UNIVERSITY OF CALIFORNIA, SAN DIEGO

Electrochemical and Thermodynamic Study of Electrode Materials on Li-ion Batteries and Aqueous Energy Storage and Conversion Applications

A dissertation submitted in partial satisfaction of the requirements for the degree Doctor of Philosophy

in

Materials Science and Engineering

by

Joon Kyo Seo

Committee in charge:

Professor Ying Shirley Meng, Chair
Professor Olivia A. Graeve
Professor Ping Liu
Professor Jian Luo
Professor Kesong Yang

2017

The Dissertation of Joon Kyo Seo is approved, and it is acceptable in quality and form for publication on microfilm and electronically:

_____

_____

_____

_____

_____
Chair

University of California, San Diego

2017

DEDICATION

To Deborah and Jooha

TABLE OF CONTENTS

LIST OF FIGURES

LIST OF TABLES

ACKNOWLEDGMENTS

First of all, I would like to thank my advisor who has mentored me for the past four years; I would like to express my sincerest gratitude to Professor Y. Shirley Meng for giving me a wonderful opportunity to be part of the greatest journey I have experienced. Her encouragement, guidance, and passion for science always inspired me to pursue my own trail without any hesitation. I also would like to thank my committee members: Prof. Olivia A. Graeve, Prof. Ping Liu, Prof. Jian Luo, and Prof. Kesong Yang for their helpful discussions and suggestions on my dissertation.

Secondly, I would like to acknowledge God almighty who gives me strength. My deepest gratitude goes to my parents Joungdae Suh and Kyungja Lee, and my parents-in-law Sangtae Kim and Heejin Kim for their love, patience, and never-ending support. Special thanks to my wife, Deborah Haesoo Kim, and my daughter, Jooha Seo for their endless support and encouragement during my Ph.D.

Lastly, I would like to express my special thanks to my collaborators and co-authors: Dr. Hyung-Man Cho and Dr. Hyojung Yoon at LG Chem, Dr. Jaewook Shin at Korea Advanced Institute of Science and Technology, Dr. Michael G. Verde at ZPower, Dr. Katsunori Takahara at Sony, Prof. Qianyu Zhang at Dongguan University of Technology, Dr. Danna Qian at Lam Research, Prof. Hui Xia at Nanjing University of Science and Technology, Prof. Zhichuan J. Xu and Dr. Yubo Chen at Nanyang Technological University, Dr. Benjamin J. Hertzberg at EOS Energy Storage, Dr. Changrong Zhu at National University of Singapore, Prof. Byungchan Han and Dr. Seunghyo Noh at Yonsei University, Dr. Min-Ho Seo at Korea Institute of Energy Research, Mr. Hitoshi Shobukawa at Asahi Kasei, Dr. Sejung Kim, Dr. Mahsa Sina, Dr. Xuefeng Wang, Ms. Hyeseung Chung, Ms. Unjong Lee, Mr. Daniel J. Noelle, Ms. Po Yu Meng, Ms. Jessie Lin, Mr.

Thomas Wynn, and Ms. An Huang at University of California San Diego, and Dr. Karena W. Chapman and Dr. Olaf J. Borkiewicz at Argonne national laboratory.

Chapter 3, in full, is a reprint of the material "Revisiting the conversion reaction voltage and the reversibility of the CuF_2 electrode in Li-ion batteries" as it appears in the Nano Research, Joon Kyo Seo, Hyung-Man Cho, Katsunori Takahara, Karena W. Chapman, Olaf J. Borkiewicz, Mahsa Sina, Y. Shirley Meng, 2017. The dissertation author was the primary investigator and author of this paper.

Chapter 4, in full, is currently being prepared for submission for publication of the material. Joon Kyo Seo, Jaewook Shin, Hyeseung Chung, Po Yu Meng, Xuefeng Wang, Y. Shirley Meng. The dissertation author was the primary investigator and author of this material.

Chapter 5, in part, is a reprint of the material "Elucidating the Phase Transformation of $Li_4Ti_5O_{12}$ Lithiation at the Nanoscale" as it appears in the ACS Nano, Michael G. Verde, Loïc Baggetto, Nina Balke, Gabriel M. Veith, Joon Kyo Seo, Ziying Wang, Ying Shirley Meng, 2016, 10, 4312. The dissertation author was the co-author of this paper. Secondly, chapter 5, in part, is a reprint of the material "Structural and electrochemical properties of Gd-doped $Li_4Ti_5O_{12}$ as anode material with improved rate capability for lithium-ion batteries" as it appears in the Journal of Power Sources, Qianyu Zhang, Michael G. Verde, Joon Kyo Seo, Xi Li, Y. Shirley Meng, 2015, 280, 355. The dissertation author was the co-author of this paper. Thirdly, chapter 5, in part, is currently being prepared for submission for publication of the material. Hyojung Yoon, Hyeseung Chung, Joon Kyo Seo, Hyung-Man Cho, Danna Qian, Mahsa Sina, Chengyu Song, Jim Ciston, Y. Shirley Meng. The dissertation author was the co-author of this material. Lastly, chapter 5, in part, is currently being prepared for submission for publication of the material. Yubo Chen, Joon Kyo

Seo, Jingxian Wang, Shibo Xi, Yonghua Du, Kaidi Yuan, Wei Chen, Adrian C. Fisher, Zhenxing Feng, Y. Shirley Meng, Zhichuan J. Xu. The dissertation author was the co-author of this material.

Joon Kyo Seo

La Jolla, September 2017

VITA

2010	Bachelor of Science in Electrical Engineering
	Kyungpook National University, Korea
2010-2011	LG Electronics, Korea
2013	Master of Science in Energy Systems Engineering
	Kyungpook National University, Korea
2017	Doctor of Philosophy in Materials Science and Engineering
	University of California San Diego, USA

PUBLICATIONS

1. **Seo, J. K.**, Shin, J., Chung, H., Meng, P. Y., Wang, X., & Meng, Y. S. Intercalation and Conversion Reactions of Nanosized β-MnO_2 Cathode in the Secondary Alkaline Battery. *In preparation.*
2. Shin, J., **Seo, J. K.**, Yayllian, R., Huang, A., & Meng, Y. S. A review of mechanistic understanding of MnO_2 in aqueous electrolyte for electrical energy storage. *In preparation*.
3. Yoon, H., Chung, H., **Seo, J. K.**, Cho, H. M., Qian, D., Sina, M., Song, C., Ciston, J., & Meng, Y. S. Mitigating surface structural instability of high voltage spinel cathode materials in Li-ion batteries. *In preparation*.
4. Kim, S., **Seo, J. K.**, Park, J. H., Song, Y., Meng, Y. S., & Heller, M. J. (2017). White-Light emission of blue-luminescent graphene quantum dots by europium (III) complex incorporation.

Accepted to Carbon.

5. **Seo, J. K.**, Cho, H. M., Takahara, K., Chapman, K. W., Borkiewicz, O. J., Sina, M., & Meng, Y. S. (2017). Revisiting the conversion reaction voltage and the reversibility of the CuF_2 electrode in Li-ion batteries. *Nano Research*, 1-13.
6. Zhu, C., Yang, L., **Seo, J. K.**, Zhang, X., Wang, S., Shin, J., Chao, D., Zhang, H., Meng, Y.S., & Fan, H. J. (2017). Self-branched α-MnO_2/δ-MnO_2 heterojunction nanowires with enhanced pseudocapacitance. *Materials Horizons*, *4*(3), 415-422.
7. Hertzberg, B.J., Huang, A., Hsieh, A., Chamoun, M., Davies, G., **Seo, J.K.**, Zhong, Z., Croft, M., Erdonmez, C., Meng, Y.S., & Steingart, D. (2016). Effect of Multiple Cation Electrolyte Mixtures on Rechargeable Zn–MnO_2 Alkaline Battery. *Chemistry of Materials*, *28*(13), 4536-4545.
8. Xia, H., Xia, Q., Lin, B., Zhu, J., **Seo, J. K.**, & Meng, Y. S. (2016). Self-standing porous $LiMn_2O_4$ nanowall arrays as promising cathodes for advanced 3D microbatteries and flexible lithium-ion batteries. *Nano Energy*, *22*, 475-482.
9. Verde, M. G., Baggetto, L., Balke, N., Veith, G. M., **Seo, J. K.**, Wang, Z., & Meng, Y. S. (2016). Elucidating the Phase Transformation of $Li_4Ti_5O_{12}$ Lithiation at the Nanoscale. *ACS nano*, *10*(4), 4312-4321.
10. Zhang, Q., Verde, M. G., **Seo, J. K.**, Li, X., & Meng, Y. S. (2015). Structural and electrochemical properties of Gd-doped $Li_4Ti_5O_{12}$ as anode material with improved rate capability for lithium-ion batteries. *Journal of Power Sources*, *280*, 355-362.
11. Seo, M. H., Choi, S. M., Lim, E. J., Kwon, I. H., **Seo, J. K**., Noh, S. H., Kim, W. B., & Han, B. (2014). Toward new fuel cell support materials: a theoretical and experimental study of nitrogen-doped graphene. *ChemSusChem*, *7*(9), 2609-2620.

12. Noh, S. H., Seo, M. H., **Seo, J. K**., Fischer, P., & Han, B. (2013). First principles computational study on the electrochemical stability of Pt–Co nanocatalysts. *Nanoscale*, *5*(18), 8625-8633.
13. **Seo, J. K.**, Khetan, A., Seo, M. H., Kim, H., & Han, B. (2013). First-principles thermodynamic study of the electrochemical stability of Pt nanoparticles in fuel cell applications. *Journal of Power Sources*, *238*, 137-143.
14. Seo, M. H., Choi, S. M., **Seo, J. K.**, Noh, S. H., Kim, W. B., & Han, B. (2013). The graphene-supported palladium and palladium–yttrium nanoparticles for the oxygen reduction and ethanol oxidation reactions: Experimental measurement and computational validation. *Applied Catalysis B: Environmental*, *129*, 163-171.

PATENTS

1. Park, K.-R., & Seo, J. K. "Photovoltaic power generation system" Korean Patent, Application Number 10-2010-0136477, Application date 12. 28. 2010.

ABSTRACT OF THE DISSERTATION

Electrochemical and Thermodynamic Study of Electrode Materials on Li-ion Batteries and Aqueous Energy Storage and Conversion Applications

by

Joon Kyo Seo

Doctor of Philosophy in Materials Science and Engineering

University of California, San Diego, 2017

Professor Ying Shirley Meng, Chair

The energy storage and conversion is one of the key issues for human beings to live sustainably on earth since our living environment has been deteriorating with the development of

industrialization. We can alleviate the waste of energy consumption and corresponding environmental pollutions by storing and converting energy efficiently. The electrochemical cells are drawing considerable attention recently as a promising solution. In this thesis, electrode materials for Li-ion batteries and aqueous electrochemical cells are studied, focusing on the electrochemical and thermodynamic aspects.

First, transition metal difluorides, MF_2 $(M = Fe, Ni, and\ Cu)$ are explored. It is found that the conversion-reaction voltage is associated with the size of the converted metal nanoparticles. The surface energy of metal nanoparticles reduces the reaction energy, which decreases the conversion-reaction voltage. In addition, CuF_2 electrodes are rechargeable when it is coated with NiO. NiO alleviates Cu dissolution into an electrolyte and enhances the cyclability of CuF_2.

Second, Zn/β-MnO_2 alkaline battery is studied as a promising rechargeable energy storage of high capacity. The nano-sized β-MnO_2 cathode in the alkaline electrolyte of LiOH and KOH exhibit the average discharge capacity of 280 mAh g^{-1} over the first 100 cycles. It is found that the β-MnO_2 transforms through proton intercalation and conversion reactions. The capacity is improved further with an addition of 4% mole fraction Bi_2O_3 in the nanosized β-MnO_2.

Third, density functional theory (DFT) calculations are conducted for $Li_4Ti_5O_{12}$ (LTO), its Gadolinium (Gd)-doped, and lithiated phases. The density of states (DOS) of LTO exhibits the property of an electrical insulator, however Gd-doped LTO is an electrical conductor which enhances the electrochemical performance. In addition, the formation energy of lithiated LTO phases is calculated to understand the reaction mechanism of LTO upon lithiation. The calculated results show that the lithiation proceeds by the two-phase reaction and there is no intermediate phase between two end phases: $Li_4Ti_5O_{12}$ and $Li_7Ti_5O_{12}$.

Lastly, oxygen evolution reaction (OER) on $YBaCo_4O_7$ (110) is investigated by DFT calculations. The results indicate that OER can be easily activated by $YBaCo_4O_7$ (110) due to its low overpotential. The free energy diagram exhibits the oxidation from O* to OOH*, which is the rate-determining step.

Chapter 1: Introduction

1.1 Li-ion batteries

Li-ion battery (LIB) is a rechargeable battery where Li-ion transports among cathode, anode, electrolyte, and a separator during charging and discharging. The component of a battery is shown in figure 1.1. Cathode and anode are a mixture of active materials, a polymeric binder, and conductive carbon deposited on an Al or Cu current collector. Active materials in cathode/anode are host materials, which electrochemically react to Li-ion during charging and discharging. The electrolyte is an ionic conductor for Li-ion to transport between cathode and anode, which consists of organic solvents. A separator is soaked in the electrolyte and located in between cathode and anode. It prevents an electrical short circuit between two electrodes.

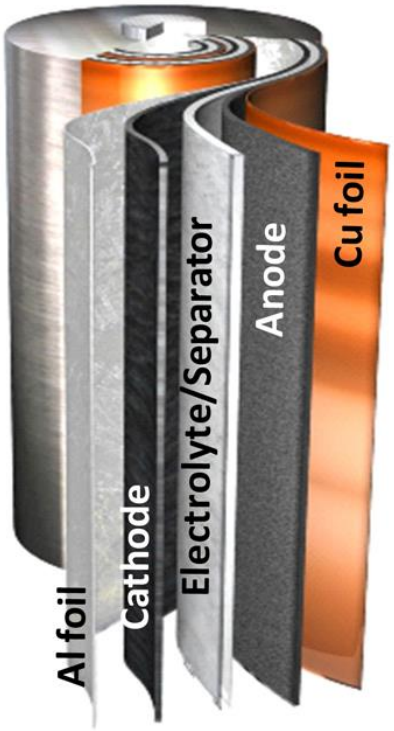

Figure 1.1 The component of a Li-ion battery[1]

The difference of Li chemical potential (μ_{Li}) in anode and cathode produces electrical energy in a Li-ion battery. Typically, anode has higher Li chemical potential than cathode as shown in figure 1.2(a). Therefore anode releases Li^+ into the electrolyte and decreases Li chemical potential while cathode receives Li^+ from the electrolyte and increases Li chemical potential. This is called discharging, which is a spontaneous reaction. The electrolyte is an ionic conductor, which provides Li^+ with a pathway between anode and cathode. The reaction in anode is oxidation and the reaction in the cathode is reduction. The electron (e^-) produced from the anode is unleashed to an electrical conductor through an external circuit, which provides energy to an electrical load.

Theoretically, Li^+ is released from the anode and recombined with the electron in cathode until Li chemical potential of both anode and cathode match, however it is prevented by a battery management system. The anode and cathode materials are structurally degraded when the difference of chemical potential significantly decreases. Therefore, the battery management system controls the depth of discharge to prohibit degradation, which enables long-cycle rechargeability.

The electrochemically stable window of electrolyte covers Li chemical potentials of both anode and cathode. The lowest unoccupied molecular orbital (LUMO) in the electrolyte needs to have higher energy level than Li chemical potential in anode so the electrolyte does not reduce; If not, the electron from anode transports to the unoccupied molecular orbital and breaks down the electrolyte. In addition, the highest occupied molecular orbital (HOMO) in the electrolyte should be lower than Li chemical potential in cathode. Then the electron that is occupied in the electrolyte lower than the HOMO does not move to cathode, which negates the electrolyte from oxidizing.

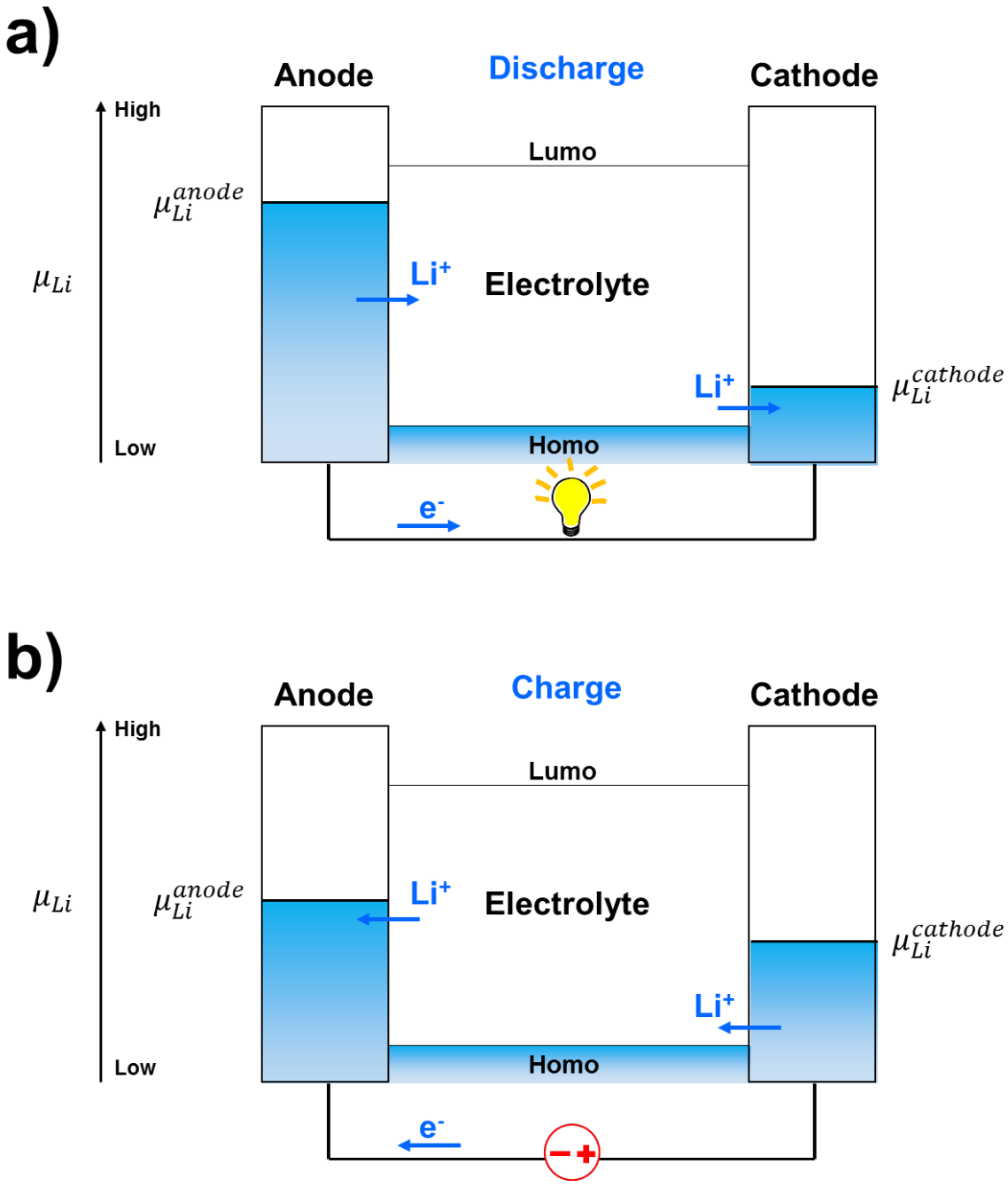

Figure 1.2 Discharge and charge reactions in a Li-ion battery

Charging is a non-spontaneous reaction as shown in figure 1.2(b). Li^+ migrates from cathode to anode with the supplied energy in a Li-ion battery. Li in cathode is forced to oxidize, which lowers the Li chemical potential. Li^+ transports to anode and reduces to Li once it merges with the

electron transferred from the external circuit. Li chemical potential in the anode increases. At the end of charge, the gap of Li chemical potential expands between anode and cathode.

1.2 Zn/MnO_2 alkaline batteries

A commercial Zn/MnO_2 alkaline battery is a primary battery consists of MnO_2 cathode, Zn anode, alkaline electrolyte, a separator, and a carbon rod current collector as shown in figure 1.3. Compared to a Li-ion battery, a commercial Zn/MnO_2 alkaline battery has a different cell design. A carbon rod is located in the center of MnO_2 cathode, which serves as a current collector. A separator is layered on MnO_2 cathode to prevent an electrical shortage with Zn anode. Alkaline electrolyte is soaked in the separator.

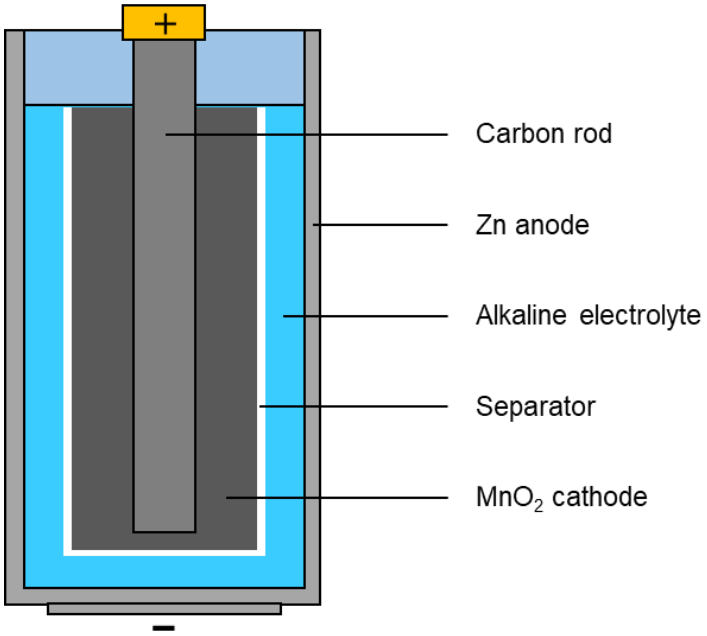

Figure 1.3 The component of a Zn/MnO_2 alkaline battery

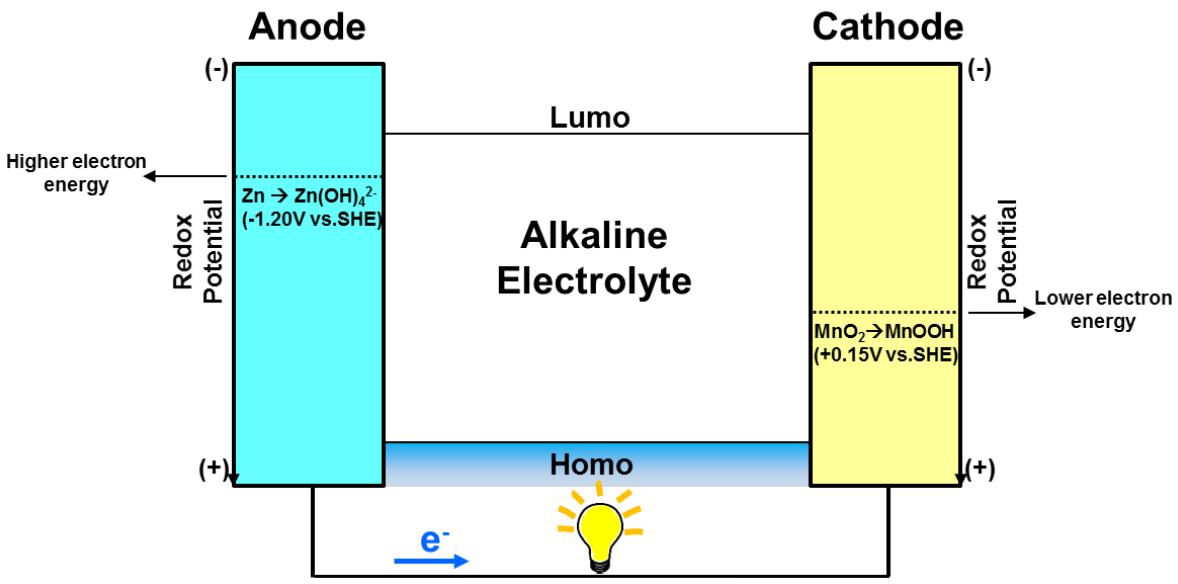

Figure 1.4 Discharge reaction of a commercial Zn/MnO_2 alkaline battery

The difference of redox potential in anode and cathode is the driving force that produces the electrical energy in a Zn/MnO_2 alkaline battery as shown in figure 1.4. Typically, Zn anode has negative value of redox potential in alkaline electrolyte and has higher electron energy whereas MnO_2 cathode has positive value of redox potential in alkaline electrolyte with lower electron energy. Therefore, Zn anode undergoes oxidation to release high-energy electrons. On the contrary, MnO_2 cathode reduces by receiving electron. This is the spontaneous redox reaction in a commercial Zn/MnO_2 alkaline battery. The electrolyte is an ionic conductor, which provides ionic phases (e.g. OH- and H-) to anode and cathode while it is oxidizing or reducing. The reaction in Zn anode is $1/2Zn + 2OH^- \rightarrow 1/2Zn(OH)_4^{2-} + e^-$ and the reaction in MnO_2 cathode is $MnO_2 + H^+ + e^- \rightarrow MnOOH$. The electron ($e^-$) is produced from anode and flows to an external circuit, providing energy to electrical load.

Theoretically, H_2 gas could be created during the operation of a Zn/MnO_2 alkaline battery since the redox potential of $H_2O + e^- \rightarrow 1/2H_2 + OH^-$ is -0.83 V vs. SHE, which resides in between

the redox potential of anode/cathode. Yet H_2 gas formation is not an issue in a conventional Zn/MnO_2 alkaline battery as it is a primary battery. H_2 gas is captured in the steel housing of a Zn/MnO_2 alkaline battery.

1.3 Electrolyzers

An electrolyzer is an energy conversion application to produce O_2 and H_2 gases by splitting H_2O. One of the widely used electrolyzers is a proton exchange membrane (PEM) electrolyzer as shown in figure 1.5. The PEM electrolyzer consists of cathode, anode, electrolyte, and a proton membrane. Once external voltage is applied, which exceeds the stable H_2O window of 1.23 V, an oxidation reaction occurs on the anode side and a reduction reaction undergoes on the cathode side. The oxidation reaction is an oxygen evolution reaction (OER), which involves $2H_2O \rightarrow O_2 + 4H^+ + 4e^-$. Once H+ is generated, it goes through the proton membrane and reacts to electron in cathode. This is a reduction reaction at cathode, which is also known as a hydrogen evolution reaction (HER) that undergoes $4H^+ + 4e^- \rightarrow 2H_2$. Theoretically, PEM electrolyzed can reverse and generate electricity, which is a PEM fuel cell. H_2 gas and O_2 gas is utilized while a PEM fuel cell is operating, which generates H_2O as a waste product.

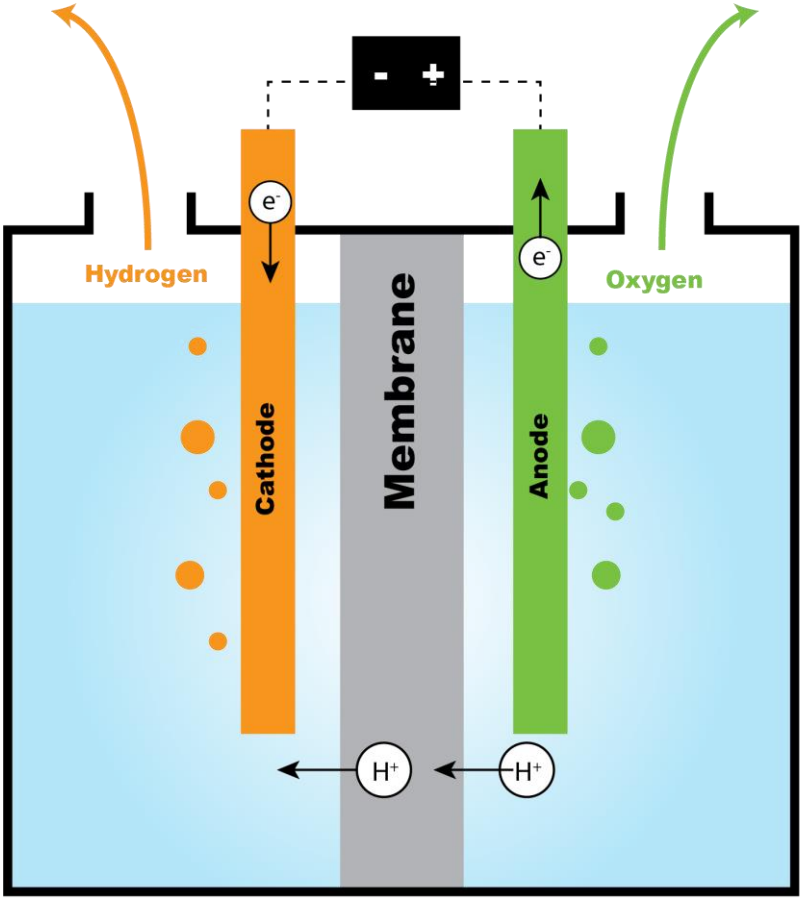

Figure 1.5 Water splitting in a proton exchange membrane (PEM) electrolyzer

Chapter 2: Background and motivation

2.1 Conversion reaction mechanism and materials in Li-ion batteries

The intercalation materials can store Li-ions reversibly because their atomic arrangement mostly maintains during Li-ion insertion and extraction. The number of available Li-ions in intercalation materials, however, is limited to 1 Li per formula unit. For example, Li_xCoO_2 layered cathode materials can be charged and discharged while Li content changes from $0 \leq x \leq 1$, theoretically. Upon Li insertion in the Li_xCoO_2 ($x = 0$), Co reduces from 4+ to 3+ electrochemically.

Due to the limited capacity in intercalation materials, alternative high-capacity materials have been extensively investigated.[2-5] The conversion material is one of the post materials of Li-ion battery since it can store multi Li-ions per formula unit. The general conversion reaction can be stated as follows;

$$MX + nLi^+ + ne^- = M + nLiX \qquad (1)$$

where M is transition metal; n is the number of electron; X is either F, O, S, N, etc. For example, CuF_2 cathode reacts to two Li-ions: $CuF_2 + 2Li^+ \rightarrow Cu + 2LiF$. While two Li-ions involved in this reaction, Cu^{2+} reduces to Cu metal and provides two electrons. On the contrary, an intercalation material provides a single electron at the most. Conversion materials undergo complete structural changes as shown in figure 2.1. This reaction is not normally reversible, because LiX on the right side of equation 1 shows poor electronic conductivity.

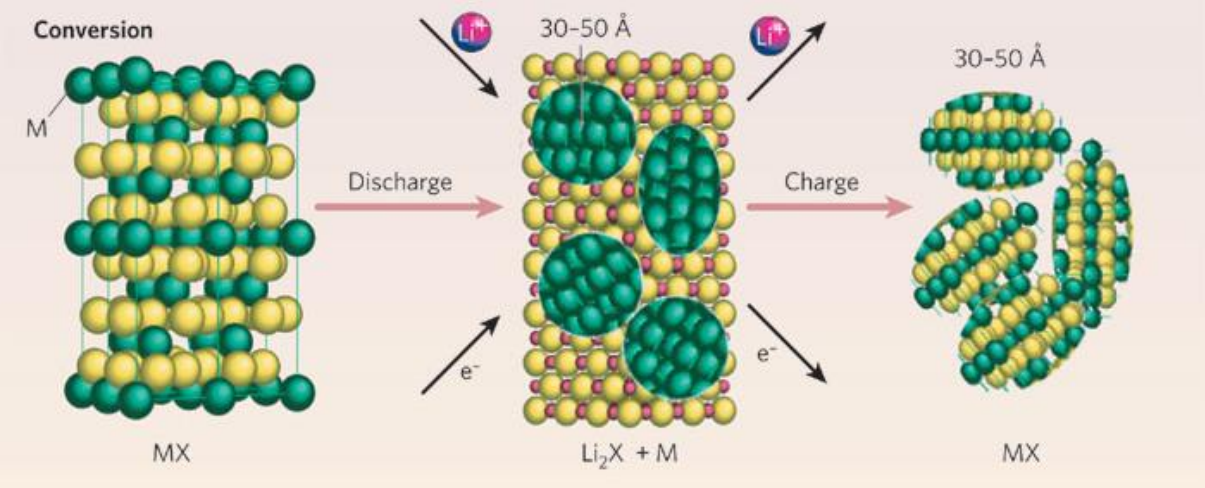

Figure 2.1 Conversion-reaction mechanism in Li-ion batteries[6]

The theoretical cell voltage (E), or electromotive force (EMF) can be obtained by applying Nernst equation for the equation 1:

$$E = \frac{n\Delta G_f(LiX) - \Delta G_f(MX)}{-nF} \qquad (2)$$

where G_f represents Gibbs free energy of formation; F is Faraday constant. Theoretical cell voltage and capacity for promising MX compounds for Li-ion conversion batteries are listed in Table 2.1.

Table 2.1 Theoretical cell voltage (or EMF) and capacity of MX compounds in Li-ion conversion batteries[3]

Table I. EMF values, Gibbs free energy of formation ($\Delta_f G$), and Li storage capacities for binary metal compounds.

MX	$\Delta_f G$ (kJ/mol)	EMF (V)	Li storage capacity (mAh/g)	MX	$\Delta_f G$ (kJ/mol)	EMF (V)	Li storage capacity (mAh/g)	MX	$\Delta_f G$ kJ/mol	EMF (V)	Li storage capacity (mAh/g)
LiF	−589	⋯	0	MnO_2	−465	1.708	1233	Ga_2O_3	−998	1.188	858
TiF_3	−1361	1.396	767	Mn_2O_3	−881	1.431	1018	GeO_2	−521	1.562	1025
VF_3	−1227	1.863	745	MnO	−363	1.032	756	Al_2O_3	−1582	0.180	1577
MnF_2	−807	1.919	577	FeO	−251	1.61	746	MgO	−569	−0.0354	1330
MnF_3	−1000	2.647	719	Fe_2O_3	−742	1.631	1007	SiO_2	−856	0.694	1784
FeF_2	−663	2.664	571	CoO	−214	1.802	715	B_2O_3	−1194	0.850	2300
FeF_3	−972	2.742	712	NiO	−212	1.954	718	Ce_2O_3	−1708	−0.038	490
CoF_2	−627	2.854	553	CuO	−128	2.248	674	Li_2S	−439	⋯	0
CoF_3	−719	3.617	694	Cu_2O	−148	2.147	375	TiS_2	−402	1.233	957
NiF_2	−604	2.964	554	ZnO	−320	1.252	659	CoS_2	−146	1.898	871
CuF_2	−492	3.553	528	SnO	−257	1.566	398	Co_3S_4	−487	1.644	703
ZnF_2	−714	2.404	518	SnO_2	−520	1.582	711	CuS	−53	1.998	561
SnF_2	−601	2.984	342	Ag_2O	−11.2	2.855	231	Cu_2S	−86	1.827	337
AgF	−187	4.156	211	RuO_2	−280	2.12	805.6	FeS	−102	1.747	610
PbF_2	−617	2.903	218	MoO_2	−533	1.669	838.2	FeS_2	−160	1.861	893
CaF_2	−1173	0.0259	686	MoO_3	−668	1.75	1117	MnS	−218	1.144	616
BaF_2	−1158	0.104	306	SrO	−561	0.005	517	MnS_2	−225	1.692	900
Li_2O	−562	⋯	0	SrO_2	−573	1.428	896	MoS_2	−226	1.69	670
TiO	−513	0.253	839	Y_2O_3	−1817	−0.226	712	Ag_2S	−40.7	2.06	216.3
TiO_2-R	−890	0.608	1342	ZrO_2	−1040	0.217	870	Li_3N	−129	⋯	0
TiO_2-A	−883	0.625	1342	NbO	−392	0.881	492	TiN	−309	−0.623	1301
VO	−404	0.819	801	NbO_2	−795	0.852	858	Co_3N	−34	0.326	421
V_2O_3	−1139	0.945	1073	Nb_2O_5	−1766	1.082	1008	Fe_4N	−3.722	0.432	338.7
VO_2	−1318	−0.502	1293	In_2O_3	−831	1.477	579	Mn_4N	−105	0.083	459
V_2O_5	−1419	1.441	1474	Sb_2O_3	−634	1.817	552	Mn_5N_2	−155	0.176	531
Cr_2O_3	−1058	1.085	1058	PbO	−189	1.933	721				
Cr_3O_4	−1531	~0.93	975	CeO_2	−1025	0.257	623				

The highest theoretical cell voltage is in AgF (~ 4.16 V) and the largest capacity is in B_2O_3 (2300 mAh/g). In general, the capacity of conversion materials shows higher values than intercalation materials because multi Li-ions per formula unit can be stored, however, the cell voltage is lower than intercalation materials. For example, the commercial $LiNi_{0.5}Mn_{1.5}O_4$ spinel cathode shows ~4.7 V vs. Li metal.[7] Among conversion materials, transition-metal fluorides have relatively high theoretical cell voltage owing to the strong ionic bonding between the transition metal and fluorine.[5] FeF_2, NiF_2, and CuF_2 have theoretical cell voltage over 2.5 V. In order to get over the poor electronic conductivity, numerous methods have been applied to network carbon and conversion materials. For example, nanocomposites of carbon and transition-metal fluorides were developed, which leads to high conversion voltage with cycling performance.[8-10]

2.2 Rechargeability of Zn/MnO_2 alkaline batteries

Electrochemical cells for energy storage systems need to meet several requirements such as low cost, long cycle, high energy density, safety, and reliability. Zn/MnO_2 alkaline battery has drawn attention since it meets most of the requirement. For example, Mn and Zn are earth-abundant materials so their costs are extremely cheaper that Li and Co, which are popular elements of commercial Li-ion batteries. Mn and Zn cost $ 2 and $ 1.5 per pound while Li and Co are $ 30 and $ 25 per pound as of 2015 (figure 2.2).

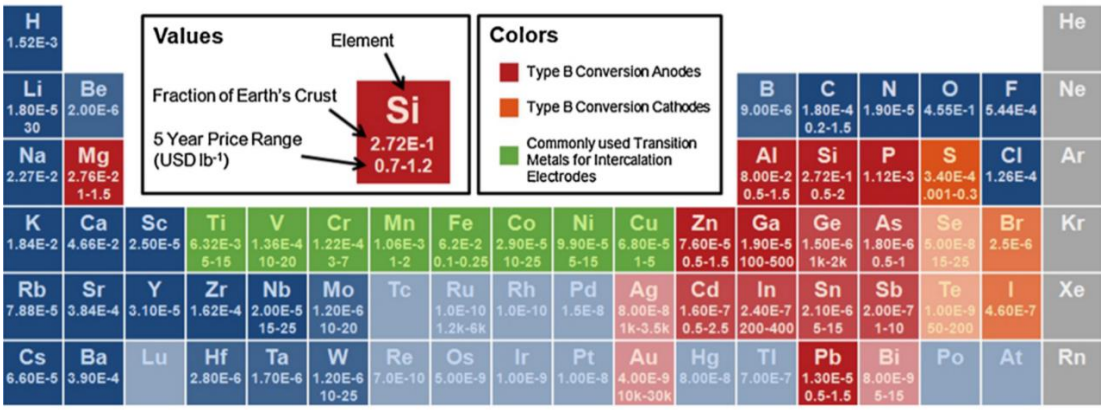

Figure 2.2 Availability and prices of earth elements[11]

MnO_2 has the theoretical gravimetric capacity of 616 mAh g^{-1} which is over twofold higher than $LiCoO_2$ of 272 mAh g^{-1}. The commercial primary Zn/MnO_2 alkaline batteries have vast energy density (> 400Whl^{-1}) as well.[12] Considering safety, this electrochemical cell operates in an aqueous system, which has low possibility of fire from the short electrical circuit.

Rechargeability is the one of issues of the current Zn/MnO_2 alkaline batteries for their commercialization. Figure 2.3 shows the capacity fading in the voltage range of 1.10 V – 1.65 V.[13] The concentrated KOH affects the cycle performance, however, all the batteries undergo severe

capacity fading at early cycles (≤ 25 cycles).

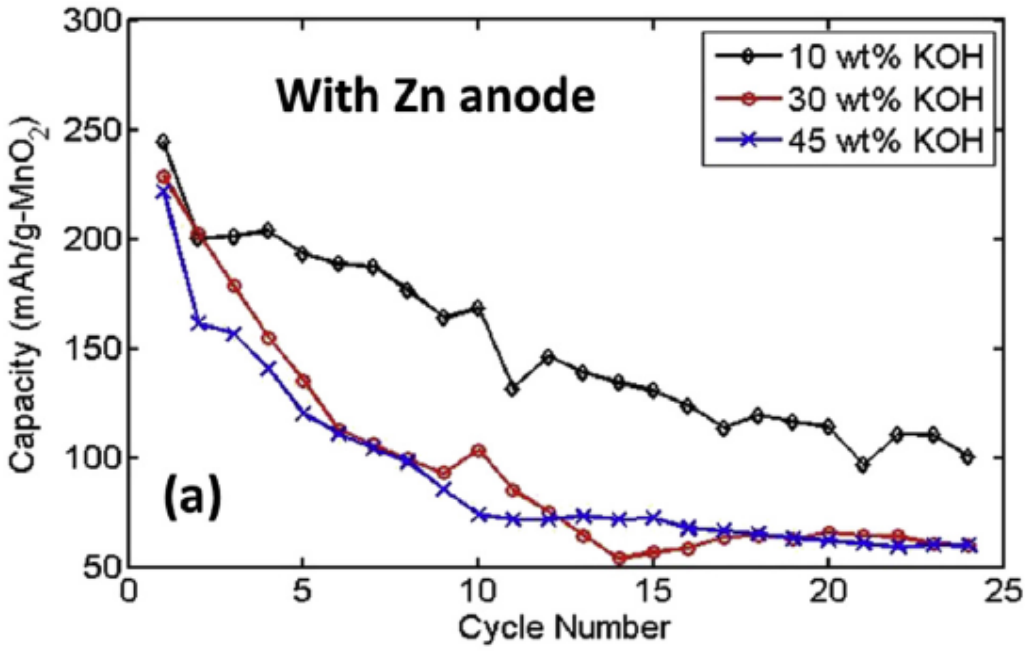

Figure 2.3 Cycling performances of Zn/MnO_2 alkaline batteries depending on the concentration of KOH[13]

It is reported that controlling the depth of discharge to only 5-10% of the theoretical capacity promotes rechargeability to 1000-3000 cycles, yet it significantly reduces the energy density to $22Whl^{-1}$.[13] Therefore it is important to attain high theoretical capacity of MnO_2 with long-cycle reversibility. MnO_2 reduces to MnOOH and $Mn(OH)_2$ during discharging and both reduced phases oxidize back to MnO_2 during charging. However, $ZnMn_2O_4$ is generated which is an undesirable phase. It is explained that $ZnMn_2O_4$ has resistivity six orders of magnitude higher than that of MnO_2, which is about 10^8 ohm·cm.[14] Such a high resistivity causes capacity loss and non-rechargeability. The $ZnMn_2O_4$ phase is a product of chemical reaction between MnOOH in cathode and $Zn(OH)_4^{2-}$ in anode. $Zn(OH)_4^{2-}$ is generated after Zn is oxidized, which migrates to cathode side and reacts to MnOOH to produce $ZnMn_2O_4$.

2.3 Spinel-type transition metal oxides for Li-ion intercalation reaction

2.3.1 $Li_4Ti_5O_{12}$ spinel

$Li_4Ti_5O_{12}$ anode for LIB applications is tracked back to the discovery of Li-intercalation activity on Li titanate materials.[15-17] Early studies probed that $Li_4Ti_5O_{12}$ showed semiconducting property upon Li intercalation at the voltage of 1.55 V vs. Li/Li^+.[18] Relatively higher reaction voltage of $Li_4Ti_5O_{12}$ compared to graphite reduces overall cell voltage, however it prevents an electrical short circuit among electrodes in a cell. The graphite anode has an intrinsic property that Li could be electroplated on its surface, which might cause a safety issue. The theoretical capacity of $Li_4Ti_5O_{12}$ is 175 mAh g^{-1} when a single Li is inserted:[19]

$$[Li]_{8a}[Li_{1/3},Ti_{5/3}]_{16d}[O_4]_{32e} + e^- + Li^+ = [Li_2]_{16c}[Li_{1/3},Ti_{5/3}]_{16d}[O_4]_{32e} \quad (3)$$

$Li_4Ti_5O_{12}$ shows the Fd3m space group, which is composed of Li in 8a and 16d, and Ti in 16d Wyckoff positions as shown in figure 2.4.

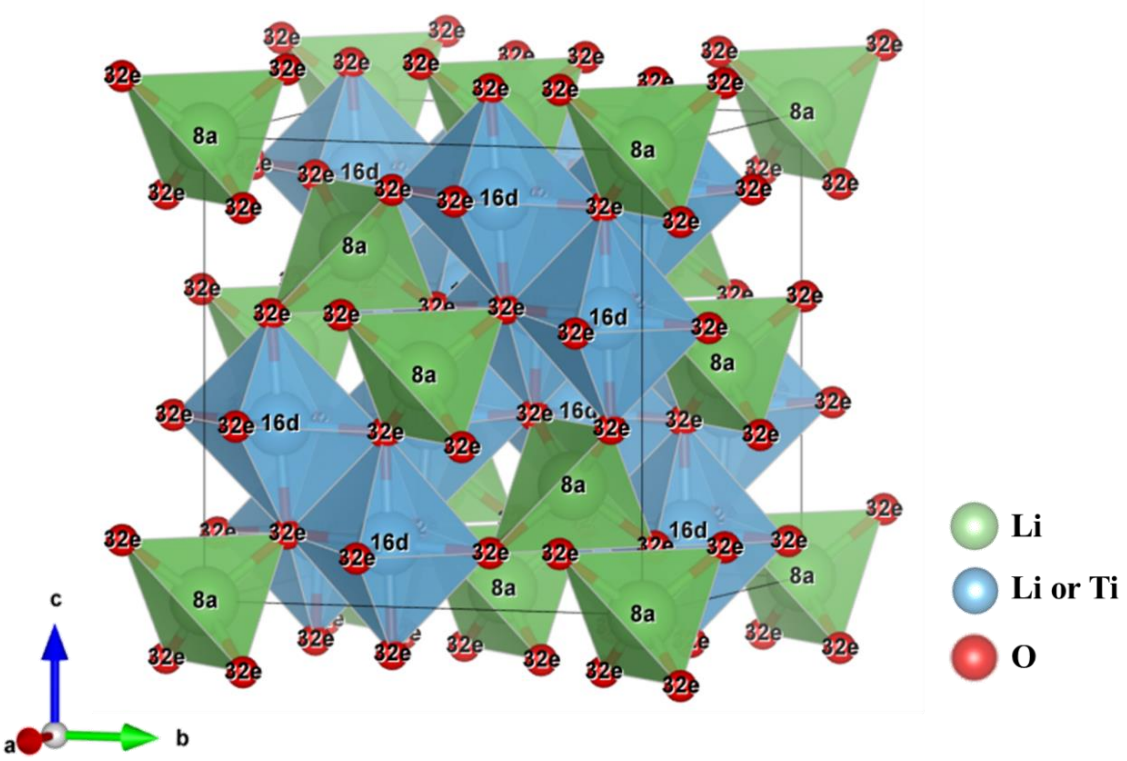

Figure 2.4 $Li_4Ti_5O_{12}$ lattice composed of Li in 8a and 16d, and Ti in 16d Wyckoff positions

Oxygen in the 32e positions coordinates with Li and Ti in tetrahedral and octahedral manners. Almost zero-strain is found while Li intercalates the $Li_4Ti_5O_{12}$. The network of octahedrons in $Li_4Ti_5O_{12}$ provides a three-dimensional Li diffusion path, which limits the volume change during Li intercalation. Therefore, this material allows a high rate and a long cycle life.

2.3.2 $LiNi_{0.5}Mn_{1.5}O_4$ spinel

$LiNi_{0.5}Mn_{1.5}O_4$ spinel provides a long voltage plateau at around 4.7 V and high energy density of 650 Wh/kg.[20] This capability has drawn attention to consider $LiNi_{0.5}Mn_{1.5}O_4$ spinel as a promising cathode material for electric vehicles. Li diffusion in the three-dimensional network of metal-oxygen octahedron (figure 2.5) enables high rate capability and long cycling stability.

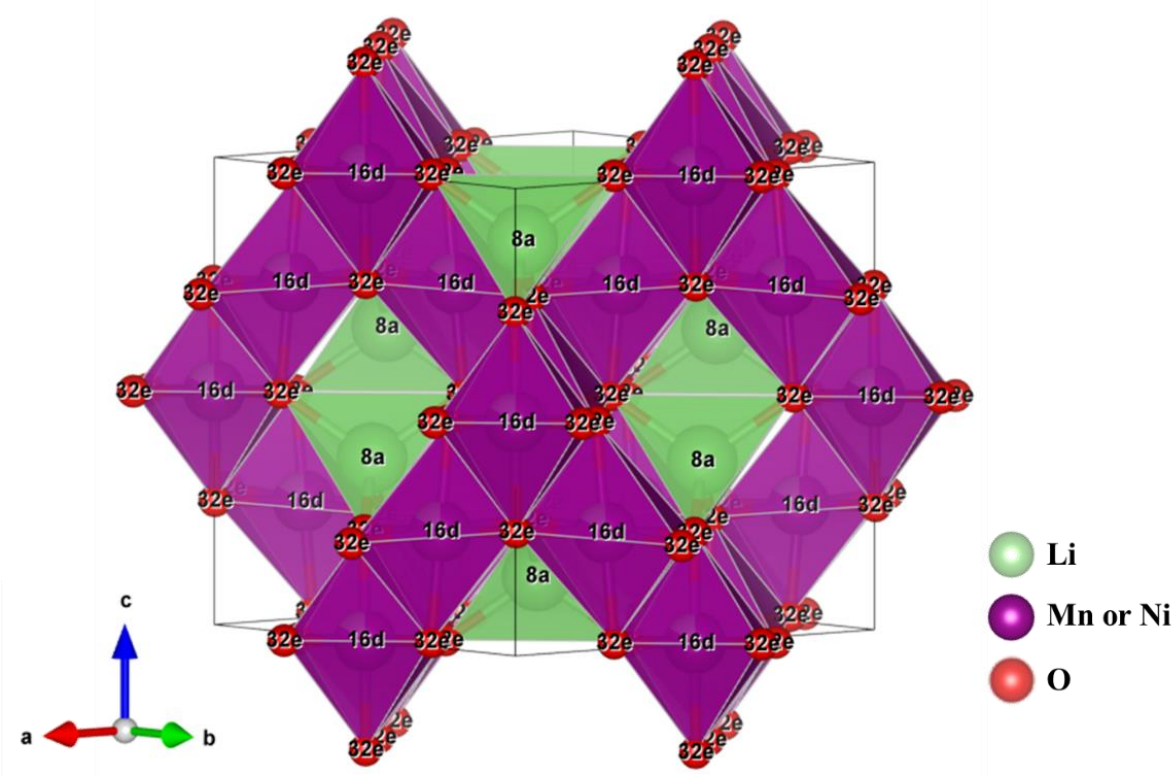

Figure 2.5 $LiNi_{0.5}Mn_{1.5}O_4$ lattice composed of Li in 8a and Mn or Ni in 16d Wyckoff positions

$LiNi_{0.5}Mn_{1.5}O_4$ shows the Fd3m space group, which consists of Li in 8a; Mn or Ni in 16d Wyckoff positions, as shown in figure 2.5. Oxygen, 32e Wyckoff position, is tetrahedrally coordinated with Li and octahedrally coordinated with Mn and Ni. The electrochemical performance of $LiNi_{0.5}Mn_{1.5}O_4$ is highly dependent on the presence of Mn^{3+}. It is reported that Mn^{3+} is redox active and creates a small plateau region at around 4V.[21] Some of Mn^{3+}, however, undergoes disproportionation, which generates Mn^{2+}. Then Mn^{2+} dissolves toward electrolyte, which is propelled at an elevated temperature. This side reaction significantly affects the capacity loss. In order to enhance the cycle performance, several doping approaches have been conducted. Li, Mg, Fe, Co, and Zn dopants changes minimally in the lattice parameter, which enhances the cycling performance.[22] The surface modification and electrolyte additive effects are also proven to increase the cycling performance of $LiNi_{0.5}Mn_{1.5}O_4$.[23]

2.4 Oxygen evolution reaction in electrolyzers

The water electrolysis is a key mechanism to produce hydrogen and oxygen gas. The scalable technology to generate hydrogen and oxygen gas is required for sustainable development on batteries. The hydrogen gas has drawn attention to generate power in fuel cell applications.[24] Most hydrogen gas is created by the process that reforms steam for natural fuels, which produces CO_2, the greenhouse gas, however the water electrolysis produces hydrogen gas without generating CO_2 when the energy sources for electrolysis is drawn from the renewables energy such as solar, wind, and tidal power. Therefore, the water electrolysis needs to enhance its efficiency and reduce its costs to operate. Limited efficiency of current technology is partially derived from the overpotential to promote the slow kinetics of the oxygen evolution reaction (OER) at anode in aqueous solutions.

Understanding fundamental reactions on an atomic scale is important to improve the performance of catalyst materials. The activity of catalyst is highly dependent on the binding energy of intermediates. The DFT calculation is an advanced characterization tool that can calculate the intermediates' binding energy.[25] In general, OER reaction mechanism undergoes four single-electron reactions. For example, OH, O, and OOH adsorbed catalysts are used as OER model systems and the free energy diagram is plotted depending on the applied voltage.[26] Figure 2.6 shows the free energy diagram of OER on the catalyst surface functioning as applied potential. The overall OER is spontaneous when the potential is 1.80 V.

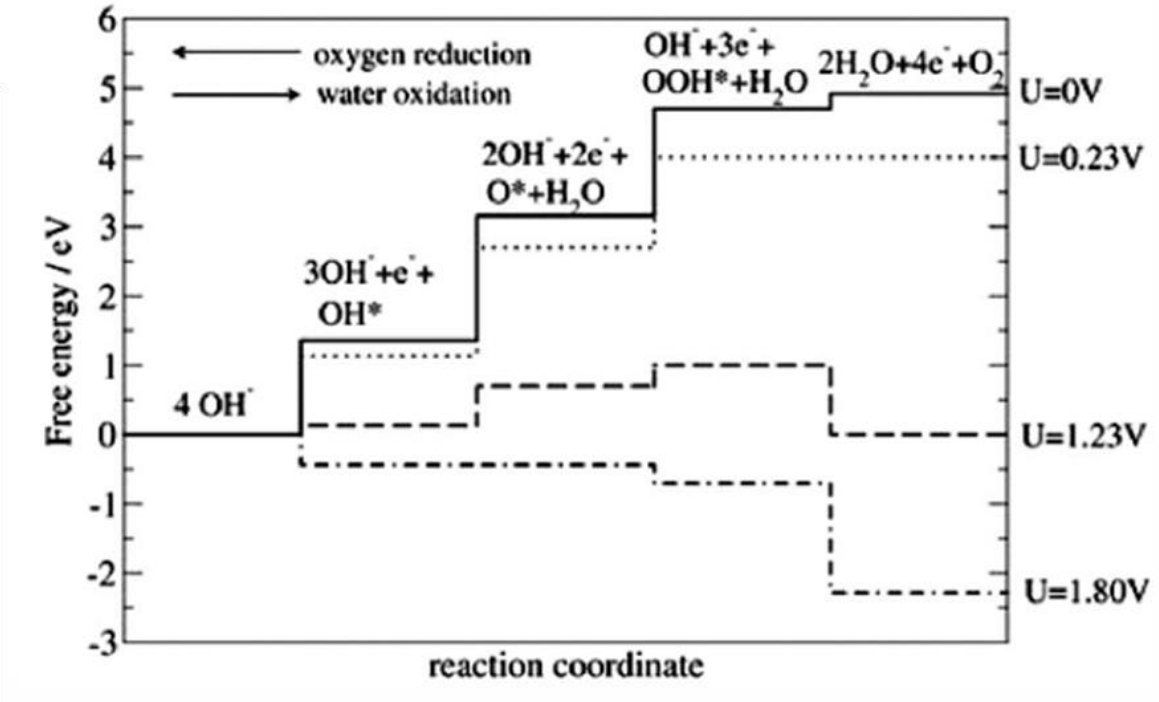

Figure 2.6 Free energy diagram of OER (from left to right) on the $CuCo_2O_4$ (111)[27]

Chapter 3: Revisiting the conversion reaction voltage and the reversibility of the CuF_2 electrode in Li-ion batteries

3.1 Introduction

Lithium-ion batteries have been used for energy sources in various mobile and stationary applications. In order to meet the growing demands for mass market adoption, improving the energy density and reducing the cost of rechargeable batteries are inevitable [28]. Conversion materials have a high Li storage capacity compared to commercialized electrode compounds of intercalation reaction [2]. Among conversion materials, transition metal difluorides, MF_2 ($M = Fe, Ni, and\ Cu$), especially show a relatively higher reaction voltage due to the strong M-F ionic bond [5]. In order to achieve the potential implication of these compounds in rechargeable batteries, there has been wide progress in practical improvement. Badway et al. developed a carbon-metal fluoride nanocomposite, which is composed of nano-domains of FeF_3 with high surface to volume ratio in carbon matrix. It is demonstrated that the high surface to volume ratio of nano-size FeF_3 are electroactively improved [9-10]. Later, they introduced another concept of nanocomposite design that enables CuF_2 to have 98% of theoretical discharge capacity within the voltage range of 2.0 - 4.0 V vs. Li/Li^+. The nanocomposite composed of carbon matrix with intercalation compounds (e.g. MoO_3, V_2O_5, MnS_2, etc) promotes electron and ion conductivity [29]. Oxygen doping into the metal fluorides, such as FeOF and Fe_2OF_4, also has been shown to enhance electrochemical properties [30-33]. It is proposed that substituting O for F increases average conversion voltage and facilitates cycling stability by incorporating more covalent M-O bonds into the ionic fluoride structure. Recently, Wang et al. reported reversible ternary metal fluorides, $Cu_yFe_{1-y}F_2$ [34]. They proposed the incorporation of Cu into the FeF_2 crystal lattice, which promotes the reversible redox behavior of $Cu^{2+} \leftrightarrow Cu^0$. Although the reversible capacity of Cu content degrades due to the Cu

dissolution, the ternary fluoride exhibits the low hysteresis with high voltage and capacity.

Despite of progress in conversion materials as promising future batteries, there are still unsolved issues: (i) The discrepancy between experimental voltage of transition metal difluorides, MF_2 ($M = Fe, Ni\ and\ Cu$) and the theoretical thermodynamic voltage, and (ii) non-reversible conversion reaction of CuF_2. As for the voltage discrepancy, it is reported that experimental voltage plateau for MF_2 ($M = Fe, Ni\ and\ Cu$) is lower than thermodynamic reaction voltage [3, 35]. In order to understand the origin of the voltage deviation problem, we use density functional theory (DFT) and calculate the conversion reaction voltage depending on the size of M ($M = Fe, Ni\ and\ Cu$) nanoparticle formed during discharging. We also conduct PITT experiment on NiF_2 and CuF_2 electrodes to observe near-equilibrium conversion reaction voltage. The average size of Ni and Cu nanoparticles during lithiation is measured by STEM to correlate the nano-size effect of metal particle formation with the reaction voltage.

CuF_2 electrode has the highest theoretical voltage among MF_2 ($M = Fe, Ni,\ and\ Cu$) that is suitable for power driven mobile devices, however, CuF_2 is intrinsically non-reversible in contrast to FeF_2 and NiF_2 [4, 36]. Wang et al. reported the origin of irreversibility is due to the separation between large Cu nanoparticles (5-12 nm in diameter) and LiF, which blocks electron paths [36]. Yamakawa et al. suggested that the different diffusivity of the ionic phases (F^- and Li^+) brings about the formation of LiF coating on the CuF_2/Cu and CuF_2/electrolyte interfaces and hinders the reversible reaction [37]. Recently, Hua et al. presented that the degradation mechanism of CuF_2 is associated with Cu dissolution along with LiF consumption [38]. In this study, we apply NiO coating on CuF_2 to study the effect of NiO on the reversible CuF_2 conversion reaction. As NiO is not electrochemically active within our voltage range (2.0 - 4.0 V), it does not contribute

any additional capacity to CuF_2. This is opposed to the other metal oxides including MoO_3, V_2O_5, and MnS_2 which have been adopted to CuF_2 conversion reaction [29]. ADF-STEM and EELS techniques are used to comprehend a reversible conversion mechanism of NiO coated CuF_2 electrode.

3.2 Experimental

We conduct first principles calculations [39] based on the spin-polarized GGA and GGA + *U* [40-41] using the Perdew-Burke-Ernzerhof exchange correlation implemented in DFT [42]. We use a plane-wave basis set and the projector-augmented wave (PAW) method [43-44] as parameterized in the Vienna ab initio simulation package (VASP) [45]. A gamma point mesh is performed with 9 x 7 x 7 k-points for CuF_2, 7 x 7 x 11 k-points for NiF_2, and 7 x 7 x 9 k-points for FeF_2. For metal nanoparticles, gamma point is used to sample the Brillouin zone, and periodic boundary conditions are imposed on the unit cell where a vacuum size is larger than a nanoparticle's diameter to prohibit interactions among the images. All the atoms are fully relaxed to calculate the optimized structure with a cutoff energy of 1.3 times the maximum cutoff specified by the pseudopotentials of the elements on a plane wave basis set. Our GGA + *U* calculations indicate that the lattice parameters of metal fluorides are agreed well with experimental measurements and the error is less than 2 % (Table 3.1).

Table 3.1 Comparison of lattice parameters between GGA + *U* calculation and experiments

	Compound	a (Å)	b (Å)	c (Å)	β (deg)
GGA + *U* calculation	CuF_2	3.332 (1.06 %)	4.617 (1.20 %)	4.671 (1.19 %)	82.756 (0.65 %)
	NiF_2	4.696 (1.00 %)	4.696 (1.00 %)	3.104 (0.67 %)	90.000
	FeF_2	4.788 (1.99 %)	4.788 (1.99 %)	3.316 (0.18 %)	90.000
Experimental	CuF_2	3.297	4.562	4.616	83.293
	NiF_2	4.650	4.650	3.084	90.000
	FeF_2	4.695	4.695	3.310	90.000

It is noted that we adopt mixing GGA and GGA + *U* framework proposed by Jain et al [46] in order to obtain accurate reaction energy and the voltage of conversion reaction. The detailed explanation on the framework is discussed in results and discussion section.

Table 3.2 The average radius of M (M=Fe, Ni, and Cu) nanoparticle composed of n atoms

n	**Iron**		**Nickel**		**Copper**	
	Cuboctahedron	**Icosahedron**	**Cuboctahedron**	**Icosahedron**	**Cuboctahedron**	**Icosahedron**
13	2.44 Å	2.40 Å	2.37 Å	2.32 Å	2.47 Å	2.41 Å
55	4.85 Å	4.75 Å	4.80 Å	4.60 Å	4.94 Å	4.81 Å
147	7.25 Å	7.04 Å	7.26 Å	7.01 Å	7.49 Å	7.29 Å
309	9.94 Å	9.30 Å	9.71 Å	9.39 Å	10.03 Å	9.74 Å

Commercial CuF_2 (Aldrich) and NiF_2 (Alfa Aesar) powders are used for this study. In order to synthesize carbon-coated metal difluoride, CuF_2/C (or NiF_2/C), we prepare a milling jar where 80 wt. % of conversion material and 20 wt. % of acetylene black (Strem Chemicals) are mixed together in the MBraun Ar-filled glovebox (H_2O < 0.1 ppm). The jar is sealed with Parafilm before being transferred to the planetary ball mill (PM 100, Retsch) and the milling is performed for 6 hours at 500 rpm. In addition, NiO (Aldrich) coated CuF_2 (NiO-CuF_2) with the stoichiometric of CuF_2 : NiO = 85 : 15 wt. % is prepared by the ball milling for 4 hours at 650 rpm under an Ar

atmosphere. NiO-CuF_2 is milled again with acetylene black to synthesize carbon-coated samples (NiO-CuF_2/C). The mass loading of CuF_2 and NiF_2 in PITT discharge experiment is 1.36 and 1.49 mg cm^{-2} respectively. Considering the cycling test of CuF_2 and NiO-CuF_2, 0.84 and 1.17 mg cm^{-2} of CuF_2 are used.

The electrochemical cells are disassembled in an argon-filled glovebox, and the electrodes are washed with dimethylene carbonate (DMC). Then the electrodes are scraped to produce fine powder. Small amount of powder is placed on a transmission electron microscopy (TEM) lacy carbon film supported on a copper grid. SAED patterns, ADF-STEM images, and EELS are acquired using a JEOL 2010F operated at 197 kV and equipped with a Gatan GIF 200 spectrometer. The EELS spectra are obtained with a collection half angle of 27 mrad and convergence angle of 10 mrad and with an energy resolution of 0.9 eV. Additionally, the ADF-STEM image as EELS spectrum image is attained using a TEAM 0.5 aberration corrected instrument operating at 80 KV at Lawrence Berkeley National Laboratory, equipped with a high brightness Schottky-field emission electron source. The ADF-STEM image and EELS elemental maps are acquired using a Gatan Efinia spectrometer; with a collection angle of 52 mrad and convergence angle of 30 mrad. Cu dissolution into the electrolyte is characterized by inductively coupled plasma optical emission spectroscopy (ICP-OES) (PerkinElmer Plasma 3700). 25 μL of electrolyte is gathered from a custom-made electrochemical cell and included into the 25 mL solution matrix (1:1 wt %, HNO_3/HCl). Therefore, the electrolyte is examined at a 1000 times diluted solution [47].

In our study, electrochemical characterization is performed using coin-type (2016) cells. We use a battery cycler (Arbin) at room temperature. We make working electrodes composed of active materials (NiO-CuF_2/C, CuF_2/C or NiF_2/C), acetylene black and polyvinylidene fluoride (PVDF) with 70:20:10 wt. % ratio. Pure lithium metal is used as a counter electrode and polypropylene

C480 (Celgard) is used as a separator. The coin cells are assembled with the electrolyte consisting of 1 M $LiPF_6$ dissolved in EC and DMC with a weight ratio of 1:1 (BASF) in the MBraun Ar-filled glovebox (H_2O < 0.1 ppm). The theoretical specific capacity of CuF_2 and NiF_2 are 528 and 554 mA h g^{-1}, respectively, which are used to set C rate. PITT is adopted on the first discharge of CuF_2/C and NiF_2/C cells with the voltage limits of 2.0 V and 1.0 V, respectively. The voltage step size is 10 mV with a cut-off current density of C/1000 of active material. In addition, electrochemical cycling of NiO-CuF_2/C and CuF_2/C are tested with the constant current density of C/35. The cell voltage ranges of 2.0 - 4.0 V is applied. The first discharge of CuF_2/C and NiF_2/C are performed with the constant current density of C/35, and the discharge voltage limit of 2.0 and 1.0 V, respectively. For the linear potential sweep voltammogram, Cu foil is employed for the working electrode. Other conditions including a coin-type cell, a separator, electrolyte, and a reference electrode are same as battery experiments. Scan rate was 1 mV s^{-1}.

3.3 Results and Discussion

3.3.1 Computational model systems

We set up four different sizes of metal nanoparticle models, $M_n^{cubo\ or\ icosa}$ (n is the number of atoms in nanoparticle), as shown in figure 3.1(a, b):

(i) $M_{13}^{cubo\ or\ icosa}$ (13 atoms and ~0.5 nm in diameter),

(ii) $M_{55}^{cubo\ or\ icosa}$ (55 atoms and 0.9 - 1.0 nm in diameter),

(iii) $M_{147}^{cubo\ or\ icosa}$ (147 atoms and 1.4 - 1.5 nm in diameter), and

(iv) $M_{309}^{cubo\ or\ icosa}$ (309 atoms and 1.9 - 2.0 nm in diameter),

in order to calculate the conversion voltage of MF_2 ($M = Fe, Ni\ and\ Cu$), with respect to metal nanoparticle sizes.

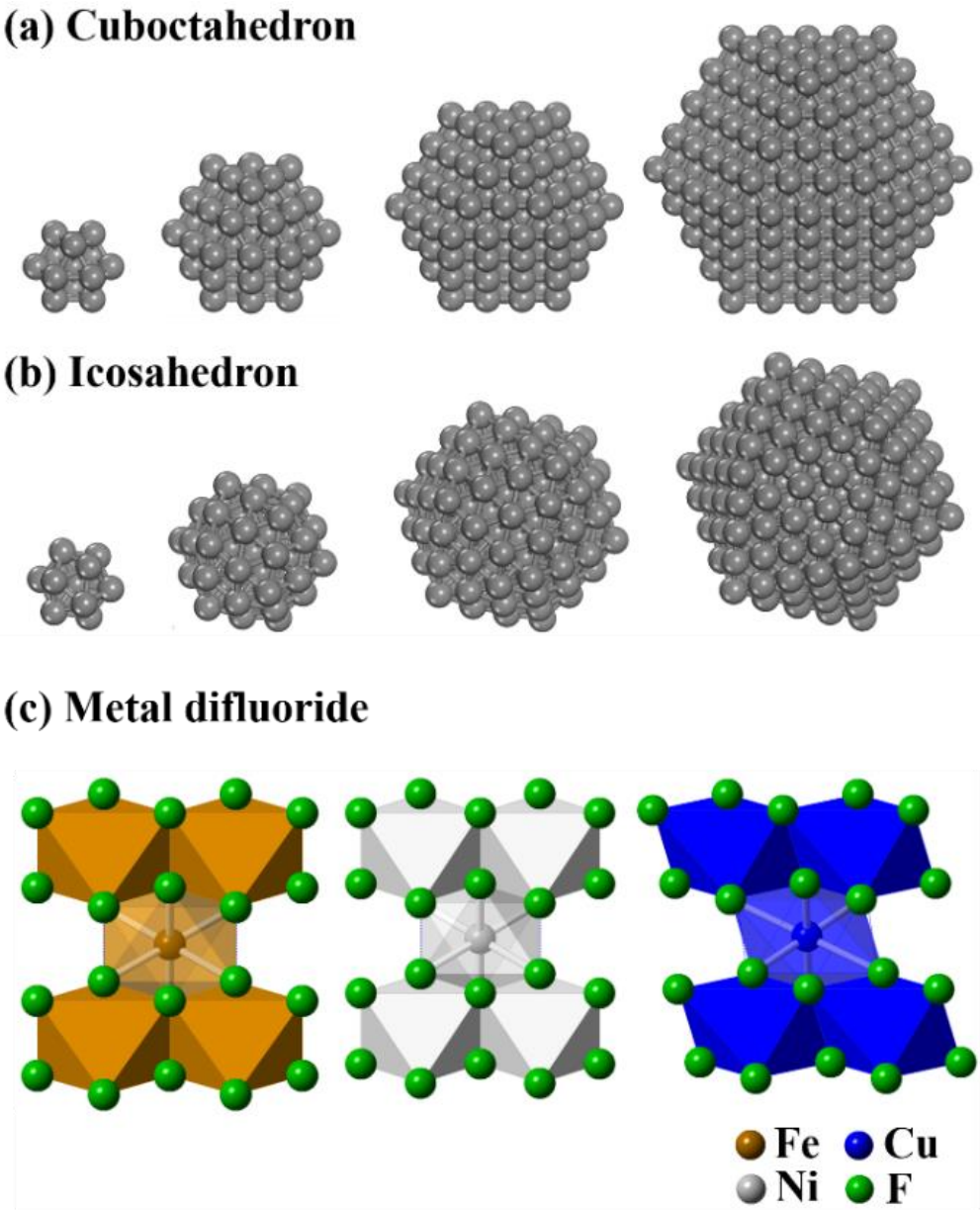

Figure 3.1 Model systems of (a) cuboctahedron and (b) icosahedron for Fe, Ni and Cu, composed of 13 atoms, 55 atoms, 147 atoms and 309 atoms (Fe cuboctahedron: 0.5, 1.0, 1.4 and 2.0 nm in diameter; Fe icosahedron: 0.5, 1.0, 1.4 and 1.9 nm in diameter; Ni cuboctahedron: 0.5, 1.0, 1.5 and 1.9 nm in diameter; Ni icosahedron: 0.5, 0.9, 1.4 and 1.9 nm in diameter; Cu cuboctahedron: 0.5, 1.0, 1.5 and 2.0 nm in diameter; Cu icosahedron: 0.5, 1.0, 1.5 and 1.9 nm in diameter). (c) The crystal structures of FeF_2, NiF_2 and CuF_2. FeF_2 and NiF_2 are tetragonal, and CuF_2 is the monoclinic

The average distance between two diametrically opposite vertices is defined to be the size of a nanoparticle and its radius is listed in Table 3.2. The shapes of the nanoparticle are ideal cuboctahedron and icosahedron structures, solely consisting of (111) and (100) planes [48], and (111) plane [49], respectively; These planes correspond to the low Miller index planes with low surface energies [50] resulting in an optimal configuration of cuboctahedron and icosahedron with minimal total free energy for a given particle size [51-54]. These morphologies are quite similar to the "magic number" nanoparticle, which also have been found to be thermodynamically stable [48, 55]. Because the activation energy to transform another morphology among ultra-small nanoparticles is very small [56-57], our model structures can be converted to different structures. This effect is outside of the extent of the present study.

Table 3.3 Bulk-phase reaction voltages calculated from GGA, mixing GGA/GGA + *U*, and Gibbs free energy of formation in thermodynamic table

Method	**FeF_2**	**NiF_2**	**CuF_2**
GGA	3.06 V	3.46 V	3.70 V
Mixing GGA/GGA + *U* (This work)	2.58 V	2.91 V	3.56 V
Gibbs free enregy of formation (Thermodynamic table)	2.66 V	2.96 V	3.55 V

The crystal structures of metal difluorides investigated in our study are FeF_2, NiF_2 and CuF_2, shown in figure 3.1(c). These crystals have rutile-type structure where transition metals are surrounded by an octahedron of 6 fluorine atoms. CuF_2 crystallizes in the monoclinic structure (P 1 21/n 1 space group) that produces a highly distorted octahedral. NiF_2 and FeF_2, however, have tetragonal structure with P 42/m n m space group.

3.3.2 Influence of metal-nanoparticle size on the conversion reaction voltage

The electrochemical conversion of transition metal difluoride, MF_2 ($M = Fe, Ni\ and\ Cu$) with Li is two-electron reaction where divalent metal ion is reduced to metallic phase.

$$MF_2 + 2Li \xrightarrow{2e^-} 2LiF + M \quad (1)$$

Thermodynamic voltage ($E^{bulk}_{thermodynamic}$) for the reaction (Eq. (1)) can be obtained from [3]

$$E^{bulk}_{thermodynamic} = \frac{G_f(2LiF) - G_f(MF_2)}{-2F} \quad (2)$$

where G_f and F are standard Gibbs free energy of formation from thermodynamic table and Faraday constant, respectively. It is noted that G_f is relevant to bulk-phase formation energy so that $E^{bulk}_{thermodynamic}$ acquired from G_f corresponds to the conversion voltage for bulk-phase reaction. Most experimental reports on MF_2 ($M = Fe, Ni\ and\ Cu$) conversion reactions however, show that the experimental voltage is much lower than $E^{bulk}_{thermodynamic}$ (up to ~1.5 V) [4, 29, 35-37, 58-59]. Interestingly, the discharge reaction does not generate bulk-phase metal. It is reported that bulk MF_2 is reduced to nanoscale M particles (≤ 10 nm) at the first discharge [4, 36-37, 58-59]. The origin of metal nanoparticle formation is estimated that electrons are tunneled from carbon conductor to the inside of poor electronic conductivity of MF_2 and forms M nanoparticle [37].

In order to understand the influence of metal nanoparticle formation on conversion voltage by DFT calculation, we replace bulk metal (M) in Eq. (1) with metal nanoparticle composed of n atoms ($M_n^{cubo\ or\ icosa}$)

$$n \cdot MF_2 + n \cdot 2Li \xrightarrow{n \cdot 2e^-} n \cdot 2LiF + M_n^{cubo\ or\ icosa} \quad (3)$$

where MF_2, Li, and LiF are bulk-phase forms. Then, we adopt the framework of mixing GGA and GGA + *U* proposed by Jain et al [46]. This method connect GGA and GGA + *U* energies, which are reasonable methods to calculate ground state properties of materials for delocalized electronic states (e.g., metal and LiF) and localized electronic states of d orbitals (e.g., transition metal difluorides), respectively [60]. The computational cell voltage (E^{nano}) is obtained as

$$E^{nano} = \frac{\left\{ \begin{matrix} \left[n \cdot G^{GGA}(2LiF) + G^{GGA}\left(M_n^{cubo\ or\ icosa}\right) \right] \\ -\left[n \cdot G_{renorm}^{GGA+U}(MF_2) + n \cdot G^{GGA}(2Li) \right] \end{matrix} \right\}}{-2n} \quad (4)$$

$G_{renorm}^{GGA+U}(MF_2)$ is calculated as $G^{GGA+U}(MF_2) - \Delta E_M$. ΔE_M connects GGA with GGA + *U* schemes and we adopt 1.723, 2.164 and 1.156 eV for Fe, Ni and Cu (per atom), when *U* are 4.0, 6.0 and 4.0 for Fe, Ni and Cu, respectively [46]. In order to confirm that the mixing framework is suitable for our calculations, we present the comparison of bulk-phase reaction voltage (Table 3.3) measured from GGA method, mixing GGA/GGA + *U* method, and Gibbs free energy of formation in thermodynamic table [61]. The voltage from mixing GGA/GGA + *U* method shows less than 0.09 V difference with respect to the voltage measured from thermodynamic table.

We find that E^{nano} for transition metal difluorides (FeF_2, NiF_2, and CuF_2) is lower than $E_{thermodynamic}^{bulk}$ as shown in figure 3.2(a).

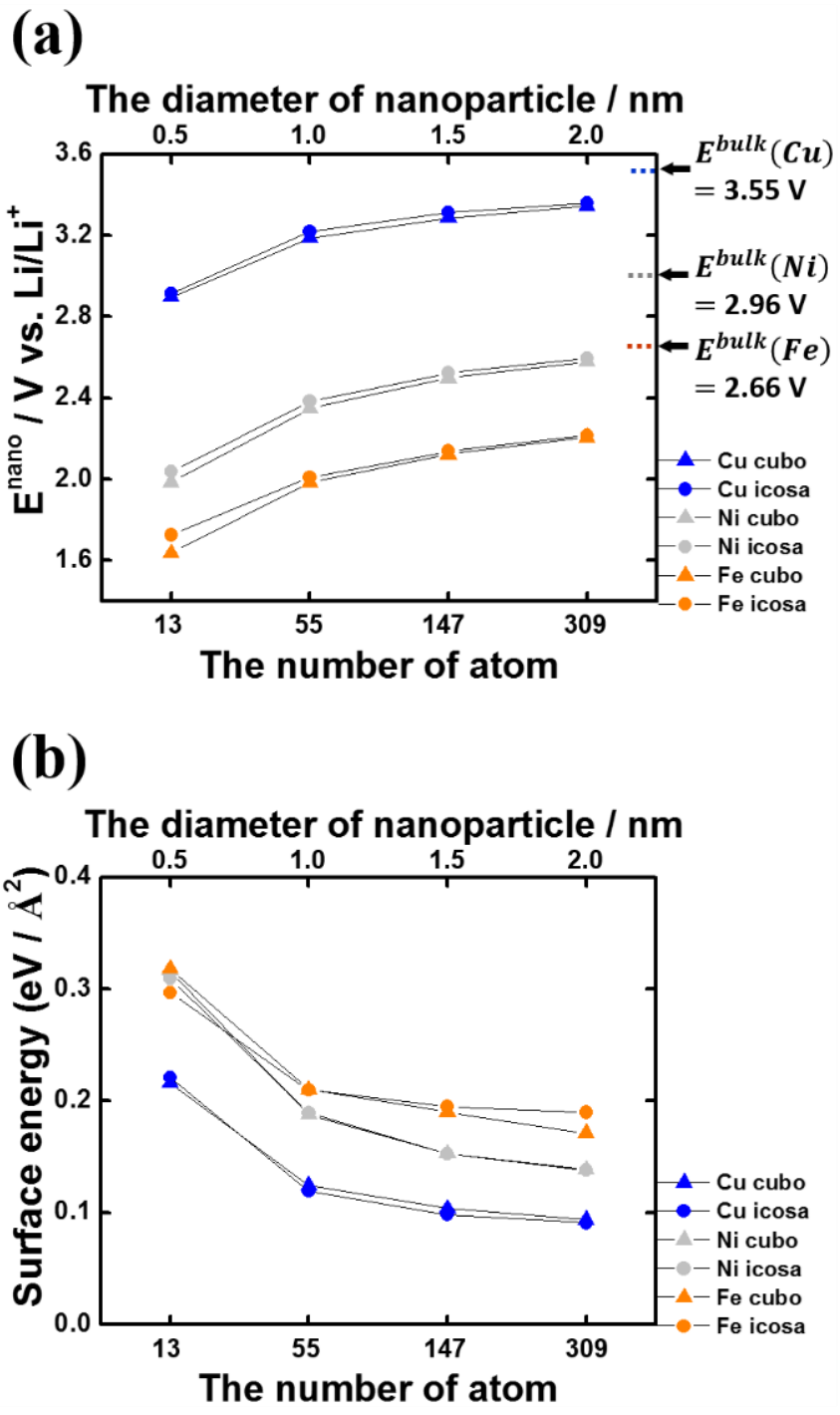

Figure 3.2 (a) Calculated conversion reaction voltage as a function of the size of M nanoparticle ($M = Fe, Ni\ and\ Cu$) formed. (b) Surface energy of M nanoparticle as a function of its size. The lower x-axis represents the number of atom contained in metal nanoparticle. The upper x-axis is the nanoparticle size in diameter which is approximate value. Detailed size information is demonstrated in Table 3.2

The voltage discrepancy between E^{nano} and $E^{bulk}_{thermodynamic}$ is 0.19-1.02 V for the metal nanoparticle size less than or equal to 2 nm. This low voltage upon the formation of metal nanoparticle resembles the conversion voltage measured from experiments, which also exhibits lower value than the thermodynamic voltage. Ko et al. displayed that the conversion voltage at the first discharge was evaluated to be 1.84 V which is lower than the thermodynamic voltage (2.66 V) on the lithiation reaction of FeF_2 (very slow C rate approximately C/1000) [35]. Another study used galvanostatic intermittent titration technique (GITT) on the conversion reaction of FeF_3 presented a voltage difference [62]. The second plateau (2.36 V) is corresponding to the reduction of Fe^{2+} to Fe, which is lower than the thermodynamic voltage. The voltage discrepancy is also commonly found in transition metal oxides cathode materials while nanoscale metal particles are formed during the lithiation [63-64]. Since the experimental voltage is measured from a distribution of nano-sizes metal nanoparticles when they were formed, it is impractical to directly compare the average experimental voltage to the calculated voltage at a certain size of metal particle. It is clear, however, the calculation supports the idea that the formation of metal nanoparticle during conversion reaction could have a lower voltage compared to the thermodynamic voltage of bulk-phase reaction.

In addition, our computational results indicate the particle size growth leads to increasing E^{nano}. E^{nano} approaches $E^{bulk}_{thermodynamic}$ when the particle size is larger than 2 nm (figure 3.2(a)) because nanoscale property of metal resembles the property of bulk metal as the particle size increases. It is reported that when the metal particle gets larger, the integrity of metal nanoparticle stabilizes because its Gibbs energy per atom decreases (or increment in cohesive energy), and eventually reaches to the stability of bulk metal [48]. This thermodynamic property is associated with Eq. (4) that Gibbs energy of $M_n^{cubo\ or\ icosa}$ per atom approached more negative

value when the particle size increases and results in the increment of E^{nano}. In calculation, we did not presume LiF as a nano-size phase because LiF is typically a bulk matrix in which metal nanoparticles are distributed.

Importantly, our results also attribute lower conversion reaction voltage to the surface energy of metal nanoparticle ($G_{surface}^{nano}$). The surface energy as an energy penalty toward the reaction energy needs to be provided to the metal nanoparticle to form during the conversion reaction. We calculate the surface energy of M nanoparticle ($M = Fe, Ni\ and\ Cu$) as a function of its size [65]

$$G_{surface}^{nano} = \frac{G^{GGA}\left(M_n^{cubo\ or\ icosa}\right) - n \cdot G^{GGA}(M)}{4\pi r^2} \qquad (5)$$

where $G^{GGA}\left(M_n^{cubo\ or\ icosa}\right)$ and $G^{GGA}(M)$ are the Gibbs energy of M nanoparticle composed of n atoms and M bulk metal per atom ($M = Fe, Ni\ and\ Cu$), respectively. r is the average radius which is measured by the distance between the center and vertex atoms of a relaxed nanoparticle (Table 3.2). It is noted that the surface energy increases as the nanoparticle size decreases (figure 3.2(b)), which results in the decrement of reaction energy and affects the reduction of conversion reaction voltage (figure 3.2(a)). This trend is correlated with the fact that while the particle is getting smaller, the fraction of thermodynamically unstable surface atoms is increasing with respect to the fraction of relatively stable bulk atom. The cuboctahedron consisting of 309 atoms has 108 atoms (35%) on the surface. As the size decreases, the fraction of surface atoms increases to 92% for the cuboctahedron with 13 atoms. We systematically shows the energy penalty in the conversion reaction associated with the formation of metal nanoparticles by first principles, which was conceptually discussed in Cabana et al.'s report [2]. Although the surface energy of nanoparticle is primarily studied in our work, other factors including the crystallinity of

the material [66], interfacial energy [67-68], or electronic conductivity [5] in nanoscale LiF/M framework can also affect the value and shape of reaction voltage.

3.3.3 Particle size and electrochemical electrode voltage

The conversion reaction of transition metal difluoride involves a local phase nucleation and evolution during lithiation process. Metal difluoride converts into metal nanoparticle and LiF phases during lithiation. In order to study the correlation of the metal nanoparticle formation with the conversion reaction voltage in the fully lithiated status, CuF_2/C and NiF_2/C are galvanostatically lithiated (figure 3.3).

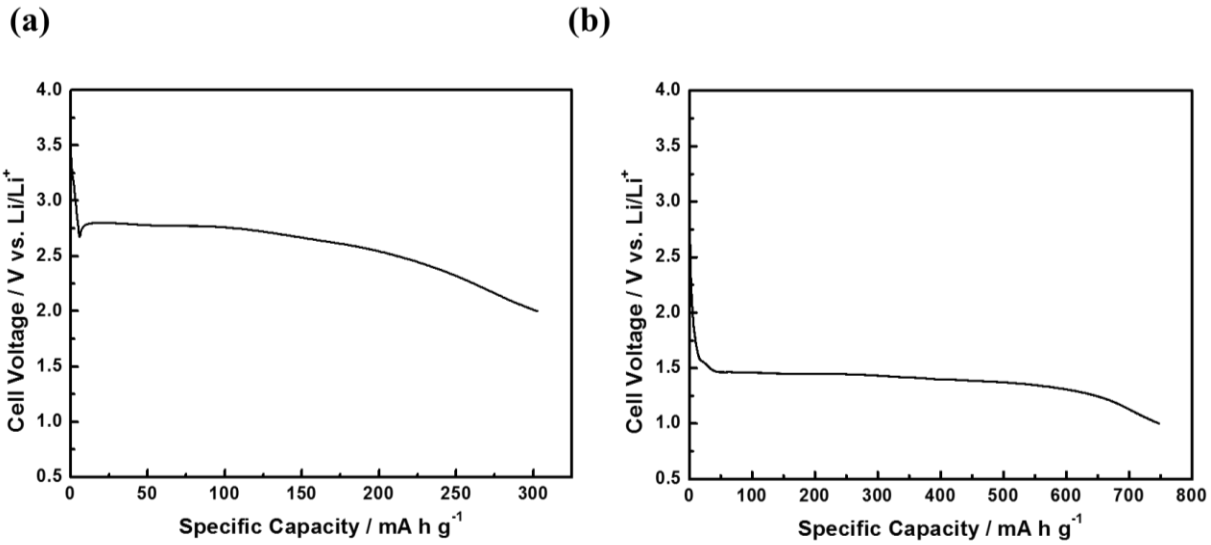

Figure 3.3 The first discharge of CuF_2/C (a) and NiF_2/C (b)

Various TEM/STEM techniques including selected area electron diffraction (SAED) patterns, ADF-STEM images and EELS spectra are used in order to study the structural and morphological changes of the CuF_2/C and NiF_2/C electrodes during lithiation. We have taken 15 different ADF-STEM images, EELS spectra, and 10 different SAED patterns from various regions of the samples

and the representative of the observed images, EELS spectra, and SAED patterns are presented here. The bright contrasts in the ADF-STEM image (figure 3.4(a)) corresponds to the area where the highest concentration of Cu can be seen, as ADF- STEM image contrast is highly sensitive to atomic number (~$Z^{1.7}$).

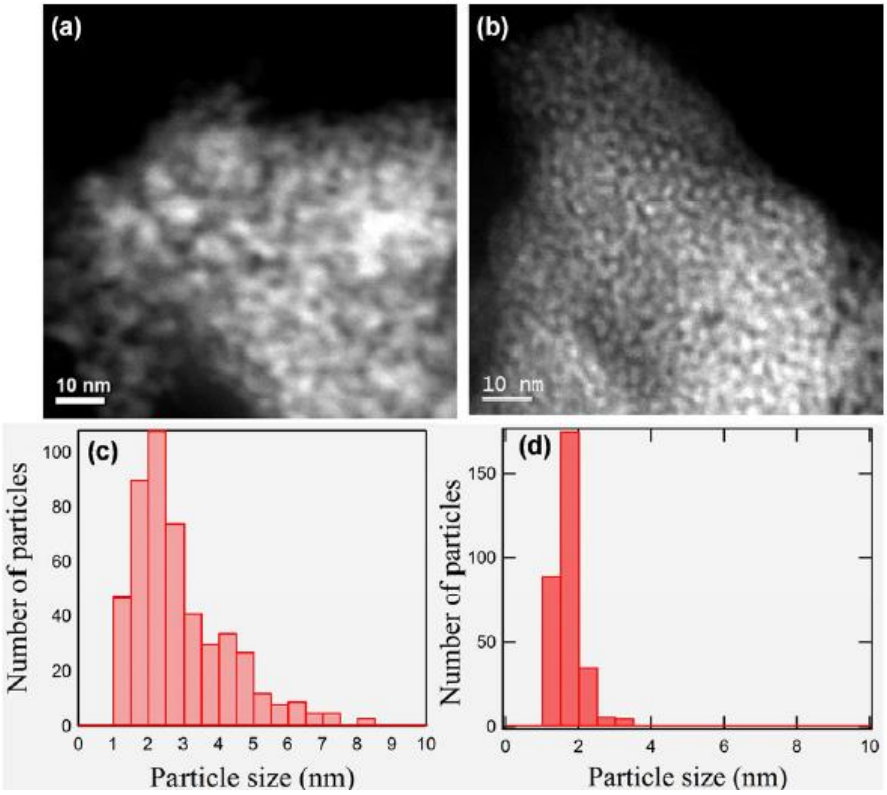

Figure 3.4 Representative ADF-STEM images of (a) lithiated CuF_2/C, and (b) lithiated NiF_2/C. The particle size distribution obtained from several ADF-STEM images of (c) lithiated CuF_2/C, and (d) lithiated NiF_2/C

The ADF-STEM image of the lithiated NiF_2/C in figure 3.4(b) shows the distribution of Ni nanoparticles (bright contrast) in LiF matrix. It is observed that lithiated CuF_2/C and lithiated NiF_2/C are composed of Cu and Ni with average particle sizes of ~ 2.5 nm and ~ 1.5 nm, respectively. The particle size distributions of Cu and Ni are obtained from several ADF-STEM images shown in figure 3.4(c, d). The lithiated CuF_2/C contains broad particle size ranges from 1

to 10 nm whereas lithiated NiF_2/C consists of Ni particle sizes range from 1 to 5 nm. The distinction in average particle sizes are attributed to the differences in diffusion rates of Cu and Ni ions that Cu has a higher diffusivity, thus forming large particles [36-37]. The SAED patterns of the pristine CuF_2/C and NiF_2/C nanocomposites confirm the existence of single phase with a monoclinic and tetragonal–rutile structure as shown in figure 3.5(a) and 3.5(b) respectively.

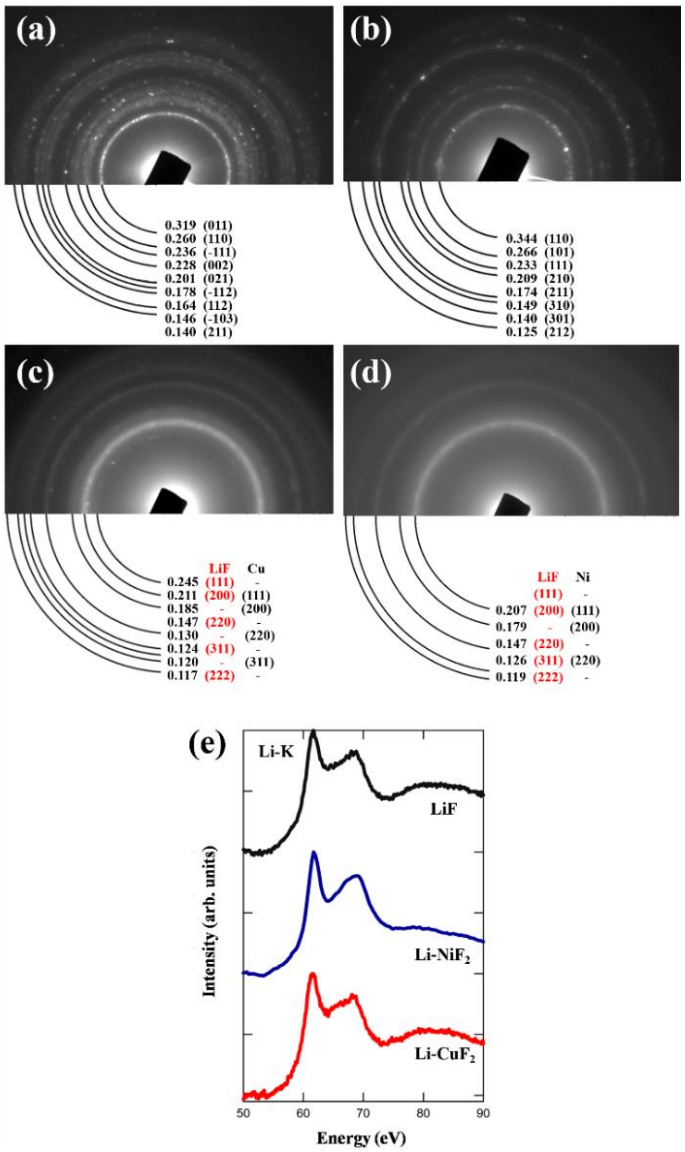

Figure 3.5 Representative SAED patterns of (a) pristine CuF_2/C, (b) pristine NiF_2/C, (c) lithiated CuF_2/C, (d) lithiated NiF_2/C, and (e) Li-K edge EELS spectra of the lithiated CuF_2/C (Li-CuF_2), lithiated NiF_2/C (Li-NiF_2), and reference LiF

Upon lithiation, CuF_2/C with monoclinic structure converts into cubic structure consists of metallic Cu and LiF (figure 3.5(c)). Similarly, NiF_2 with tetragonal-rutile structure transforms into metallic Ni and LiF upon lithiation, presented in figure 3.5(d). The presence of LiF in lithiated CuF_2/C and NiF_2/C is further verified by the characteristic near-edge fine structure in the Li K-edge spectra (figure 3.5(e)).

Interestingly, large Cu particles are found to be isolated and be dispersed in carbon matrix. Figure 3.6 shows the ADF image and the corresponding energy-dispersive X-ray (EDX) spectra of the lithiated CuF_2/C.

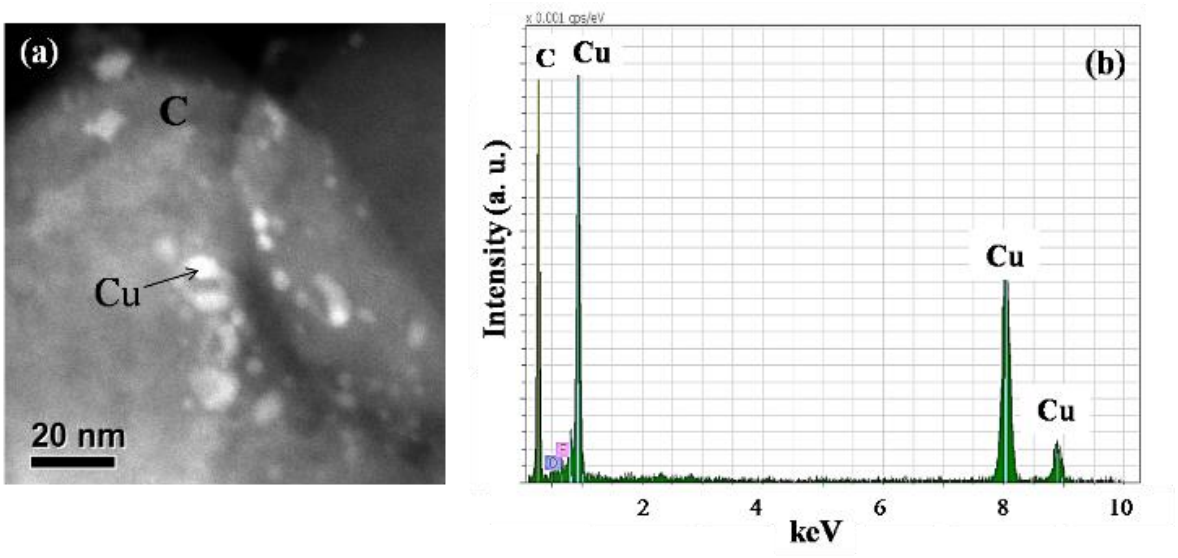

Figure 3.6 (a) Representative ADF-STEM and (b) EDX spectrum of the lithiated CuF_2/C showing the presence of large Cu metal (about 10 nm) on carbon matrix

It is observed that large Cu particles with ~10 nm are distributed in carbon matrix. This suggests large Cu particles are being isolated from LiF after first discharge; therefore, they most probably have less chance to participate in the re-conversion reactions.

Additionally, PITT is applied to CuF_2/C and NiF_2/C cells in order to measure conversion reaction voltages under near-equilibrium state (figure 3.7).

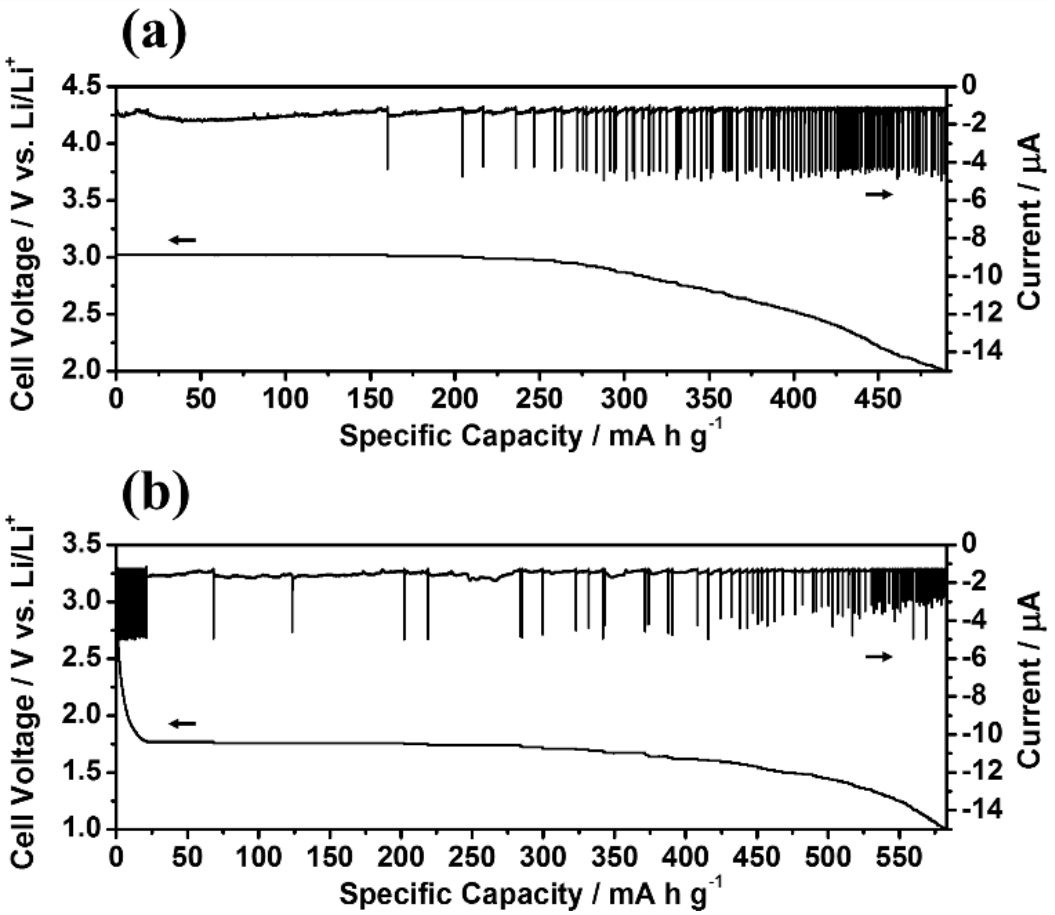

Figure 3.7 PITT discharge of (a) CuF_2/C and (b) NiF_2/C

This technique controls small voltage steps and monitors the current correlated with the reaction. We apply the voltage step with 10 mV interval. The voltage step does not proceed to the next step until the discharge current declines to a current limit of -1.1 and -1.3 μA for CuF_2/C and NiF_2/C cells, respectively (C/1000 for both cells). PITT takes ~ 765 and ~ 909 hours for the first discharge of CuF_2/C and NiF_2/C, respectively. In case of CuF_2/C, the open circuit voltage (OCV) is 3.09 V and the conversion reaction proceeds without any significant current decrease to the current limit at 3.02 V (figure 3.7(a)). The reaction continues at the following voltage steps with shortening plateaus. NiF_2/C shows the OCV of 3.07 V and the conversion reaction initiates at 1.77 V after rapid voltage drop (figure 3.7(b)). From our PITT results, we confirmed that the conversion

reactions of both CuF_2/C and NiF_2/C occur at lower voltages than the thermodynamic bulk-reaction voltages ($E^{bulk}_{theoretical}$ (CuF_2) = 3.55 V and $E^{bulk}_{theoretical}$ (NiF_2) = 2.96 V). The formation of metal nanoparticle has a strong influence on the conversion voltage which is lower than thermodynamic voltage of bulk-phase reaction.

3.3.4 Rechargeable behavior of NiO-CuF_2 conversion material

According to the previous reports, two main factors can result in a poor cycling performance of CuF_2: (i) Cu dissolution within the operating voltage window (2.0 - 4.0 V) [37] and (ii) isolated large Cu particle formation upon lithiation [36]. The linear potential sweep voltammogram for Cu demonstrates that Cu dissolves at ~ 3.5 V within the operating voltage window of CuF_2 electrode (figure 3.8).

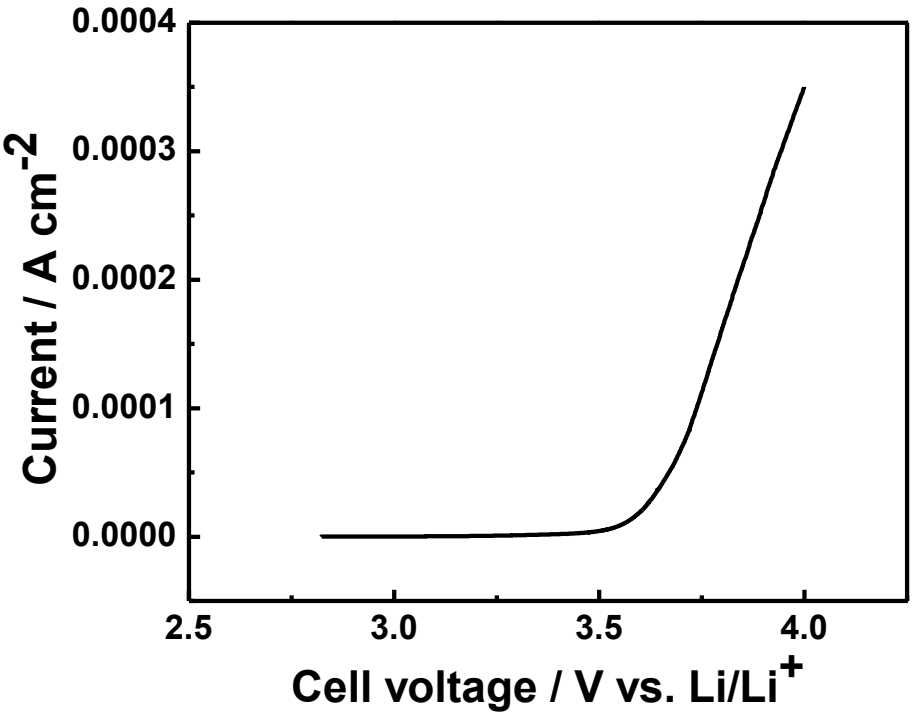

Figure 3.8 Linear potential sweep voltammogram for Cu foil

In addition, our ADF-STEM images observe a bimodal Cu particle size (figure 3.4(a) and figure 3.6(a)). The small Cu particles (~2.5 nm in average) are distributed in microstructure of LiF (figure 3.4(a)), which is similar to the other conversion materials including FeF_2 [69-70]. However, large Cu particles (~10 nm) are segregated from LiF and located in carbon matrix (figure 3.6(a)). It is noteworthy that based on our ADF-STEM image, the majority of Cu particles are observed to be small (~2.5 nm in average) and embedded in LiF (figure 3.4(a)). This contrasts to the previous TEM work on CuF_2, which showed that only isolated large Cu particles (5-12 nm) form upon lithiation.[36]

CuF_2 is intrinsically non-reversible conversion material in contrast to FeF_2 and NiF_2, however, it has the highest thermodynamic voltage with the theoretical specific capacity of 528 mA h g^{-1}. In the present work, we have developed a novel reversible NiO-CuF_2/C electrode. Figure 3.9 shows the electrochemical voltage profile of CuF_2/C and NiO-CuF_2/C electrodes in the voltage window between 2.0 - 4.0 V at a C/35 rate.

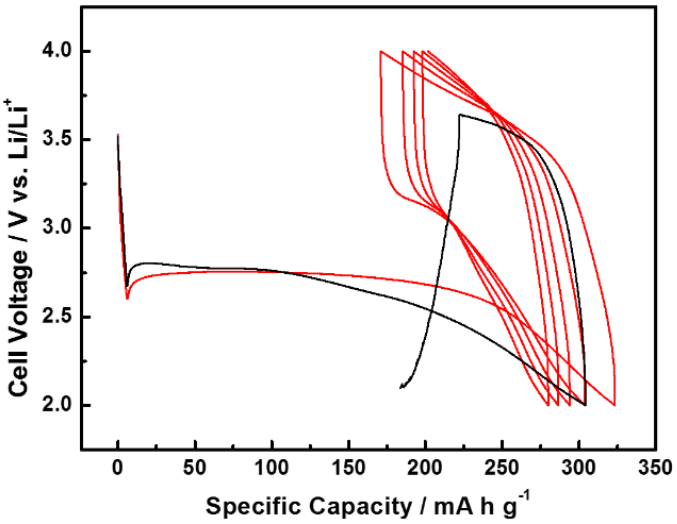

Figure 3.9 Voltage profiles of CuF_2/C and NiO-CuF_2/C electrodes

CuF_2/C delivered 303 mA h g^{-1} discharge capacity (57% of theoretical capacity). Similarly, NiO-CuF_2/C electrode shows the first discharge capacity of 323 mA h g^{-1} (61 % of the theoretical capacity). Both electrodes show quite low voltage plateaus (2.75 V and 2.77 V for NiO-CuF_2/C and CuF_2/C, respectively) compared to the thermodynamic voltage of bulk-phase reaction (3.55 V). However, NiO-CuF_2/C electrode displays a reversible conversion reaction with specific capacity of 152 mA h g^{-1} at the first charge. During the charging process, CuF_2/C electrode voltage starts to drop from ~3.64 V resulting in a charge failure. We ascribe this to Cu^{2+} dissolution from the cathode.

In order to gain in-depth insights into the effects of NiO on CuF_2 reversibility, the distribution of Cu and Ni in the lithiated NiO-CuF_2/C sample has been studied using STEM-EELS elemental mapping. As lithium and fluoride-base compounds are extremely beam sensitive, we have optimized the electron dose and spatial resolution to minimize the beam damage in this work. As such, the STEM-EELS spectrum image is taken with a total electron dose of $3x10^4$ e/nm^2. A representative ADF-STEM image and the corresponding Cu-$L_{2,3}$, and Ni-$L_{2,3}$ edge elemental maps are shown in figure 3.10.

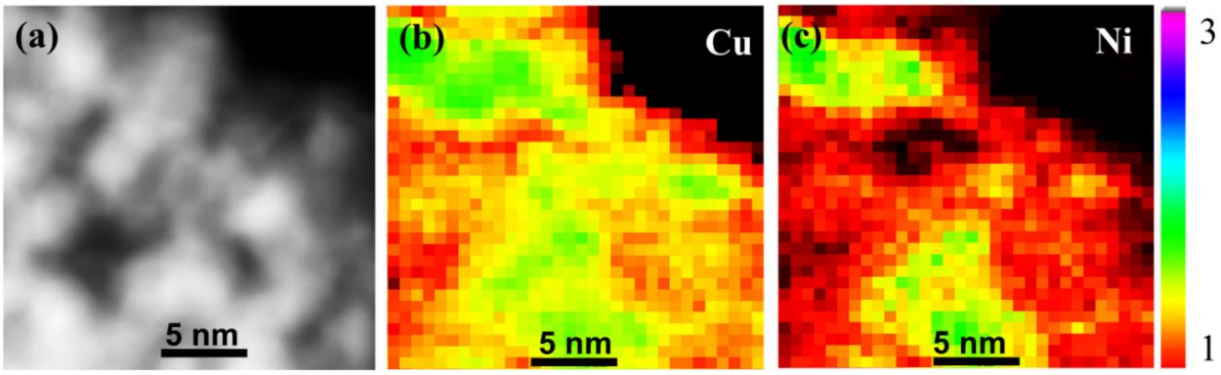

Figure 3.10 Representative ADF-STEM image of (a) the first discharged NiO-CuF_2/C and the corresponding elemental maps for (b) Cu-L , and (c) Ni-L

It is observed that the bright contrast is attributed to the areas where the highest concentration of Cu is in. It is interesting that Ni rich areas are located in the same regions as Cu rich areas. It also indicates that the lithiation process mostly occurs in areas with high NiO content. We propose that NiO as an artificial solid electrolyte interphase (SEI). NiO is insoluble solid phase and electrochemically inactive within the voltage window (2.0 - 4.0 V), which reduces the direct contact between the cathode and the electrolyte, and possibly alleviates Cu dissolution in the electrolyte. It has been reported that metal oxides could suppress metal ion dissolution into the electrolyte [71-73]. In addition, the large Cu particles (~10 nm) in carbon matrix are observed in the first discharged NiO-CuF_2/C. Our ADF-STEM and the corresponding EELS spectra of the first discharged NiO-CuF_2/C (figure 3.11 (a, c, d)) show the presence of large Cu particles (~10 nm) distributed in carbon matrix, similar to what we find from the lithiated CuF_2/C (figure 3.6(a)).

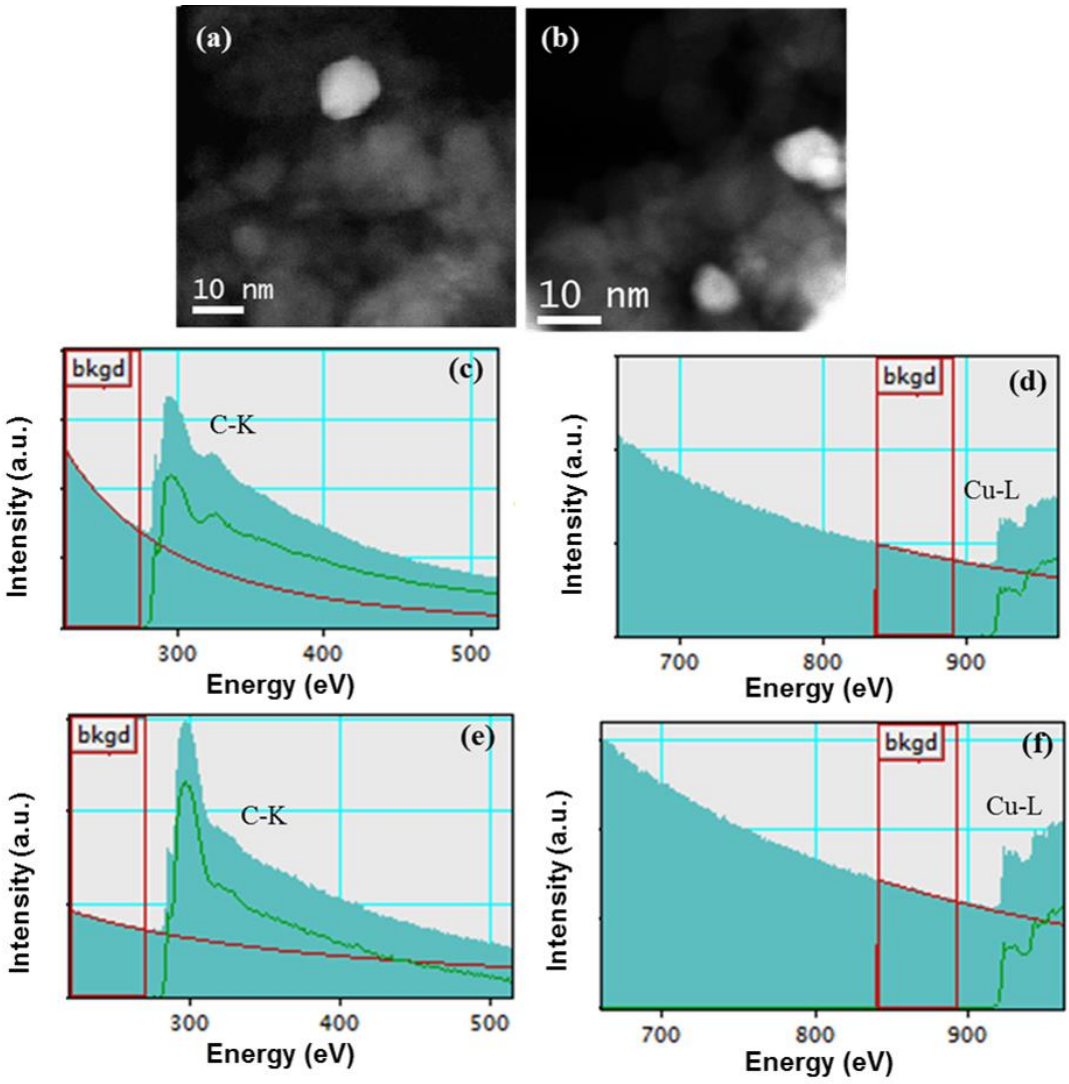

Figure 3.11 ADF-STEM of the first discharged (a) and the first charged NiO-CuF_2/C (b). C-K edge EELS spectra of the first discharged (c) and the first charged (e) NiO-CuF_2/C. Cu-L edge EELS spectra of the first discharged (d) and the first charged (f) NiO-CuF_2/C

Interestingly, the large Cu particles are still present in the first charged NiO-CuF_2/C (figure 3.11 (b, e, f)). This implies that large Cu particles on the carbon domain have less opportunity to participate in further cycles.

To investigate the extent of Cu dissolution into the electrolyte, elemental analysis of the electrolyte is performed using ICP-OES. The first cycled (discharge/charge) CuF_2/C and NiO-CuF_2/C cells are disassembled and their electrolytes are collected. It is noted that CuF_2/C cell

cannot be charged up to 4 V because of its non-reversible feature in contrast with NiO-CuF_2/C cell. For that reason, the electrolyte from CuF_2/C cell is collected after the CuF_2/C cell fails during the charging process. We find that Cu dissolution into the electrolyte is alleviated when the electrode is coated with NiO (figure 3.12).

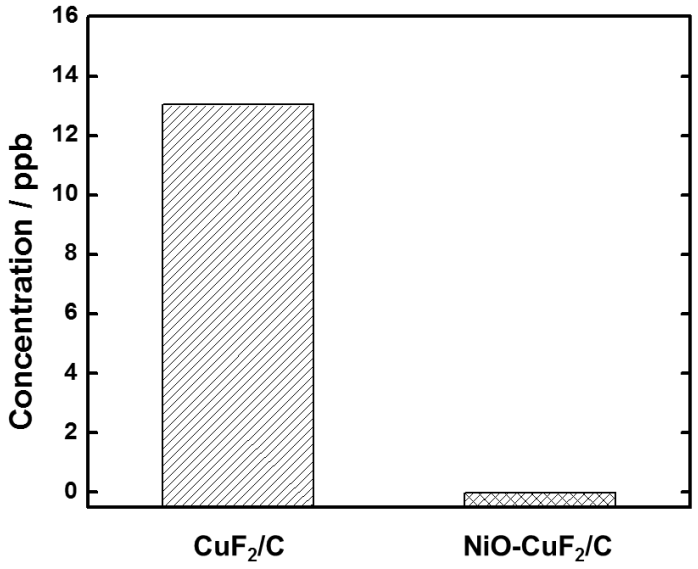

Figure 3.12 Cu dissolution into the electrolyte from CuF_2/C and NiO-CuF_2/C electrodes

The concentration of Cu in the electrolyte when using CuF_2 electrode is measured to be ~13 ppb, however, NiO-CuF_2 electrode shows the Cu concentration of ~ 0 ppb. This observation directly indicates NiO coating suppresses the Cu dissolution and alleviate the electrode degradation.

Recently, a bimodal-size evolution of Ni nanoparticle from NiO-NiF_2/C electrode has been reported by pair distribution function (PDF) analysis that NiO possibly facilitates the conversion process by providing electronic conductivity [5]. NiF_2/C electrode, however, is only converted into smaller Ni nanoparticles because of its insulating property. In order to investigate the phase transformation in CuF_2/C and NiO-CuF_2/C, we also conduct PDF for (a) first discharged CuF_2/C

and (b) first discharged NiO-CuF_2/C (c) first charged NiO-CuF_2/C, and (d) second discharged NiO-CuF_2/C samples, as shown in figure 3.13.

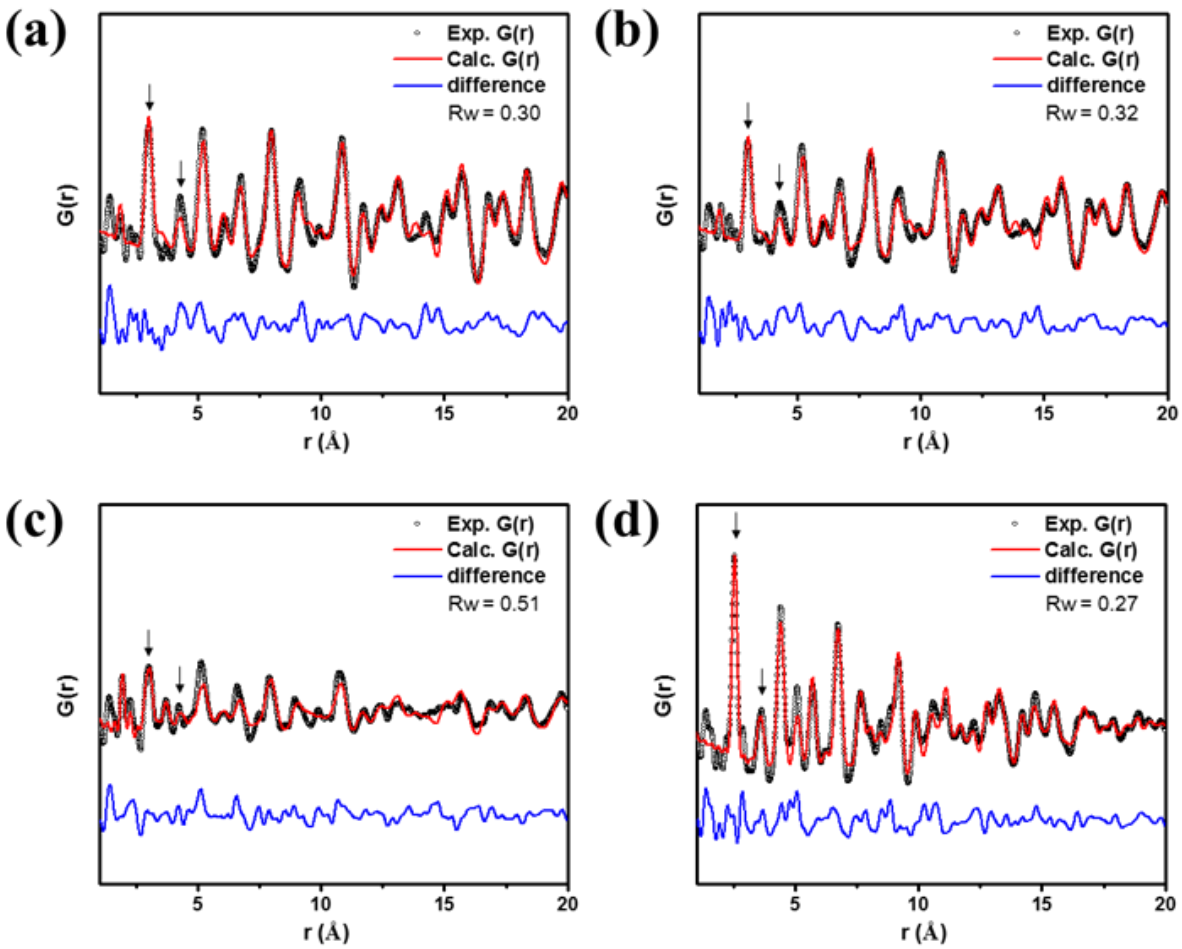

Figure 3.13 Experimental PDF (Exp. G(r)), refined fit (Calc. G(r)), and difference between Exp. G(r) and Calc. G(r). The first discharged CuF_2/C (a), first discharged NiO-CuF_2/C (b), first charged NiO-CuF_2/C (c), and second discharged NiO-CuF_2/C (d)

We measure the Cu phase with average nanoparticle size of ~ 2.3 nm from the second discharged NiO-CuF_2/C (figure 3.13 (d)). Cu_2O are mainly found from other samples instead of Cu phase (figure 3.13 (a-c)) which most likely have been resulted from the contamination of samples by air when they are kept in the Kapton capillaries [37]. Although more PDF work is still needed, our PDF refinement on the second discharged NiO-CuF_2/C confirms the formation of Cu

nanoparticle, which suggests NiO facilitates the CuF_2/C reversible reaction.

3.4 Conclusions

In this study, we combine first principles calculations and experiments with the characterization technique to analyze the conversion reaction voltage for MF_2 ($M = Fe, Ni\ and\ Cu$) in Li-ion batteries. Based on our calculations, the voltage heavily depends on the size of metal nanoparticle generated. The formation of metal nanoparticle affects the conversion reaction voltage which is lower than the thermodynamic voltage of a bulk-phase reaction. We propose the surface energy of metal nanoparticle as an energy penalty against the free energy of reaction, bringing about a low voltage. Our ADF-STEM images demonstrate Cu and Ni nanoparticle formations for the first discharged CuF_2 and NiF_2, respectively. Similarly, the PITT results show that the conversion reactions of CuF_2 and NiF_2 occur at low voltages as a result of metal nanoparticle formation.

Moreover, we propose a rechargeable CuF_2 electrode by introducing NiO. NiO reduces the immediate contact between the CuF_2 and electrolyte, thus suppresses the Cu dissolution. We suggest NiO can be used as an artificial SEI layer to improve the reversibility of Cu-based conversion materials. Further research of surface coatings will provide a breakthrough in the class of high energy density conversion materials.

Chapter 3, in full, is a reprint of the material “Revisiting the conversion reaction voltage and the reversibility of the CuF_2 electrode in Li-ion batteries” as it appears in the Nano Research, Joon Kyo Seo, Hyung-Man Cho, Katsunori Takahara, Karena W. Chapman, Olaf J. Borkiewicz, Mahsa Sina, Y. Shirley Meng, 2017. The dissertation author was the primary investigator and author of this paper.

Chapter 4: Intercalation and conversion reactions of nanosized β-MnO_2 cathode in the secondary Zn/MnO_2 alkaline battery

4.1 Introduction

Ever since Lewis Urry invented a primary Zn/MnO_2 alkaline battery back in the late 1950's, it has been widely adopted as an energy source for low-power electronics. Recently, the Zn/MnO_2 aqueous battery is gaining attention as a rechargeable energy storage for smart grid technology.[13, 74-75] Compared to a Li-ion battery, a Zn/MnO_2 aqueous battery has several advantages such as low material cost, high energy density, better safety, and non-toxicity. To illustrate, the current rechargeable Zn/MnO_2 aqueous battery technology costs under $90 per kWh,[13] whereas the cost for Li-ion batteries are unlikely to fall below $200 per kWh.[75] In addition, Zn/MnO_2 aqueous battery operates with water-based electrolytes, furnishing a higher degree of safety making them an attractive option for grid-scale usage in residential homes and dense urban areas.

MnO_2 exists in multiple crystallographic structures including α-, β-, γ-, δ-, λ-, and R-MnO_2. These MnO_2 polymorphs are defined by different connection of the basic structural unit, MnO_6 octahedron, and various types of tunnels within the crystal structure.[76-77] Electrochemical reactions vary in Zn/MnO_2 aqueous batteries dependent on the phase of MnO_2 and electrolyte used, however, the most common discharge mechanism of MnO_2 involves a homogeneous reaction and followed by a heterogeneous reaction.[78-81] Once the discharge initiates, protons intercalate into tunnels of MnO_2 through the homogeneous reaction without Mn-O bond breakage, however the bonds begin to break in the heterogeneous reaction as the discharge proceeds further leading to eventual deformation of the lattice. During the homogeneous reaction, the voltage changes rapidly, however the heterogeneous reaction manifests the voltage plateaus due to two-phase reactions.

Recently, many studies have reported the development of rechargeable Zn/MnO_2 aqueous batteries which utilize mild acidic electrolytes.[14, 74-75, 82-86] Lee et al. describe that a Zn/α-MnO_2 system in $ZnSO_4$ electrolyte involves Zn/Zn^{2+} redox at the anode and α-MnO_2/Mn^{2+} at the cathode. An additional reversible phase of $Zn_4(OH)_6(SO_4)\cdot 5H_2O$ (zinc hydroxide sulfate) precipitates on the cathode's surface due to Zn^{2+} and SO_4^{2+} in an aqueous electrolyte.[82] Pan et al. report that the rechargeability of Zn/α-MnO_2 aqueous battery is significantly improved by adding $MnSO_4$ salt in the $ZnSO_4$ electrolyte.[84] They describe the same redox reactions proposed by Lee et al. with an undefined hydration number for the zinc hydroxide sulfate. However, the addition of the $MnSO_4$ salt in the electrolyte suppresses the dissolution of Mn^{2+} and enables longevity of over 5000 cycles.

In addition to the acidic solutions, the basic solutions have been investigated to understand the rechargeability of Zn/MnO_2 aqueous batteries. Gallaway et al. probed the phase transformation of the cathode/anode in a commercial alkaline 'AA' cell.[14] They observed $ZnMn_2O_4$ (hetaerolite) forming in the cathode, implying that it is a side product of the chemical reaction between MnOOH and $Zn(OH)_4^{2-}$. The $Zn(OH)_4^{2-}$ (zincate ion) is generated from $Zn(OH)_4^{2-}/Zn$ redox at the Zn anode which then migrates to the cathode where MnOOH is formed after MnO_2 is reduced. The $ZnMn_2O_4$ phase produced is electrochemically inactive phase and degrades the cycle performance of Zn/MnO_2 aqueous batteries. Turney et al. reported that the formation of $Zn(OH)_4^{2-}$ is favorable at the Zn anode where OH^- species are concentrated inducing the production of $ZnMn_2O_4$.[75] In another study, Hertzberg et al. found that the combination of LiOH and KOH as electrolytes in a Bi species incorporated Zn/β-MnO_2 alkaline battery improved the rechargeability demonstrating a reversible single-electron reaction for 60 cycles.[85] They proposed that a reversible reaction occurs during the cycling between the reduced phases ($Mn(OH)_2$ and $LiMn_2O_4$) and the oxidized phase (δ-MnO_2). This reaction mechanism, however, is contentious due to δ-MnO_2 being measured

solely during the first charged state and not in any of the subsequent cycles.

Optimizing the utilization of two electrons in MnO_2 is an essential for high-energy stationary storage. Many studies have demonstrated that the capacity increases using nanostructured materials.[77, 87-88] Chen et al. reported that nanosized γ-MnO_2 shows almost two-times higher discharge capacity than bulk γ-MnO_2.[87] They suggested that broad surface area in nano-scale MnO_2 enlarges contact between MnO_2 active materials and an electrolyte which lowers internal resistance and facilitates proton diffusion. In order to utilize large capacity and improve the reversibility of reactions in alkaline solutions, we synthesized nanoscale β-MnO_2 and assembled the Zn/β-MnO_2 alkaline battery with the LiOH and KOH electrolytes. The average discharge capacity shows 280 mAh g^{-1} throughout 100 cycles, which is higher than the capacity of the battery made of commercial β-MnO_2 by 116 mAh g^{-1}. Furthermore, we studied the phase transformation of nanosized β-MnO_2 in Zn/β-MnO_2 alkaline battery. The result indicates that the proton intercalation reaction is followed by two-phase conversion reactions at the first cycle, however, a different reaction mechanism is observed at the hundredth cycle. Li and H co-inserted λ-MnO_2 spinel and λ-MnO_2 spinel are formed at the hundredth discharged and charged state, respectively. Lastly, we incorporated β-MnO_2 cathode with 4% mole fraction of Bi_2O_3 to enhance the electrochemical performance. The average discharge capacity is 369 mAh g^{-1} throughout 100 cycles. Bi_2O_3 additive reacts with $Zn(OH)_4^{2-}$, which alleviates the capacity loss driven by the formation of irreversible $ZnMn_2O_4$.

4.2 Experimental

β-MnO_2 was synthesized by a thermal decomposition process beginning with dissolving 10 g of $Mn(NO_3)_2 \cdot 4H_2O$ in 16 mL deionized (D.I.) water. The solution was stirred with a magnetic

stir-plate while being heated to increase the reaction temperature to 140 °C. Once the temperature reached 140 °C, the reaction was held at that temperature until the initially clear solution developed a black color with high viscosity indicating the oxidation to the Mn^{4+} state. Then, the black solution was transferred to a preheated vacuum oven and kept at 125 °C overnight to facilitate complete drying of the MnO_2 product and to eliminate excess NO_x gases. The sample was removed from the vacuum oven after 12 h and transferred to a preheated box furnace heated to 125 °C. The temperature of the oven was programmed to increase up to 325 °C with a step of 5 °C/min, then to hold the temperature at 325 °C for 5 h. After natural cooling, the solid sample was ground with a mortar and a pestle to turn it into fine powder.

The working electrode is composed of the β-MnO_2 active material (synthesized β-MnO_2, commercial β-MnO_2, or synthesized β-MnO_2 with 4 % mole fraction of Bi_2O_3), carbon black Super-P, and polytetrafluoroethylene (PTFE) with a 60:30:10 weight ratio. The electrode was implanted onto a Ni foam current collector and pressed using a hydraulic press with a pressure of eight tons. The pressed electrode was then covered with one layer of polyvinylidene chloride, two layers of nonwoven separator (FS 22145 from Freudenberg LLC) and a Zn plate counter electrode. They were sandwiched between two acrylic plates, which were held together tightly with screws. After an assembly, the battery was immersed in a 20 mL beaker with 10.5 mL of 1 M KOH and 3 M LiOH electrolyte. Parafilm was used to seal the beaker. All batteries in this study were tested at C/10 current rate for the first cycle and C/5 for the following cycles. Considering the rate capability tests for synthesized β-MnO_2 with/without Bi_2O_3, the discharge/charge process was carried out over the course 20 cycles for each stage except for the last stage (9 cycles). Constant current rates were calculated using the theoretical two-electron capacity of MnO_2 which is 616 mAh/g. The voltage range used is $0.5 < V < 1.8$. The constant voltage of 1.8 V was applied at the end of constant

current charging until the current decreased to 10% of the current rate. The batteries were cycled using an Arbin battery cycler at room temperature. In addition, the electrochemical stability window of electrolyte was measured using a Solartron 1260 Impedance Analyzer. The linear sweep voltammetry was taken on Ni foam electrodes compared against Hg/HgO reference electrode in 1M KOH and 3M LiOH electrolyte at a scan rate of 1 mV/s.

The in-house XRD samples were synthesized and commercial β-MnO_2 powder, and cycled β-MnO_2 electrodes. Cycled electrodes were collected at 1.25 V, 1.05 V, 0.5 V and 1.8 V during the first cycle of synthesized β-MnO_2 in Zn/β-MnO_2 alkaline batteries. Those electrodes were washed with running D.I. water and soaked in the D.I. water overnight. After washing, electrodes were dried in 60 ℃ for 3 hours. All the XRD data were collected at an ambient temperature on a Bruker D8 Advance diffractometer at 40 kV, 40 mA for Cu Ka (λ = 1.5418 Å), with a scan speed of 5 s per step, a step size of 0.02° in 2θ, and a 2θ range of 10–80°.

Cycled electrodes of synthesized β-MnO_2 collected at the hundredth discharge/charged state were selected for synchrotron XRD analysis. The cycled electrodes were washed with running D.I. water and soaked in the D.I. water overnight. After washing, electrodes were dried at 60 ℃ for 3 hours in the oven. Synchrotron XRD spectra were acquired at the Advanced Photon Source (APS) at Argonne National Laboratory (ANL) on beamline 11-BM (λ= 0.4145 Å). The beamline uses a sagittal focused X-ray beam with a high precision diffractometer circle and perfect Si(111) crystal analyzer detection for high sensitivity and resolution. Synchrotron XRD spectra were plotted based on λ= 1.5418 Å to compare with the in-house XRD spectra.

XPS was performed using a Kratos AXIS Supra at the Laboratory for Electron and X-ray Instrumentation. Cycled samples were prepared by washing with running D.I. water, soaking the

electrode in the D.I. water overnight, and drying in 60 ℃ for 3 hours. The XPS was operated using Al anode source at 15 kV. All XPS measurements were collected with a 300 μm by 700 μm spot size without using a charge neutralizer during acquisition. We used a step size of 0.3eV for survey scan and 0.1 eV for high-resolution scans. All the spectra was calibrated with carbon 1s sp^3 at 284.8 eV.

The SEM/EDS samples selected were synthesized and commercial β-MnO_2 powders, Bi_2O_3 and immersed Bi_2O_3 powder in 6M Zn nitrate solution. The sample of immersed Bi_2O_3 powder was prepared by washing with running D.I. water, soaking the powder in the D.I. water overnight, and drying in 60 ℃ for 3 hours in the oven. All powder samples were loaded onto a SEM holder using a carbon adhesive tape. The images were obtained using a 15 kV energy source using the FEI/Phillips XL30 ESEM.

First principles calculations were conducted based on spin-polarized GGA+*U* [40-41] using the Perdew–Burke–Ernzerhof of exchange and correlation functionals.[42] A plane-wave basis set and the projector-augmented wave (PAW) method [43-44] were used as parameterized in the Vienna *ab initio* simulation package (VASP).[45] A gamma point mesh is performed with 7 × 7 × 7 *k*-points for λ-MnO_2. All the atoms were fully relaxed to calculate the optimized structure with a cutoff energy of 1.3 times the maximum cutoff specified by the pseudopotentials on a plane-wave basis set. The scheme proposed by Persson et al[89] was adopted in order to obtain an accurate standard Gibbs free energy of formation.

4.3 Results and Discussion

4.3.1 The influence of a particle size

The powder of synthesized and commercial β-MnO_2 are measured by in-house X-ray diffractometer as shown in figure 4.1(a).

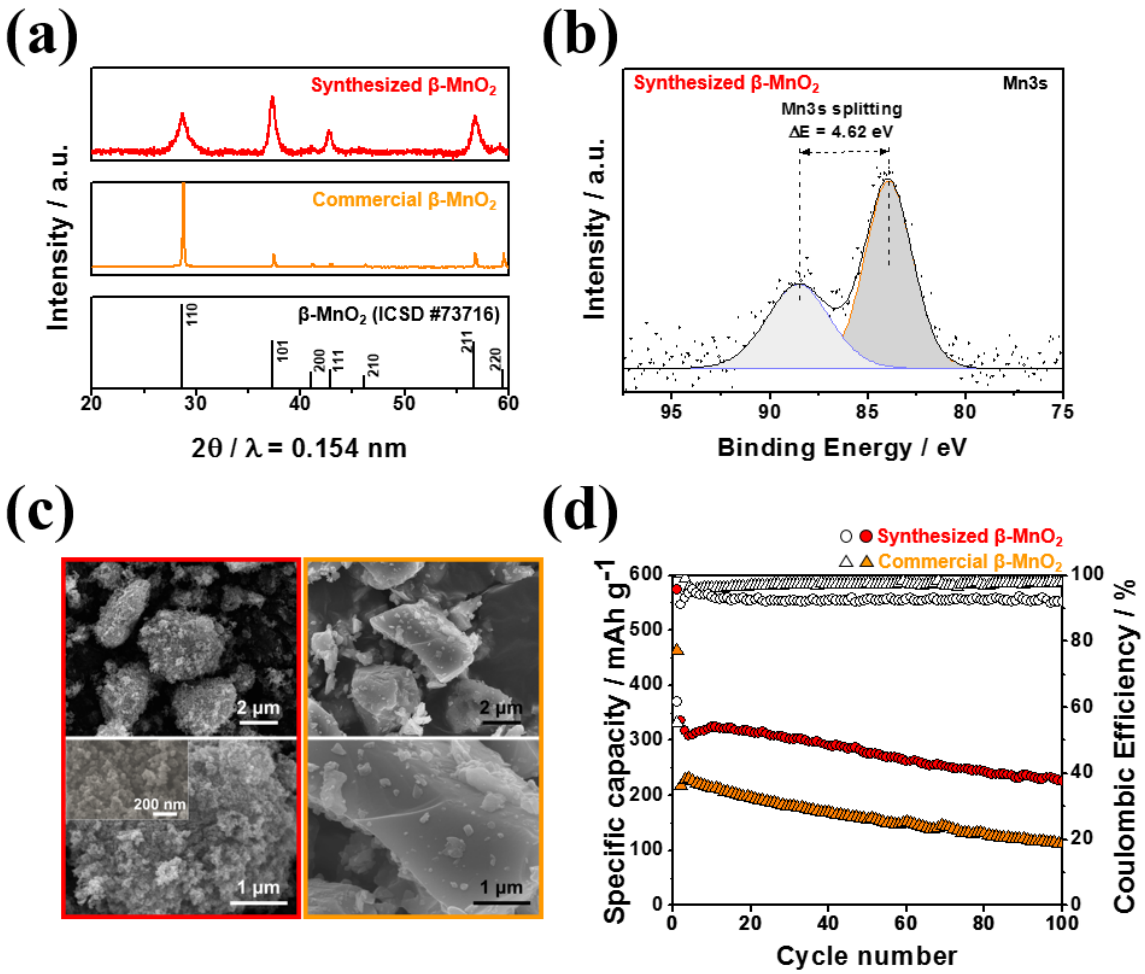

Figure 4.1 (a) In-house XRD patterns for synthesized and commercial β-MnO_2 (Alfa Aesar); (b) Mn 3s splitting in the XPS result of synthesized β-MnO_2; (c) SEM images for synthesized (red box) and commercial β-MnO_2 (orange box); (d) Cyclic performance for synthesized β-MnO_2 and commercial β-MnO_2 at C/10 current rate for the first cycle and C/5 for the following cycles

The peak broadenings are observed in synthesized β-MnO_2, however, the peak positions match the reference β-MnO_2 (ICSD #73716). The X-ray photoelectron spectroscopy (XPS) result

confirms Mn 3s multiplet splitting with ΔE = 4.62 eV in figure 4.1(b); this value agrees well with ΔE = 4.65 eV found in commercial β-MnO_2 (Alfa aesar) as shown in figure 4.2.[90]

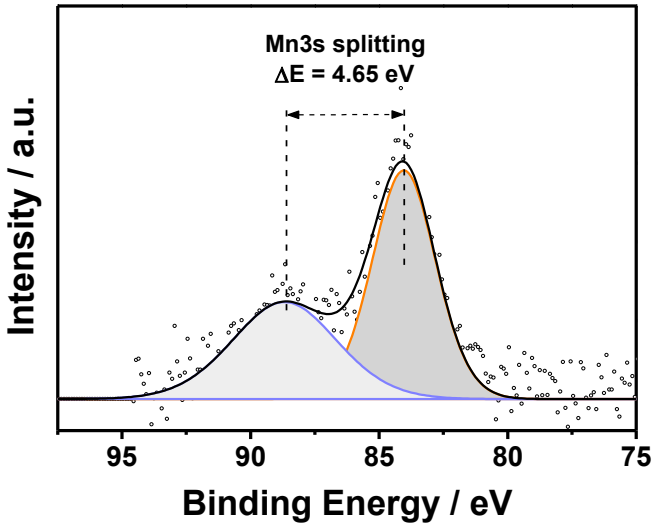

Figure 4.2 Mn 3s splitting in the XPS result of commercial β-MnO_2 (Alfa aesar)

The scanning electron microscope (SEM) image shows agglomerated secondary particles from the synthesized β-MnO_2 (the red color box) and chunky particles with small parasites from the commercial one (the orange color box) in figure 4.1(c). The primary particle has the size range of less than 50 nm in the synthesized β-MnO_2. The BET (Brunauer–Emmett–Teller) surface analysis conducted by the nitrogen sorption isotherms at -196 °C by Autosorb - iQ (Quantachrome) indicates ~21 times larger surface area for the synthesized β-MnO_2 than the commercial β-MnO_2 in Table 4.1.

Table 4.1 BET surface area for synthesized and commercial β-MnO_2

	Synthesized β-MnO_2	Commercial β-MnO_2
BET surface area / m^2 g^{-1}	52.92	2.57

The cyclic performance of Zn/β-MnO_2 alkaline batteries is tested in 3 M LiOH and 1 M KOH containing electrolyte as shown in figure 4.1(d). The first discharge capacity of synthesized β-MnO_2 is 574 mAh g^{-1} which is about 93% of the MnO_2's theoretical capacity of 616 mAh g^{-1}. On

the other hand, the commercial β-MnO_2 produces 464 mAh g^{-1} at the first discharge, which is only about 75% of the theoretical capacity. The average discharge capacity of synthesized β-MnO_2 shows 280 mAh g^{-1} over 100 cycles, which is higher than that of commercial β-MnO_2, 164 mAh g^{-1}. The coulombic efficiency defined by the percentage of charge capacity over discharge capacity is less than 100 %. This is due to the additional capacity produced by H_2 and O_2 gases, which are generated within the battery's operating voltage (figure 4.3). We estimate the amount of gas generation is different during the anodic and cathodic reaction of an electrolyte, which affects the overall coulombic efficiency of a battery. The gases are released from the customized beaker cell and its configuration is demonstrated in the experimental.

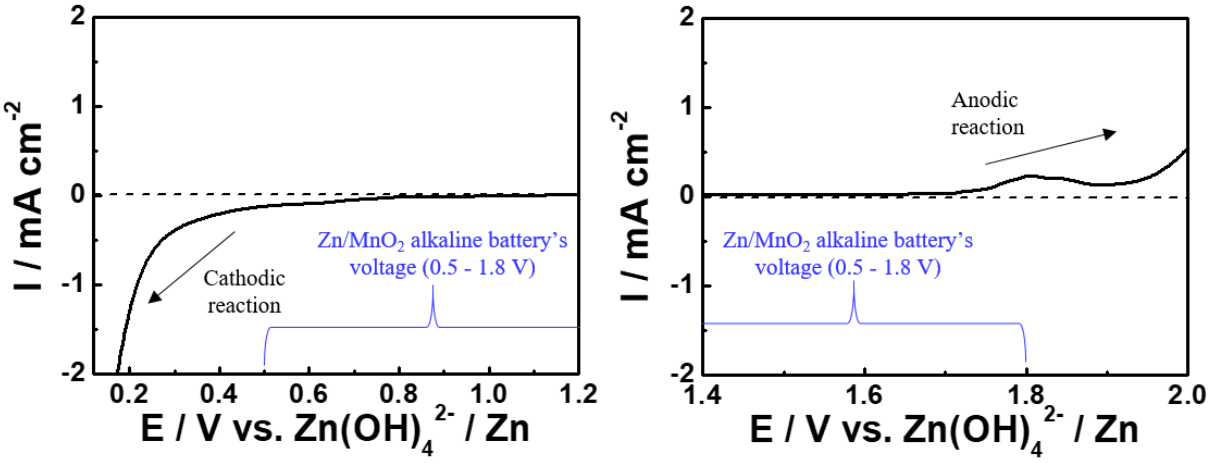

Figure 4.3 The electrochemical stability window of 1M KOH and 3M LiOH electrolytes on Ni foam electrodes

The gap between the first discharge capacities from two batteries is most likely due to the particle size of active materials. The nanoscale β-MnO_2 particles have broader electrochemical surface area than the bulk β-MnO_2 particles, which increases the effective contact points with the electrolyte, leading to low internal resistance and short diffusion pathways.[77, 88] In addition, insufficiently coordinated surface atoms of the synthesized β-MnO_2 nanoparticle are expected to

facilitate chemical adsorptions from aqueous solutions and undergo electrochemical reactions. Han et al. reported the effect of the nanosized particle on an adsorption energy of chemicals in aqueous media.[91] It shows that the adsorption energy of chemicals on the surface of a nanoparticle is stronger than that on the surface of a bulk material. A nanoparticle holds the high ratio of undercoordinated surface atoms to coordinated atoms, thus their chemisorption is greater than that of the bulk materials. Considering our nanosized β-MnO_2 case, facile electrochemical reactions are expected to undergo once H_2O adsorption from aqueous electrolytes is encouraged. The reaction mechanism of synthesized β-MnO_2 will be discussed further in this study. A cohesive energy per atom of a nanoparticle is another factor affecting the surface chemisorption.[48] Atoms in a nanoparticle are bound to each other by weak cohesive energy, which makes it energetically less stable than a bulk material. Thus, a nanoparticle in an aqueous media is likely to bind with nearby molecules to stabilize, stimulating electrochemical reactions.

4.3.2 The reaction mechanism of nanosized β-MnO_2 during the first cycle

Ex situ in-house X-ray diffraction (XRD) patterns are measured for synthesized β-MnO_2 cathodes during the first cycle of Zn/β-MnO_2 alkaline batteries (figure 4.4). The reaction mechanism of synthesized β-MnO_2 nanomaterial is proposed as follows:

Electrochemical reaction (the first discharge):

$$\beta\text{-}MnO_2 + H_2O + e^- \rightarrow \gamma\text{-}MnOOH + OH^- \quad (1)$$

$$\gamma\text{-}MnOOH + H_2O + e^- \rightarrow Mn(OH)_2 + OH^- \quad (2)$$

Electrochemical reaction (the first charge):

$$Mn(OH)_2 + 2OH^- \rightarrow \lambda\text{-}MnO_2 + 2H_2O + 2e^- \quad (3)$$

$$1/3Mn_3O_4 + 4/3OH^- \rightarrow \lambda\text{-}MnO_2 + 2/3H_2O + 4/3e^- \quad (4)$$

Chemical reaction:

$$\gamma\text{-MnOOH} + 1/2\text{Mn(OH)}_2 \rightarrow 1/2\text{Mn}_3\text{O}_4 + \text{H}_2\text{O} \qquad (5)$$

To further validate the reaction mechanism characterized by *ex situ* in-house XRD patterns, the theoretical reaction voltage (E) for each electrochemical reaction proposed in Eq. (1-4) is calculated by applying the Nernst equation as follows:

$$E = E° + 2.303 \cdot \frac{RT}{F} \cdot pOH - (-1.119) \quad V \quad vs. \quad Zn(OH)_4^{2-} \mid Zn \qquad (6)$$

where E° is the standard reduction potential (table 4.2) which is obtained by the standard Gibbs free energy of formation (table 4.3); R is the gas constant (8.314 J K^{-1} mol^{-1}); T is the room temperature (298.15 K); F is the Faraday constant (96.485 kJ mol^{-1}); pOH is the potential of hydroxide.

Table 4.2 Standard reduction potentials

	$\beta\text{-MnO}_2$ / $\gamma\text{-MnOOH}$, OH^-	$\gamma\text{-MnOOH}$ / $Mn(OH)_2$, OH^-	$Mn(OH)_2$, OH^- / $\lambda\text{-MnO}_2$	Mn_3O_4, OH^- / $\lambda\text{-MnO}_2$
E° (V vs. SHE)	0.12	-0.23	-0.05	0.11

Table 4.3 Standard Gibbs free energy of formation

	$\beta\text{-MnO}_2$ (s)	$\gamma\text{-MnOOH}$ (s)	$Mn(OH)_2$ (s)	Mn_3O_4 (s)	$\lambda\text{-MnO}_2$ (s)	H_2O (l)	OH^- (i)
$G_f°$ (kJ)	-466.41[92]	-557.73[93]	-615.00[94]	-1283.2[94]	-464.67	-237.13[94]	-157.24[94]

The theoretical value of pOH = -0.6 or pH = 14.6 is used since the electrolyte consists of 3 M LiOH and 1 M KOH, where 4 M OH^- exists in total. The Zn anode has a redox couple with $Zn(OH)_4^{2-}$ in alkaline media,[14, 95] thus we measure E with respect to the standard reduction potential of $Zn(OH)_4^{2-} \mid Zn$ (1.119 V vs. SHE).[96] The ideal voltage curve of a Zn/$\beta\text{-MnO}_2$ aqueous battery fabricated with synthesized $\beta\text{-MnO}_2$ nanomaterial is presented in figure 4.4(b). The

theoretical voltage profile (dotted line) matches well with the experimental voltage profile, which will be discussed in detail.

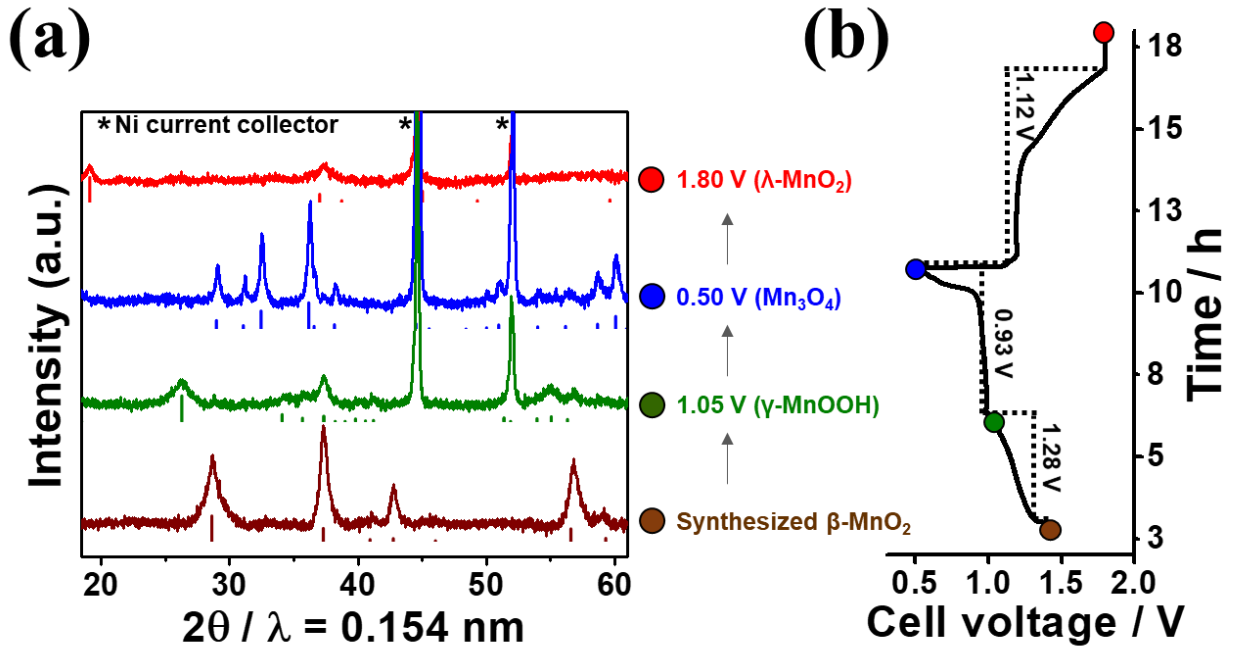

Figure 4.4 (a) *Ex situ* in-house XRD patterns for synthesized β-MnO_2 nanomaterial and its intermediate phases during the first cycle. The vertical line presents XRD patterns from ICSD database (β-MnO_2: #73716, γ-MnOOH: #84949, Mn_3O_4: #643199, and λ-MnO_2: #193445). Detailed XRD patterns are shown in figure 4.4. (b) The voltage profile for the first discharge/charge of a Zn/β-MnO_2 alkaline battery at C/10 current rate. The colored circles represent points that synthesized β-MnO_2 nanomaterial and cycled β-MnO_2 cathode samples are collected. The dotted line indicates the theoretical voltage profile at pH=14.6

As mentioned above, XRD results indicate that synthesized powder is β-MnO_2 in figure 4.4(a). This material belongs to the tetragonal crystal lattice where Mn-O octahedrons are connected in a corner-sharing and an edge-sharing manners as shown in figure 4.6. Void tunnels and Mn-O octahedrons are positioned 1 x 1. Upon the initiation of the first discharge, protons from H_2O molecules adsorbed on the surface of nanosized β-MnO_2 intercalate into the void tunnels and form γ-MnOOH at the end of the first-electron reaction (Eq. (1)). The XRD pattern of γ-MnOOH is obtained at 1.05 V (figure 4.4). γ-MnOOH has the monoclinic crystal lattice where the original

1 x 1 void tunnels in β-MnO_2 are occupied with protons as shown in figure 4.6. It is noted that the tetragonal crystal lattice of β-MnO_2 is maintained at an early stage of proton intercalation. The XRD result at 1.25 V during the first discharge shows the overall peak intensity of β-MnO_2 decreasing, yet the phase still holds the tetragonal crystal lattice (figure 4.6).

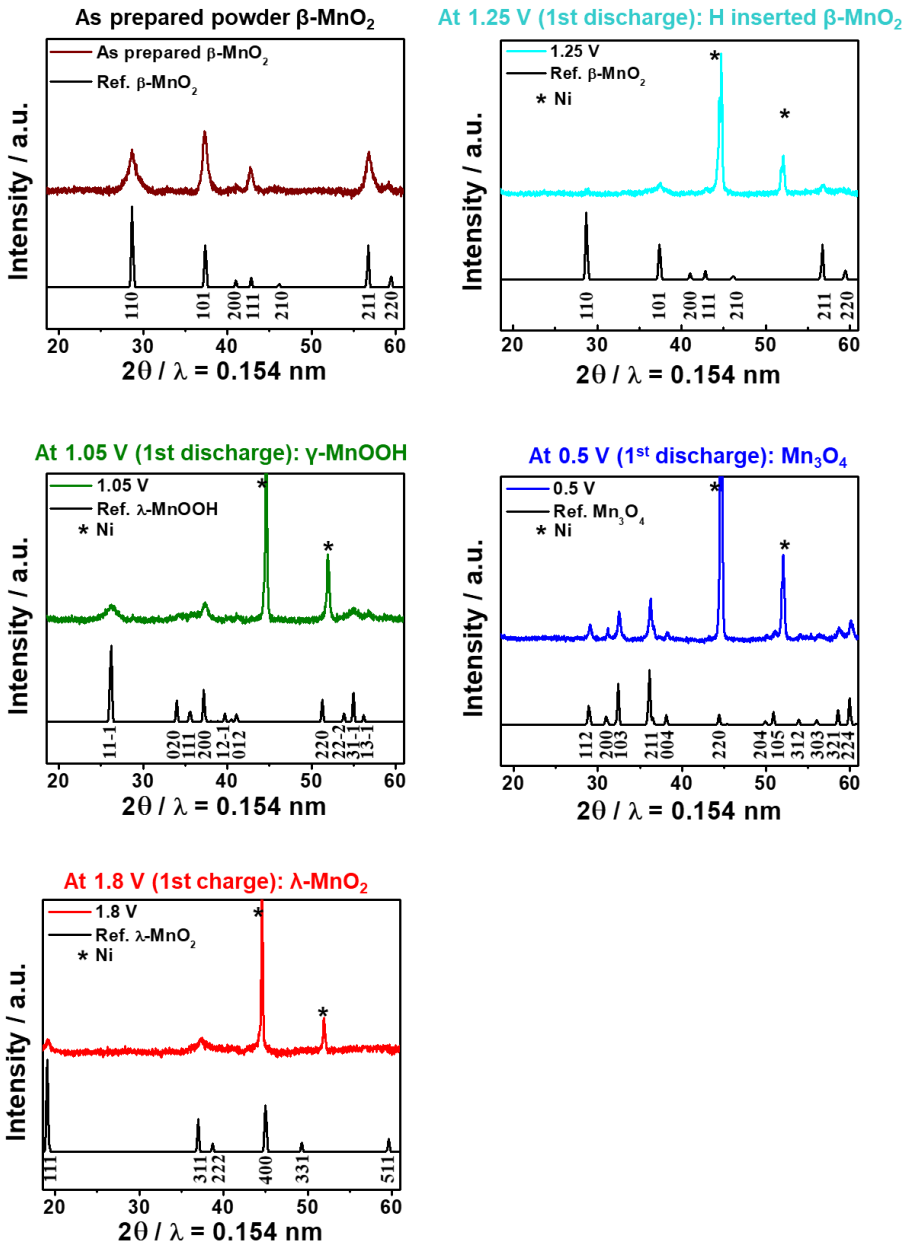

Figure 4.5 *Ex-situ* in-house XRD patterns for synthesized β-MnO_2 nanomaterial and its intermediates during the first cycle

The crystal lattice gets distorted as the proton concentration increases and becomes monoclinic at the end of the first-electron reaction at 1.05 V (figure 4.4(a)). Kordesch et al. proposed that the first-electron reaction of MnO_2 in a Zn/MnO_2 alkaline battery is a solid-solution intercalation reaction.[97] This reaction is a homogeneous step because Mn-O bonding in the host MnO_2 does not break and form a new bonding while the proton is intercalating. The theoretical voltage for β-MnO_2 | γ-MnOOH redox couple shows the average voltage of 1.28 V upon the proton intercalation, which locates within the experimental voltage curve of the first-electron reaction (figure 4.4(b)).

During the second-electron reaction, γ-MnOOH is reduced to $Mn(OH)_2$ by a two-phase conversion reaction (Eq. (2))[98-99] and Mn_3O_4 is formed by a sluggish chemical reaction in parallel (Eq. (5)).[14, 81, 99] $Mn(OH)_2$ has the trigonal crystal lattice where the layer of edge-sharing M-O octahedrons and the layer of the proton are aligned along the c-axis as shown in figure 4.6. Mn_3O_4 has the tetrahedral crystal lattice where corner-sharing Mn-O tetrahedrons and edge-sharing Mn-O octahedrons are interconnected (figure 4.6).

It is noted that the XRD result shows Mn_3O_4 solely at the end of discharge (0.5 V) in figure 4.4(a). However, the first discharge is a two-electron reaction as its experimental capacity is 574 mAh g^{-1} so in reality Mn^{4+} in β-MnO_2 reduces to Mn^{2+} in $Mn(OH)_2$.[98-99] Mn_3O_4 cannot be transformed from γ-MnOOH by an electrochemical reduction since Mn_3O_4 has two Mn^{3+} and one Mn^{2+}. If this reaction happens, only 1/3 electron is involved, which is insufficient to demonstrate the first-discharge capacity. The reduction of γ-MnOOH to $Mn(OH)_2$ is the second-electron reaction as it involves one electron.

It has been reported that Mn_3O_4 is formed by the sluggish chemical reaction between γ-

MnOOH and $Mn(OH)_2$ while the β-MnO_2 reduces to $Mn(OH)_2$ electrochemically.[14, 81, 99] We think that further chemical reaction in our battery contributes to not detecting $Mn(OH)_2$ but detecting Mn_3O_4 from the cathode sample. We collected the cathode sample by *ex situ* method to measure XRD. Additional Mn_3O_4 begins to form when the electrochemical test stopped at 0.5 V and its amount increases extensively until the *ex situ* sample is collected. Holton et al. showed the formation of Mn_3O_4 is a slow reaction.[81, 98] They measured Mn_3O_4 when experiments were tested over the extended time duration. Hertzberg et al., however, did not detect the Mn_3O_4 but $Mn(OH)_2$ while conducting *in situ* X-ray diffractometer.[85] Mn_3O_4 formation is alleviated in the relatively short-time frame. In addition, the theoretical voltage of γ-MnOOH | $Mn(OH)_2$ redox couple demonstrates the formation of $Mn(OH)_2$ during the second-electron reaction. The voltage is 0.93 V, which corresponds well with the experimental voltage plateau during the second-electron reaction (figure 4.4(b)).

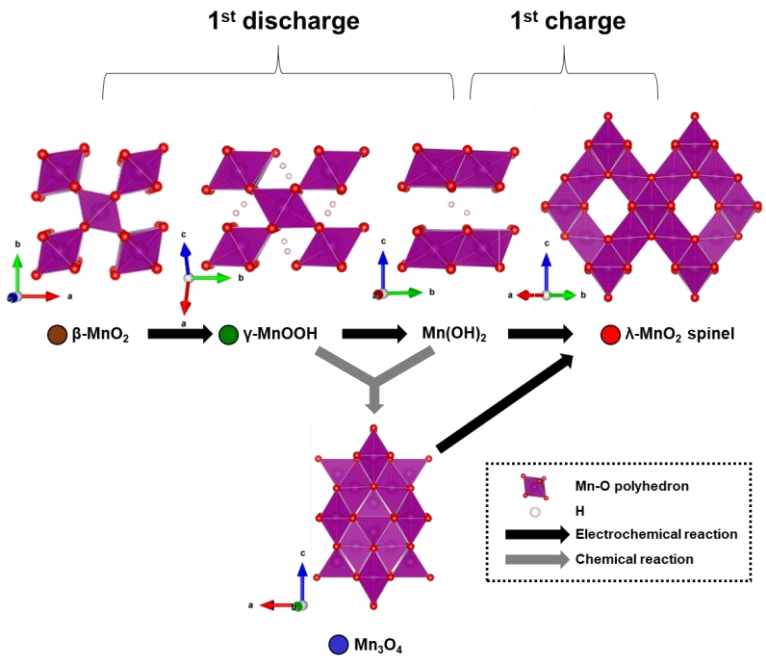

Figure 4.6 Schematic illustration of the electrochemical reaction mechanism of nanosized β-MnO_2 during the first cycle

At the end of the first charge, λ-MnO_2 is measured (figure 4.4(a)) as a result of $Mn(OH)_2$ oxidation (Eq. (3)). λ-MnO_2 is a spinel phase with the cubic crystal lattice where M-O octahedrons are interconnected in an edge-sharing manner with a 3D network of 1 x 1 void channel (figure 4.6). The XRD pattern at 1.80 V has weak and broadened peaks because of the amorphous-like nanoscale phase as shown in figure 4.4(a). Nonetheless, this phase belongs to λ-MnO_2. Among XRD patterns of MnO_2 polymorphs (figure 4.6), λ-MnO_2 has a peak at ~19.1° which corresponds to a peak in XRD pattern measured at 1.80 V (figure 4.4(a)).

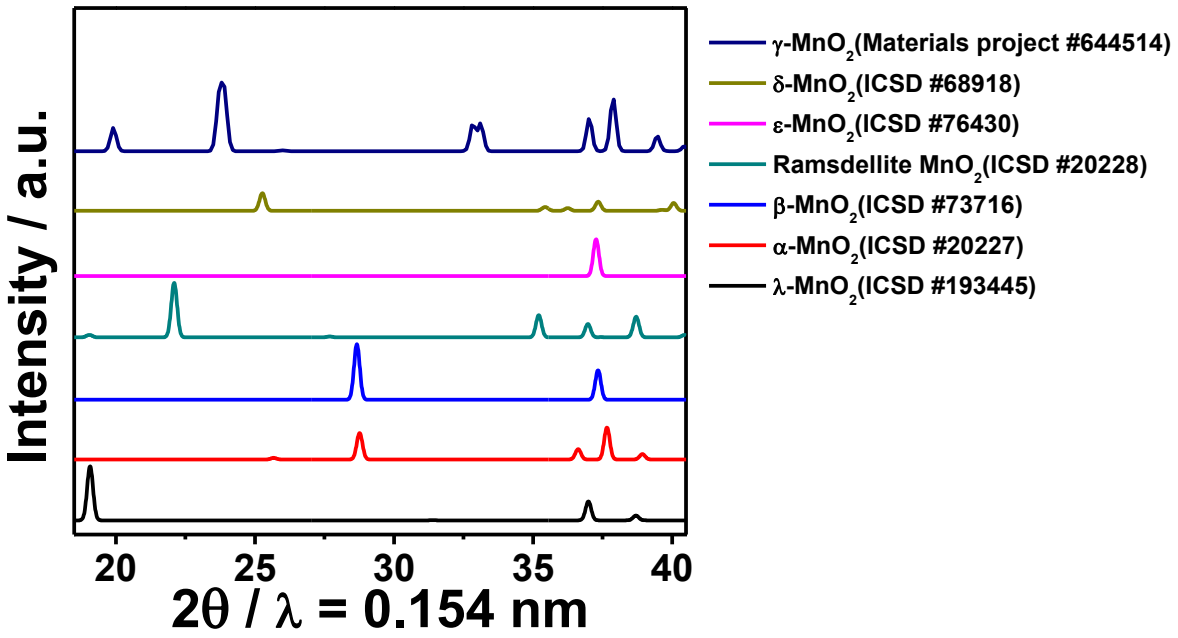

Figure 4.7 XRD patterns of MnO_2 polymorphs from ICSD database

The theoretical voltage of $Mn(OH)_2$ | λ-MnO_2 redox couple (1.12 V) supports the formation of λ-MnO_2, which is closed to the experimental voltage plateau during the first charge shown in figure 4.4(b). It is noted that the first charge capacity is 353 mAh g^{-1}, which is 57 % of the theoretical capacity for two-electron reaction. We ascribe the capacity loss to any unreacted $Mn(OH)_2$ which dissolves in the electrolyte as OH^- coordinated-complex ions or $[Mn(OH)_{n+2}]^{n-}$,[100] because Mn^{2+} in $Mn(OH)_2$ is soluble in highly concentrated basic solution.

It is interesting that Mn_3O_4 generated during the discharge is not measured at 1.80 V because it is also oxidized to λ-MnO_2 (Eq. (4)). Mn_3O_4 has poor electrical conductivity (10^8 ohm·cm)[14] which hinders electrochemical reactions in Zn/MnO_2 alkaline batteries. However, Mn_3O_4 converts into λ-MnO_2 in this study and we attribute it to the particle size of Mn_3O_4. We think that our synthesized active materials remain as nanoscale particles during phase transformations, which compensates for the intrinsic high resistivity of Mn_3O_4 and facilitates electrochemical reactions. Compared to bulky Mn_3O_4, nanoscale Mn_3O_4 has advantages in terms of large electrode/electrolyte interface for electrochemical reactions, superior conductivity by embedding into carbon network, and short electron/ion transport distance.[101] Recently, nano-size Mn_3O_4 has been reported on its high reversible capacity and enhanced coulombic efficiency as an anode material in Li-ion battery.[101-103] The theoretical redox potential of Mn_3O_4 | λ-MnO_2 is calculated as 1.28 V, which is also closed to the experimental voltage plateau during the charge (figure 4.4(b)).

4.3.3 The reaction mechanism at the hundredth cycle

The *ex situ* synchrotron X-ray diffraction (SXRD) pattern is measured at the hundredth discharged/charged state of the synthesized β-MnO_2 cathode in Zn/β-MnO_2 alkaline battery. Li and H co-inserted λ-MnO_2 spinel is formed at the hundredth discharged state as shown in figure 4.8(a). 111 and 311 peaks from the Li and H co-inserted λ-MnO_2 spinel are aligned with the peaks from *ex situ* SXRD. The presence of Li is confirmed at the hundredth discharge state by the Li signal in Li 1s region of XPS result as shown in figure 4.8(b), which supports the formation of Li contained phase. We investigate other lithiated λ-MnO_2 spinel phases to see if their XRD patterns match the *ex situ* SXRD pattern. However, none of them has any good match as shown in figure 4.8.

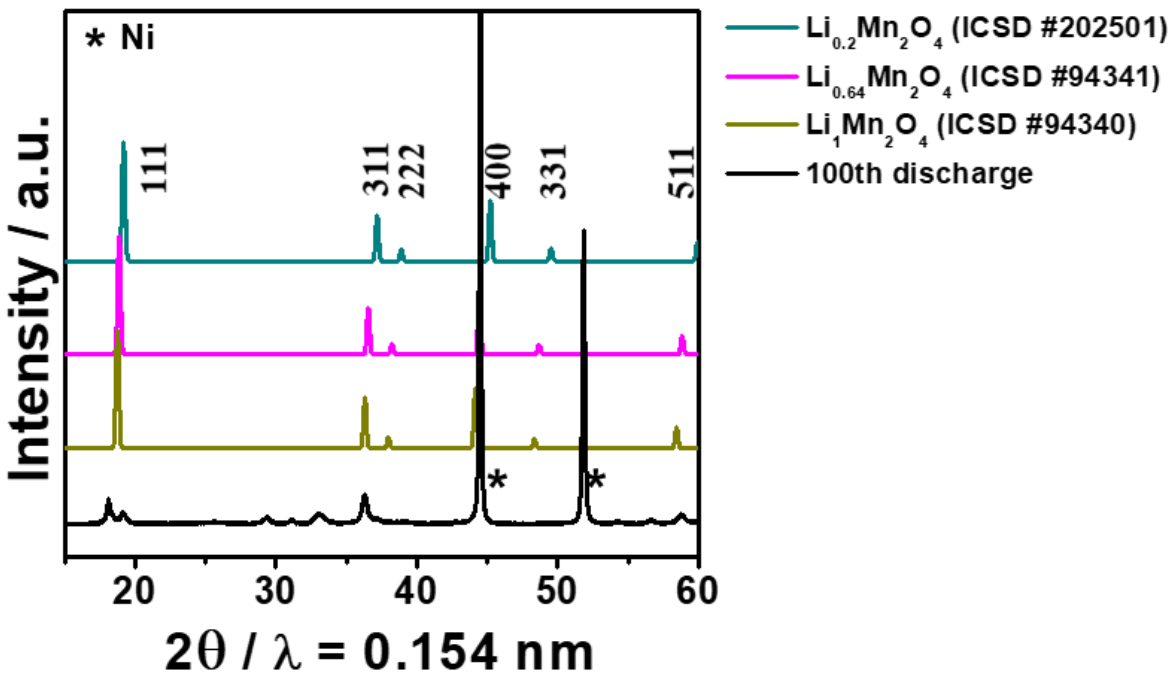

Figure 4.8 XRD patterns of lithiated Mn oxide spinels from ICSD database and the SXRD pattern at the hundredth discharge

As the lithium concentration in λ-MnO_2 spinel increases, XRD peaks moves to low 2θ altogether, which does not correspond to the *ex situ* SXRD pattern. It is noted that the specific stoichiometry of the Li and H co-inserted λ-MnO_2 spinel is not defined quantitatively, however, we anticipate the Li and H co-inserted λ-MnO_2 spinel is generated based on our *ex situ* SXRD and XPS.

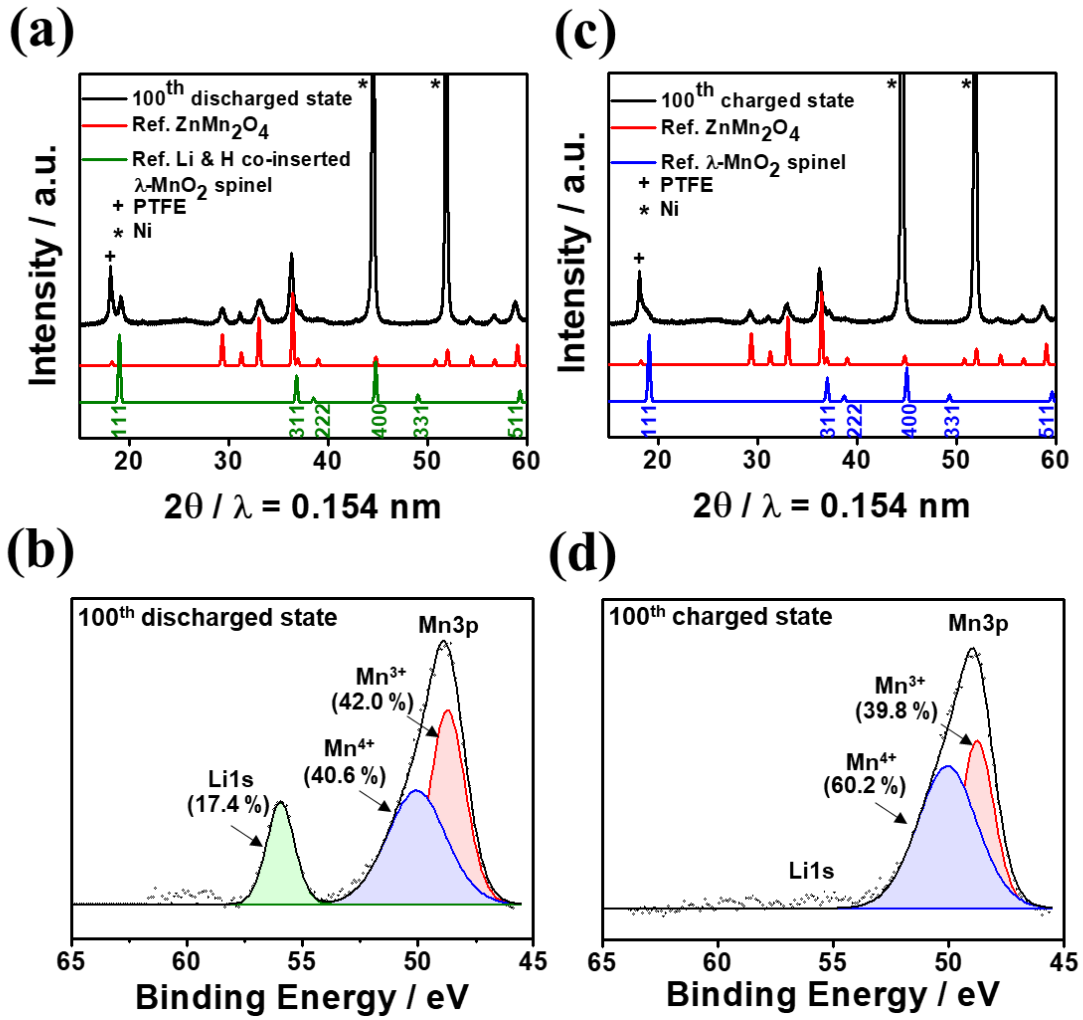

Figure 4.9 (a) *Ex situ* SXRD pattern from the cathode at the hundredth discharged state, the reference $ZnMn_2O_4$ (ICSD #15305) and the reference Li & H co-inserted λ-MnO_2 spinel (ICSD #85606); (b) XPS spectra for Li 1s and Mn 3p region; and (c) Zn 2p region from the cathode at the hundredth discharged state; (d) *Ex situ* SXRD pattern from the cathode at the hundredth charged state, the reference $ZnMn_2O_4$ (ICSD #15305) and the reference λ-MnO_2 spinel (ICSD #193445)

We estimate delithiated λ-MnO_2 spinel is formed at the hundredth charged state as shown in figure 4.9(c). 111 and 311 peaks from delithiated λ-MnO_2 spinel are aligned with peaks from measured *ex situ* SXRD pattern. We believe this phase is formed by the extraction of Li and H process during charging as shown in figure 4.10. Li 1s region from XPS result has not detected Li, supporting the formation of delithiated spinel phase. In addition, an increase in the ratio of Mn^{4+}'s amount to Mn^{3+}'s indicates delithiation upon charging as shown in figure 4.9(b, d). The ratio is

about 1:1 at the hundredth discharge and it increases to 3:2 at the hundredth charge. Mn^{3+} is partially oxidized to Mn^{4+} when Li^{+} leaves the cathode.

We measure irreversible $ZnMn_2O_4$ from both the hundredth discharge/charge states in the *ex situ* SXRD pattern (figure 4.9(a, c)). In Zn/MnO_2 alkaline batteries, $Zn(OH)_4^{2-}$ is formed during the anode discharge reaction:[95]

$$Zn + 4OH^- \rightarrow Zn(OH)_4^{2-} + 2e^- \qquad (7)$$

Once $Zn(OH)_4^{2-}$ is formed, it reacts to MnOOH in a cathode electrode chemically:[104]

$$2MnOOH + Zn(OH)_4^{2-} \rightarrow ZnMn_2O_4 + 2H_2O + 2OH^- \qquad (8)$$

$ZnMn_2O_4$ has the tetrahedral crystal lattice where corner-sharing Zn-O tetrahedrons and edge-sharing Mn-O octahedrons are interconnected (figure 4.10).

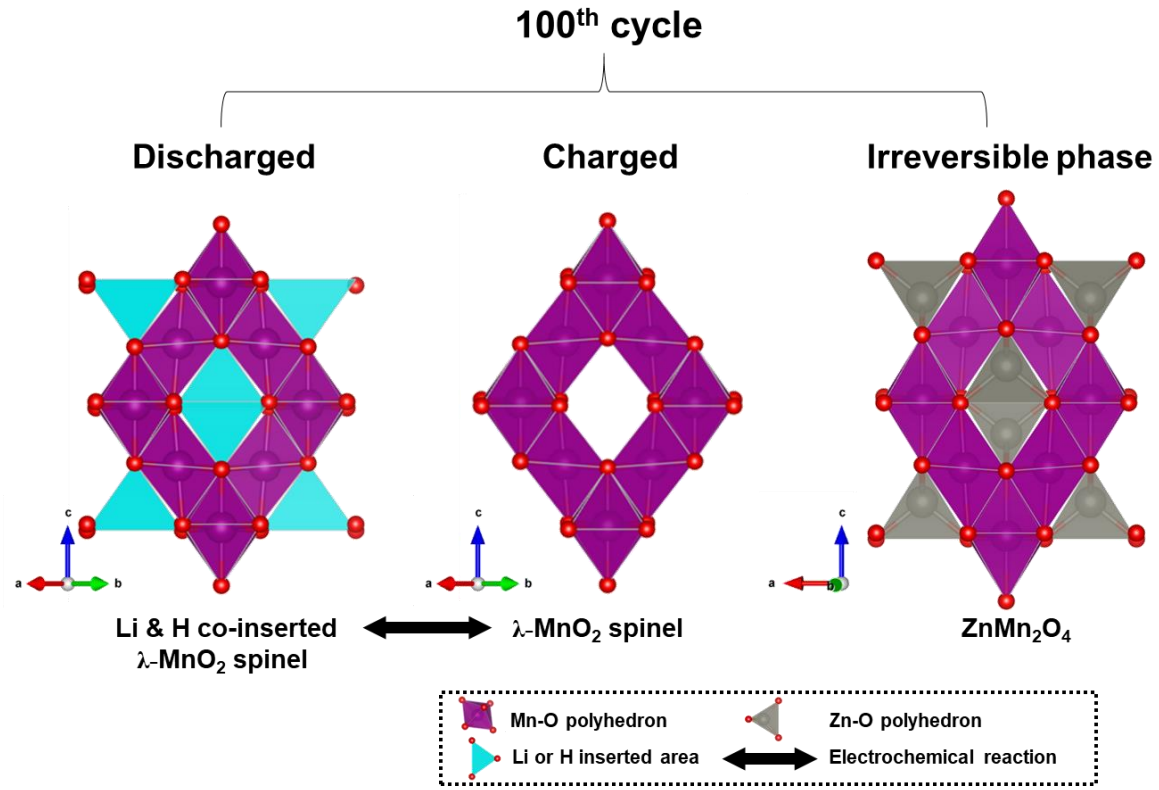

Figure 4.10 The reaction mechanism of β-MnO_2 during the hundredth cycle

Mn and Zn have 3+ and 2+ oxidation states, respectively. $ZnMn_2O_4$ is known to have higher resistivity than MnO_2 in six orders of magnitude, which causes a loss of conductivity in the cathode electrode.[14] In this study, $ZnMn_2O_4$ is not found in the first cycle as shown in figure 4.4(a), however, we find it at the hundredth cycle from both the discharged/charged states in figure 4.10. We expect its amount in the cathode increases as the cycle of Zn/β-MnO_2 alkaline battery proceeds, which leads to capacity fading.

4.3.4 The effect of Bi_2O_3 additive

It is reported that the adding Bi^{3+} either chemically or physically to the MnO_2 cathode improves the cycling performance of Zn/MnO_2 alkaline batteries.[105-107] Recently Shin et al. suggested that zincate ion is deposited on the Bi_2O_3 and prolongs the cycle life of Zn-based batteries.[73] As we mentioned, zincate ion undergoes a chemical reaction with Mn species in a cathode and produces $ZnMn_2O_4$, which is a highly irreversible phase in Zn/MnO_2 alkaline batteries. In order to alleviate the side effect of zincate ion, we physically mix Bi_2O_3 into the synthesized β-MnO_2 nanomaterial with 4% mole fraction and measure the performance of Zn/β-MnO_2 alkaline battery. It is noted that the average discharge capacity is 369 mAh g^{-1} over 100 cycles (figure 4.11(a)). This indicates increased capacity compared to the commercial β-MnO_2 and synthesized β-MnO_2 nanomaterial (164 and 280 mAh g^{-1} in average over 100 cycles, respectively). Furthermore, the synthesized β-MnO_2 nanomaterial with Bi_2O_3 shows improved rate capability as shown in figure 4.11(b). This exhibits higher discharge capacity and better cycling stability than the synthesized β-MnO_2 without Bi_2O_3. To be specific, the synthesized β-MnO_2 with Bi_2O_3 has the average capacity of 506 mAh g^{-1} at the first stage and retain 86% of 506 mAh g^{-1} (434 mAh g^{-1}) at the last stage. However, the synthesized β-MnO_2 without Bi_2O_3 has the average capacity of 403 mAh g^{-1} at the first stage and 292 mAh g^{-1} at the last stage, which indicates 72% is recovered. In

order to investigate the role of Bi_2O_3 in the rechargeable Zn/MnO_2 alkaline chemistry, Bi_2O_3 powder was immersed in the 6 M Zn nitrate solution. SEM images show that original disordered structures transform to relatively ordered structures with island meshes in a Zn^{2+} solution (figure 4.12). The energy dispersive X-ray spectroscopy (EDS) mapping for immersed Bi_2O_3 powder that was carefully cleansed and dried indicates the presence of Zn species on the surface of the Bi_2O_3 (figure 4.13). These SEM and EDS analyses imply that Zn^{2+} reacts with the surface Bi_2O_3. As was discussed for Zn/MnO_2 alkaline batteries, $Zn(OH)_4^{2-}$ or potentially a combination of Zn^{2+} and OH^- in alkaline solution undergo chemical reactions with Mn species to produce an electrochemically irreversible phase consisting of $ZnMn_2O_4$. Our results suggest that the formation of $ZnMn_2O_4$ can be alleviated through $Zn(OH)_4^{2-}$ reactions with Bi_2O_3 which lessens the likelihood that Mn species will react with $Zn(OH)_4^{2-}$.

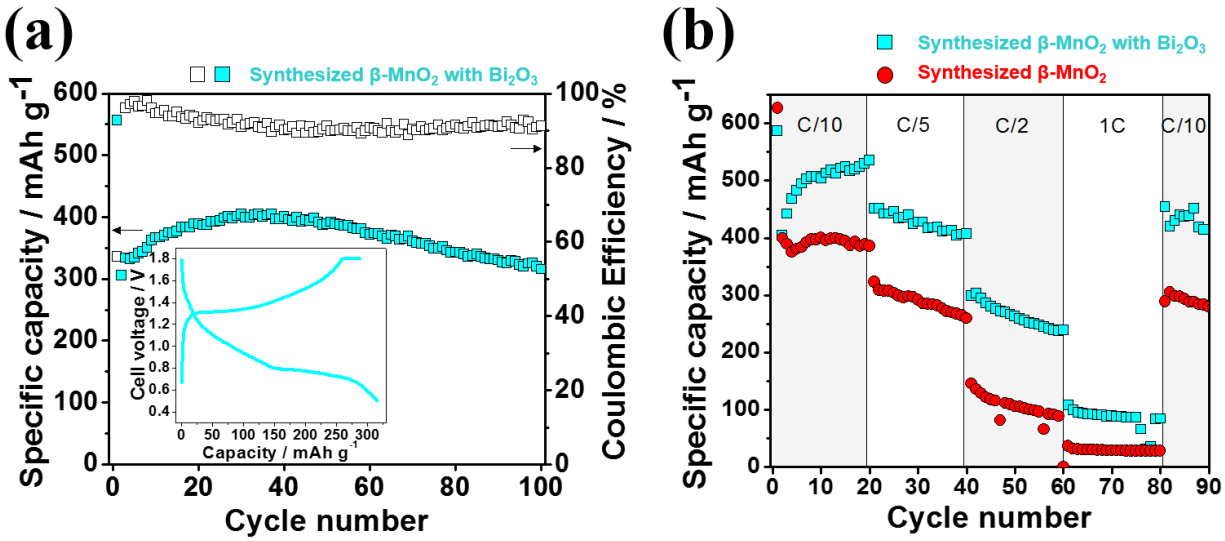

Figure 4.11 (a) Cyclic performance for the synthesized β-MnO_2 with Bi_2O_3 additive. The inset indicates the voltage curve at the hundredth cycle; (b) Rate capability test for the synthesized β-MnO_2 with and without the Bi_2O_3 additive are conducted with C/10, C/5, C/2, 1C, and C/10 in sequence

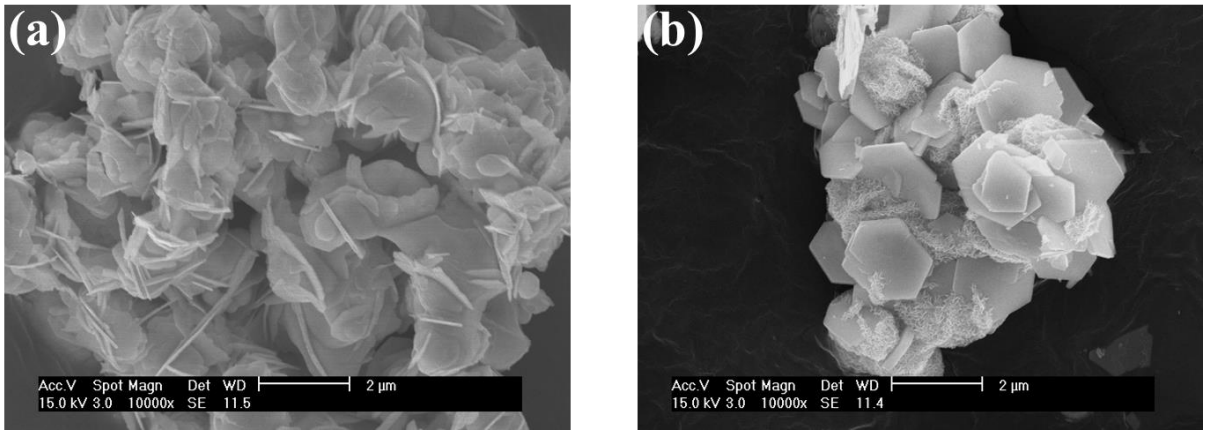

Figure 4.12 SEM images of (a) Bi_2O_3 powder and (b) immersed Bi_2O_3 powder in 6M Zn nitrate solution

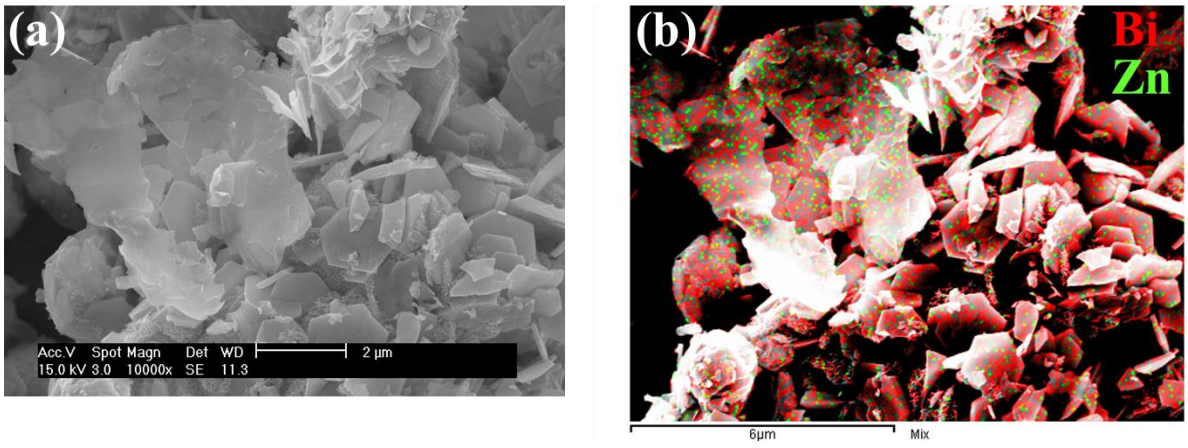

Figure 4.13 (a) SEM image of immersed Bi_2O_3 powder in 6M Zn nitrate solution and (b) corresponding EDS mapping for Zn $K\alpha_1$ and Bi $M\alpha_1$

4.4 Conclusions

This study has demonstrated that synthesized β-MnO_2 nanomaterials have high utility for rechargeable Zn/β-MnO_2 alkaline batteries. The nanosized β-MnO_2 cathode in the 1 M KOH and 3 M LiOH mixed electrolyte shows higher rechargeable capacity compared to the bulky β-MnO_2 cathode's capacity. The β-MnO_2 nanomaterials have large surface area and strong surface-

chemisorption property to facilitate electrochemical reactions in alkaline solutions. In addition, the phase transformation of synthesized β-MnO_2 nanomaterial involves proton intercalation reactions followed by two-phase conversion reactions during the first cycle. At the hundredth cycle, Li and H intercalate together into the host structure of λ-MnO_2 spinel. Additionally the physical incorporation of Bi_2O_3 into synthesized β-MnO_2 nanomaterials shows an excellent average discharge capacity of 369 mAh g^{-1} over 100 cycles. The findings of this study may provide useful insights towards the development of rechargeable Zn/MnO_2 alkaline batteries in high-energy and low-cost stationary energy storage.

Chapter 4, in full, is currently being prepared for submission for publication of the material. Joon Kyo Seo, Jaewook Shin, Hyeseung Chung, Po Yu Meng, Xuefeng Wang, Y. Shirley Meng. The dissertation author was the primary investigator and author of this material.

Chapter 5: First principles studies on electrode materials for Li-ion batteries and electrolyzers

5.1 Introduction

In this chapter, first principles calculations are conducted extensively for $Li_4Ti_5O_{12}$ as an anode material and $LiNi_{0.5}Mn_{1.5}O_4$ spinel as a cathode material in Li-ion batteries, and $YBaCo_4O_7$ as a catalyst for OER in water electrolyzers.

$Li_4Ti_5O_{12}$ exhibits relatively low capacity and high voltage compared to the most commercially available Li-ion anode, graphite (175 vs 372 mAh·g−1 and 1.55 vs ∼0.1 V Li/Li^+).[108] The high redox potential of $Li_4Ti_5O_{12}$ lies in the electrolyte stability window.[109] This enables cycling without forming deleterious passivation layers, which is a problem for long-term stability of conventional graphite anode and popular alternatives such as silicon.[110] The two-phase reaction, which leads to moderate capacity, is also highly facile. It proceeds between two members ($Li_4Ti_5O_{12}$ and $Li_7Ti_5O_{12}$) that possess the same crystallographic space group: Fd-3m. Even upon intercalation of 3 Li^+ per formula unit, there is only a 0.2% volume change of the spinel lattice.[15] The stability, robustness, and safety of $Li_4Ti_5O_{12}$ have enabled successful commercialization.[111] While the ionic conductivity of $Li_4Ti_5O_{12}$ is comparable to that of other Li-ion anodes, a major shortcoming is its inherently low electronic conductivity.[112-115] $Li_4Ti_5O_{12}$ is considered to be an insulator with experimentally reported band gaps normally between 3.0 and 4.0 eV.[116-117] To circumvent this problem, we *ab-initio* investigate the effect of Gd doping upon the enhanced electrochemical performance of $Li_4Ti_5O_{12}$. Although it is a common dopant used in electrochemical systems and has been shown to significantly improve the rate capability of LIB cathode materials [118], full details of the effects of Gd-doping in spinel $Li_4Ti_5O_{12}$ anode materials

have not been reported until now. Ground state Gd has a special electronic structure of a half full 4f electron shell, thus we expect that doping Gd^{3+} ion is beneficial to enhance the rate performance of $Li_4Ti_5O_{12}$. We demonstrate the results and explain the beneficial characteristics of doping Gd^{3+} into $Li_4Ti_5O_{12}$. In addition, understanding exactly how the two-phase transformation between $Li_4Ti_5O_{12}$ and $Li_7Ti_5O_{12}$ proceeds and which of the factors that promote the two-phase transformation is still relatively ill-defined because few diffraction techniques are able to physically differentiate them.[119-120] We perform DFT calculations to fully describe the two-phase reaction and structures formed. The band gaps of $Li_4Ti_5O_{12}$ and its lithiated form are calculated.

Recently, $LiNi_{0.5}Mn_{1.5}O_4$ (LNMO), which is one of derivatives of 4 V-spinel $LiMn_2O_4$ (LMO) electrode, has drawn attention for powering electric vehicles and stationary energy storage.[121-124] Substituting Mn with Ni has proven to be an effective way to enhance the electrochemical performance of LMO. Ni-doped LMO shows a high operating voltage (~4.7 V vs. Li), however the poor capacity fading still remain as a major challenge in its widespread application.[20, 125-130] In order to commercialize the LNMO material, it is important to operate LIB at fast Li insertion-extraction kinetics and high temperature. Despite the fact that the LNMO material undergoes minimal structural changes at low voltage (< 4.4 V), undesirable change of the spinel lattice often occurs at high voltage. This is one of the factors that degrades the reversible energy density of the LNMO material. Several studies have been conducted on the structural changes of bulk LNMO by advanced characterization techniques.[131-132] Based on observation, degradation mechanisms are proposed: (1) the Jahn-Teller distortion,[133-135] (2) cation mixing between Li and Mn, and (3) the dissolution of Mn^{2+} ion into the electrolyte.[136-138] These investigations provide better understanding on the degradation mechanisms in bulk, however, a detailed atomic scale changes on the surface structure of the LNMO is still needed.[122, 139] In this thesis, the first principles

calculations were carried out to understand how the surface reconstruction degrades LNMO as Mn^{2+} phase forms. Our results demonstrate that LNMO (111) undergoes the surface reconstruction to minimize the surface energy, but reconstructed Mn_3O_4 contains soluble Mn^{2+} ions, which can cause Mn dissolution into an electrolyte.

Oxygen evolution reaction (OER) is the essential step for water electrolysis. In general, the OER undergoes the complex four-electron transfer process, thus it displays large overpotential. Multiple catalysts have been developed to alleviate the overpotential and some of them show successful functionalities. For instance, the simple peroxide-type catalysts such as IrO_2 and RuO_2 have been adopted in the industrial water electrolysis.[140] Perovskite-type $Ba_{0.5}Sr_{0.5}Co_{0.8}Fe_{0.2}O_3$ (BSCF) and spinel-type $(Fe, Co, Mn)_3O_4$ have also shown high OER activity in alkaline solutions.[141-144] It is noted that an octahedral site coordinated with six oxygens has been regarded as an OER active site regardless of catalysts' crystal structures. In this study, however, we show tri-oxygen-coordinated Co on $YBaCo_4O_7$ (110) as an OER active site since it has the lowest OH adsorption energy compared to other surface Co coordinated with different numbers of oxygen. We select the OER active site, which displays strong OH adsorption energy because the OER initiates from OH adsorption. Our calculations demonstrate that the OER activity is promoted on the tri-oxygen-coordinated surface Co in $YBaCo_4O_7$ (110). In addition, we find that OH* and O* formations are energetically favorable (exothermic), whereas OOH* and O_2 formation steps are unfavorable (endothermic) at the equilibrium potential (U = 1.23 V). When the applied potential (U) is 2.24 V, all free energy steps become exothermic and all OER procedure are completed.

5.2 Experimental

In the study of Gd doping $Li_4Ti_5O_{12}$, first principles calculations were based on the spin-polarized Generalized Gradient Approximation (GGA) [40] using the Perdew-Burke-Ernzerhof (PBE) exchange-correlation implemented in Density Functional Theory (DFT) [42]. We used a plane-wave basis set and the Projector Augmented Wave (PAW) method to replace the interaction potentials of the core electrons, as parameterized in Vienna Ab initio Simulation Package (VASP) [43-44]. In all calculations, Li (2s1), Ti (3p6 3d3 4s1), O (2s2 2p4), and Gd (4f7 5s2 5p6 5d1 6s2) are treated as the valence electron configurations. A gamma point mesh with 9 x 9 x 3 k-points was specified in the Brillouin zone and periodic boundary conditions were utilized in the model systems. All the atoms were fully relaxed to simulate the optimized structure of each lattice model, with a cutoff energy of 368 eV on a plane wave basis set. The calculated lattice constant for $Li_4Ti_5O_{12}$ was 8.43 Å in this work; this value shows only a small discrepancy from the experimentally measured value of 8.35 Å, with the error of 0.96% [145].

In the study of two-phase reaction between $Li_4Ti_5O_{12}$ and $Li_7Ti_5O_{12}$, the GGA by PBE, as implemented in the VASP, was adopted to describe the exchange-correlation energy of electrons in $Li_4Ti_5O_{12}$.[40, 42, 45] The interaction potential of the core electrons was replaced with PAW pseudopotentials.[43] In all calculations, Li (1s22s1), Ti (3p6 3d3 4s1), and O (2s2 2p4) are treated as the valence electron configurations. A gamma point mesh with 6 × 6 × 2 k-points was specified in the Brillouin zone, and periodic boundary conditions were imposed on our calculations. The plane-wave energy cutoff was set at 520 eV, which is 1.3 times higher than the maximum cutoff specified by the pseudopotential of oxygen in the VASP. We set the electronic energy difference required for convergence at 10^{-4} eV. All the atoms were fully relaxed to simulate the optimized structure of each lattice model. The density of states (DOS) for structurally optimized $Li_4Ti_5O_{12}$

and $L_7Ti_5O_{12}$ were calculated using the tetrahedron method with Blöchl corrections.[146] We used the Heyd−Scuseria−Ernzerhof (HSE06) hybrid functional to produce the exact band gaps of $Li_4Ti_5O_{12}$ and $Li_7Ti_5O_{12}$.[39, 147] We also tuned 30% of the exact Hartree−Fock (HF) exchange contribution to the hybrid functional in order to benchmark the experimental band gap of $Li_4Ti_5O_{12}$.

In the study of surface degradation of LNMO, the Perdew-Burke-Ernzerhof (PBE) formulation of the generalized gradient approximation (GGA), as implemented in the Vienna Ab initio Simulation Package (VASP), was adopted to describe the exchange-correlation energy of electron in LNMO.[40, 42, 45] We used pseudopotentials generated by the Projector Augmented Wave (PAW) method to replace the interaction potentials of the core electrons.[43] The appropriate *k*-point mesh of 3 x 3 x 3 and 2 x 2 x 1 were specified for the bulk and the surface calculations of LNMO. In surface models, vacuum space is thicker than the slab thickness to prohibit interactions among the images. All the atoms were fully relaxed in the bulk calculation. In surface calculations, however, the first eight layers from the bottom have been fixed and the rest of layers were relaxed. The Dudarev's rotationally invariant DFT+*U* functional was adopted to treat the 3d electrons in Mn and Ni ions.[41] The effective *U* values are 3.9 and 6.0 eV for Mn and Ni.[46] All calculations are performed with the cutoff energy of 520 eV on a plane wave basis set. The calculated lattice parameter for LNMO was found to be 8.31 Å in this report, which shows a small discrepancy from the refined value of 8.17 Å with the error of 1.71%.

In the study of OER on $YBaCo_4O_7$, we use the Vienna Ab initio Simulation Package (VASP) with the Perdew-Burke-Ernzerhof (PBE) formulation of the generalized gradient approximation (GGA) to describe the exchange-correlation energy of electron in $YBaCo_4O_7$.[40, 42, 45] The interaction potentials of the core electrons were replaced by pseudopotentials generated by the Projector Augmented Wave (PAW) method.[43] The appropriate *k*-point mesh of 4 x 4 x 2 and 2 x 2

x 1 were specified for the bulk and the surface calculations of $YBaCo_4O_7$. In surface models, vacuum space is thicker than the slab thickness to prevent interactions among the images. All the atoms were fully relaxed in the bulk calculation. However, the first four layers from the bottom have been fixed and the rest of layers were relaxed in surface calculations. In order to treat the 3d electrons in Co ions the Dudarev's rotationally invariant DFT+*U* functional[41] was adopted with the effective $U = 3.32$.[148] We use the cutoff energy of 520 eV for all calculations on a plane wave basis set.

5.3 Results and Discussion

5.3.1 $Li_4Ti_5O_{12}$ spinel as anode material in Li-ion batteries

In order to further elucidate the electronic and structural changes of Gd-doped materials, we used DFT to calculate energetically optimized lattice models of pristine and doped $Li_4Ti_5O_{12}$. Those structures are represented in figure 5.1.

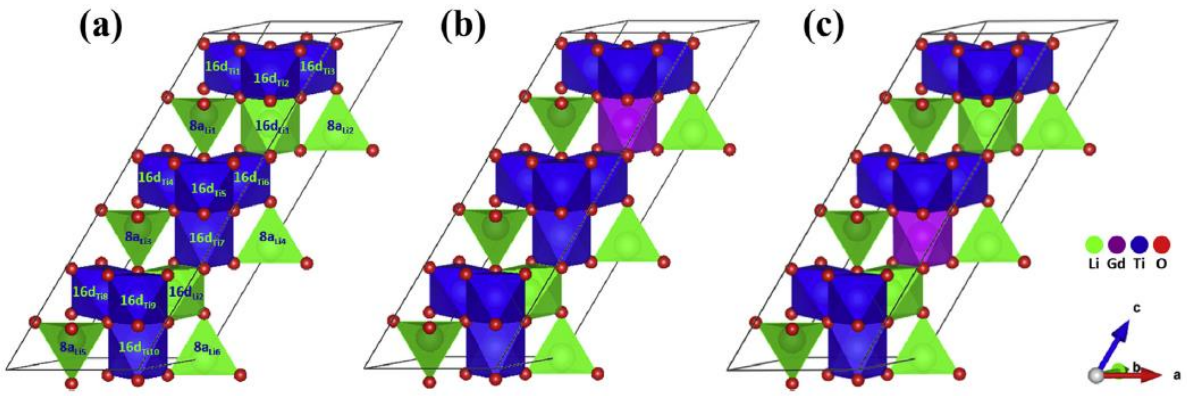

Figure 5.1 Model systems and structural optimizations of the (a) $Li_4Ti_5O_{12}$ lattice, as well as (b) Li, and (c) Ti sites, where Gd doping is most thermodynamically stable

Figure 5.1(a) shows the unit cell consists of both tetrahedral 8a and octahedral 16d sites coordinated by oxygen in 32e sites. While 8a sites are solely occupied by Li ions, octahedral 16d

sites are occupied by both Li and Ti ions with the compositional ratio of 1:5 (1 Li for every 5 Ti). The lowest energy structure, which is demonstrated in figure 5.1(a), was obtained when octahedrally coordinated Li was farthest away from one another. This was the case when Li ions in 16d sites were separated by four cation layers along the c-axis [149-150].

The range of 8a and 16d sites shown in the unit cell of figure 5.1(a) was explored as a candidate for potential Gd doping. Considering the case of Gd being doped into any of the Li ion sites, $Li_4Ti_5O_{12}$ with Gd substituted into the $16d_{Li1}$ site resulted in the lowest energy among the possible candidates. This is represented by the structure in figure 5.1(b). The other doping cases show relatively higher energy, ranging from 176 meV to 373 meV per formula unit, with respect to the most stable structure. In addition, the calculation of Gd doped into the original Ti ion sites (figure 5.1(c)) exhibits that $Li_4Ti_5O_{12}$ with Gd substituted into the $16d_{Ti7}$ site has the lowest energy. The other candidates show relatively higher energy, ranging from 93 meV to 252 meV per formula unit, with respect to the most stable structure. The energy of Gd doped into the $16d_{Ti10}$ structure is almost identical to the most stable structure (only 0.16 meV energy difference), which is due to the similarity in their atomic arrangement; both of positions share the edge with the 16d Li site. A summary of these values is provided in Table 5.1.

Table 5.1 Gibbs energy per formula unit for doping cases with respect to the energy of the most stable structure

Gd doped into the original Li ion sites		**Gd doped into the original Ti ion sites**	
Gd doping site	Relative energy (meV)	Gd doping site	Relative energy (meV)
$16d_{Li2}$	372	$16d_{Ti1}$	243
$8a_{Li1}$	280	$16d_{Ti2}$	247
$8a_{Li2}$	280	$16d_{Ti3}$	252
$8a_{Li3}$	373	$16d_{Ti4}$	244
$8a_{Li4}$	176	$16d_{Ti5}$	241
$8a_{Li5}$	176	$16d_{Ti6}$	252
$8a_{Li6}$	373	$16d_{Ti8}$	93
$16d_{Li1}$	0	$16d_{Ti9}$	93
		$16d_{Ti10}$	0.16
		$16d_{Ti7}$	0

In order to investigate the effect of Gd doping upon the enhanced electrochemical performance of $Li_4Ti_5O_{12}$, we utilize the DFT band structure calculation on $Li_4Ti_5O_{12}$, $Li_{3.5}Ti_5Gd_{0.5}O_{12}$, and $Li_4Ti_{4.5}Gd_{0.5}O_{12}$, as shown in figure 5.2(a-c), respectively.

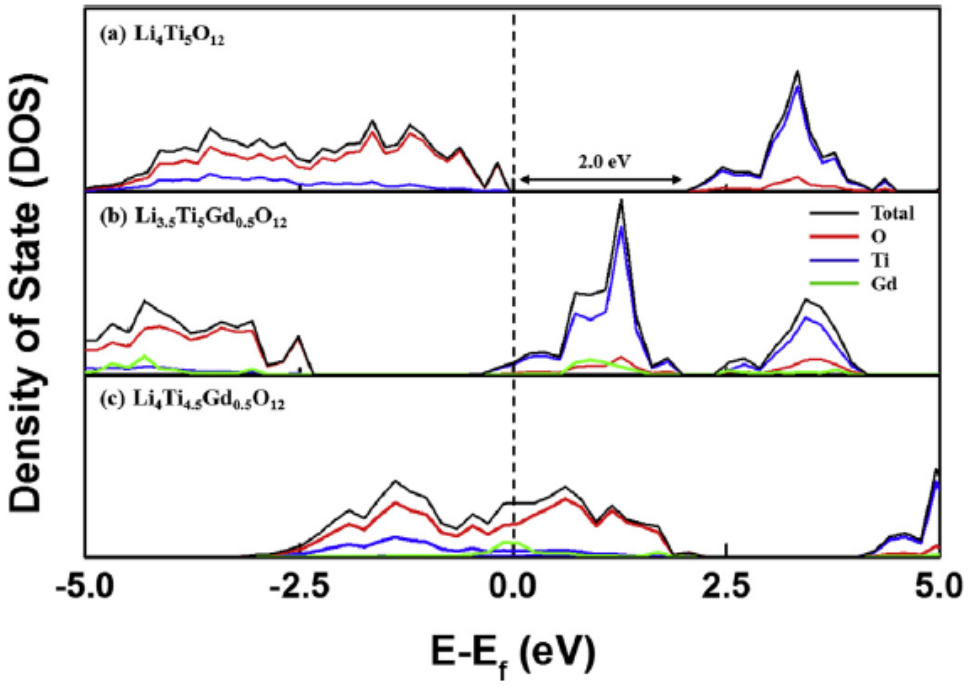

Figure 5.2 Density of states (DOS) of $Li_4Ti_5O_{12}$ and $Li_{3.5}Ti_5Gd_{0.5}O_{12}$ where Gd is doped into the $16d_{Li1}$ site, as well as $Li_4Ti_{4.5}Gd_{0.5}O_{12}$ where Gd is doped into the $16d_{Ti7}$ site; the Fermi energy is normalized to 0 eV

In figure 5.2(a), the band gap of $Li_4Ti_5O_{12}$ is about 2 eV, which is in the range of previous experimental and calculated range of 1.8-3.8 eV [117, 151-153] and 1.7 to 2.3 eV [154-156], respectively. The band gap is mainly determined by the O 2p and Ti 3d bands and $Li_4Ti_5O_{12}$ is an insulator. It is clear that there is a strong bond between Ti and O from their overlapped DOS.

Upon substituting Gd with Li, however, all the projected DOS of $Li_{3.5}Ti_5Gd_{0.5}O_{12}$ move downwards with respect to the normalized energy ($E-E_f$) and the tail of conduction bands is placed below the Fermi level, becoming partly filled as shown in figure 5.2(b). On the other hand, all the projected DOS of $Li_4Ti_{4.5}Gd_{0.5}O_{12}$ (figure 5.2(c)) shift upwards with respect to the normalized energy ($E-E_f$) and the Fermi level is located in the middle of valence bands. This suggests that only little energy is necessary for an electron to move to an energy level higher than the Fermi level. Both Gd doping cases demonstrate that Gd doped $Li_4Ti_5O_{12}$ is an electrical conductor where Gd

has an important role as a donor.

In addition, we applied DFT to describe the phases contributing to the local electronic conductivity of each sample. To calculate the DOS for $Li_4Ti_5O_{12}$ and $Li_7Ti_5O_{12}$, we built the model systems and performed structural optimization calculations. The structures are shown in figure 5.3(a).

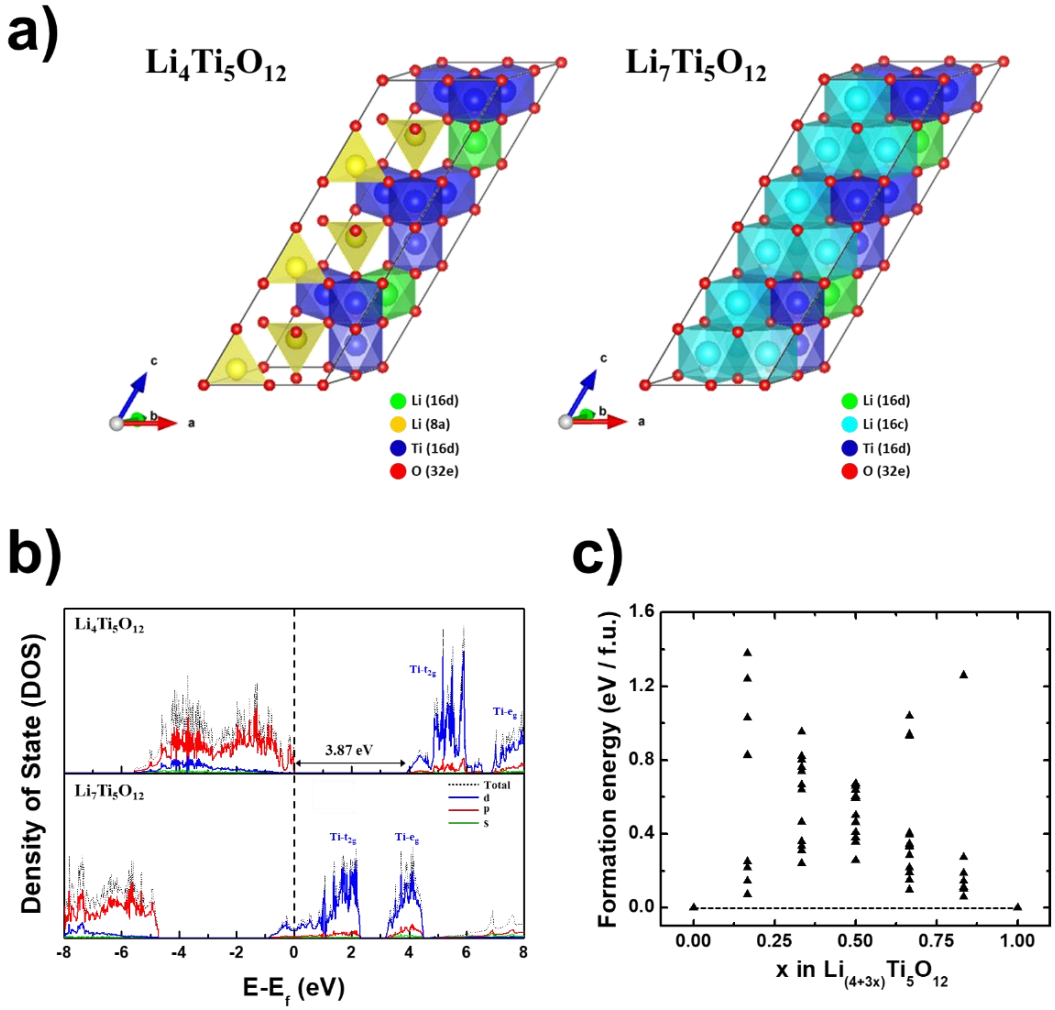

Figure 5.3 (a) Structurally optimized $Li_4Ti_5O_{12}$ and $Li_7Ti_5O_{12}$ lattices. (b) DOS calculations for $Li_4Ti_5O_{12}$ and $Li_7Ti_5O_{12}$ where the Fermi energy is normalized to 0 eV. (c) Formation energy of possible intermediate phases of various Li concentrations with respect to $Li_4Ti_5O_{12}$ and $Li_7Ti_5O_{12}$ end members

We adopted $2Li_4Ti_5O_{12}$ since it has the smallest number of atoms representing $Li_4Ti_5O_{12}$. The structure belongs to the Fd-3m space group and consists of both Li in 8a sites and Li or Ti in 16d sites. Oxygen in 32e sites are tetrahedrally coordinated to 8a sites and octahedrally coordinated to 16d sites. Furthermore, one Li for every five Ti ions are occupied in 16d sites. It was determined that the lowest energy $Li_4Ti_5O_{12}$ structure occurred when octahedrally coordinated Li ions were located farthest away from one another, which is shown as the green Li in figure 5.3(a). Upon lithiation, the original Li ions in 8a sites (yellow) together with intercalated Li ions migrate to 16c sites (cyan) to form $Li_7Ti_5O_{12}$. We confirmed the lattice parameter of fully relaxed $Li_4Ti_5O_{12}$ and its lithiated form, which were calculated using the PBE functional. The values were 8.44 and 8.38 Å, respectively, which corresponds well to experimentally reported values with an error of less than 0.95%. 36 A range of experimentally determined band gaps has been reported for $Li_4Ti_5O_{12}$. Those values are commonly determined to be between 3.0 and 4.0 eV with the most reported value at ca. 3.8 eV.[117, 151-152] Standard DFT calculations, however, underestimate the band gap between 1.7 and 2.3 eV because the GGA functional is not able to properly describe the electron−electron correlation−exchange interaction.[154, 156-157] To measure the band gap more accurately, we adopted the HSE06 hybrid functional to our $Li_4Ti_5O_{12}$ calculations. This functional is capable of improving the band gap calculation by subtly tuning the weight of the Hartree−Fock exchange toward the GGA exchange and correlation. We also confirmed the dependence of $Li_4Ti_5O_{12}$'s band gap on the Hartree−Fock mixing contribution, shown in figure 5.4.

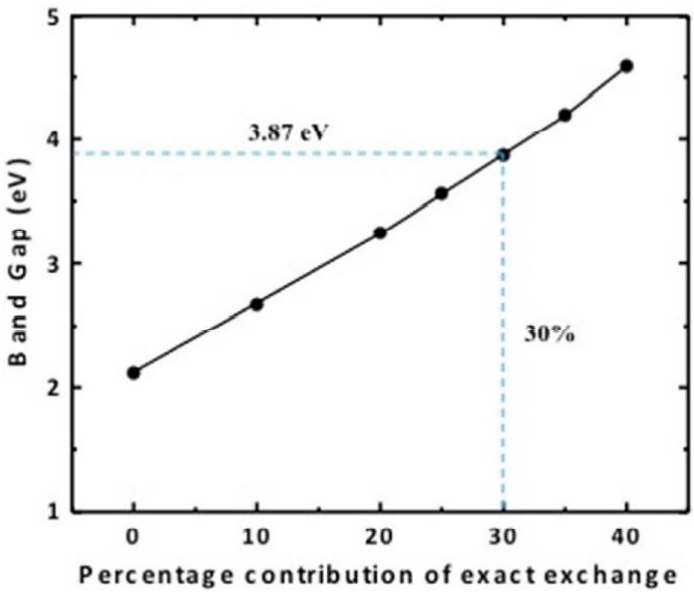

Figure 5.4 Dependence of the calculated $Li_4Ti_5O_{12}$ band gap on the percent contribution of the exact Hartree-Fock (HF) exchange. The dashed blue line indicates the HF percentage used to determine the $Li_4Ti_5O_{12}$ properties we report

The results indicate that the band gap is linearly dependent on the percent contribution of the exact Hartree−Fock exchange. We found that a hybrid functional contribution of 30% exhibits a band gap of 3.87 eV, which is most compatible with experimentally determined band gaps. Figure 5.3(b) shows the electronic structure of $Li_4Ti_5O_{12}$ within the hybrid functional framework described above. The DOS demonstrates the band gap of 3.87 eV, which is primarily defined by the O 2p and Ti 3d bands. We confirmed the breaking of degeneracies of Ti 3d orbitals into t_{2g} and e_g energy levels. This is a common phenomenon originates from the octahedral crystal field. Electrons in pristine $Li_4Ti_5O_{12}$ do not occupy t_{2g} and e_g levels because the oxidation state of all Ti ions is 4+ where Ti 3d electrons do not exist. We applied the 30% Hartree−Fock mixing parameter on lithiated $Li_4Ti_5O_{12}$, which is shown in figure 5.3(b). Upon lithiation, Li ions as well as electrons are incorporated into $Li_4Ti_5O_{12}$, resulting in $Li_7Ti_5O_{12}$. This phase has three Ti^{3+} and two Ti^{4+} so that the lower energy t_{2g} level is partially filled. The DOS of $Li_7Ti_5O_{12}$ is continued across the

Fermi level, which demonstrates the lithiated phase is an electronic conductor. To further determine how $Li_4Ti_5O_{12}$ lithiation/delithiation proceeds, we set up 68 possible intermediate phases and performed DFT calculations using the PBE functional (figure 5.3(c)). We modeled intermediate phases by allocating or removing Li ions into 16c sites of the $Li_4Ti_5O_{12}$ or lithiated $Li_4Ti_5O_{12}$ phases shown in figure 5.3(a). The results indicate that the formation of intermediate phases is unfavorable. The formation energy of the possible $Li_{4+3x}Ti_5O_{12}$ ($0 < x < 1$) intermediate phases are all positive (the system favors a composite mixture of $Li_4Ti_5O_{12}$ and $Li_7Ti_5O_{12}$) in figure 5.3(c), which shows there is no intermediate phase more energetically stable than a mixture of the end phases. The formation of thermodynamically stable end members supports the hypothesis that lithiation/delithiation occurs by means of a two-phase reaction and not by a solid solution mechanism.

5.3.2 $LiNi_{0.5}Mn_{1.5}O_4$ spinel as cathode material in Li-ion batteries

It is reported that the low-index surface planes of $LiMn_2O_4$ spinel (LMO) are thermodynamically unstable and undergo surface reconstruction.[158-159] During the reconstruction, Mn and Li cations migrate and generate Mn_3O_4-like structure on LMO surface, which includes dissoluble Mn^{2+}.[160-162] In order to find surface reconstruction in LNMO case, we set up the pristine LNMO (111) (Fig. 5.5) and possible LNMO (111) reconstruction models (Fig. 5.6).

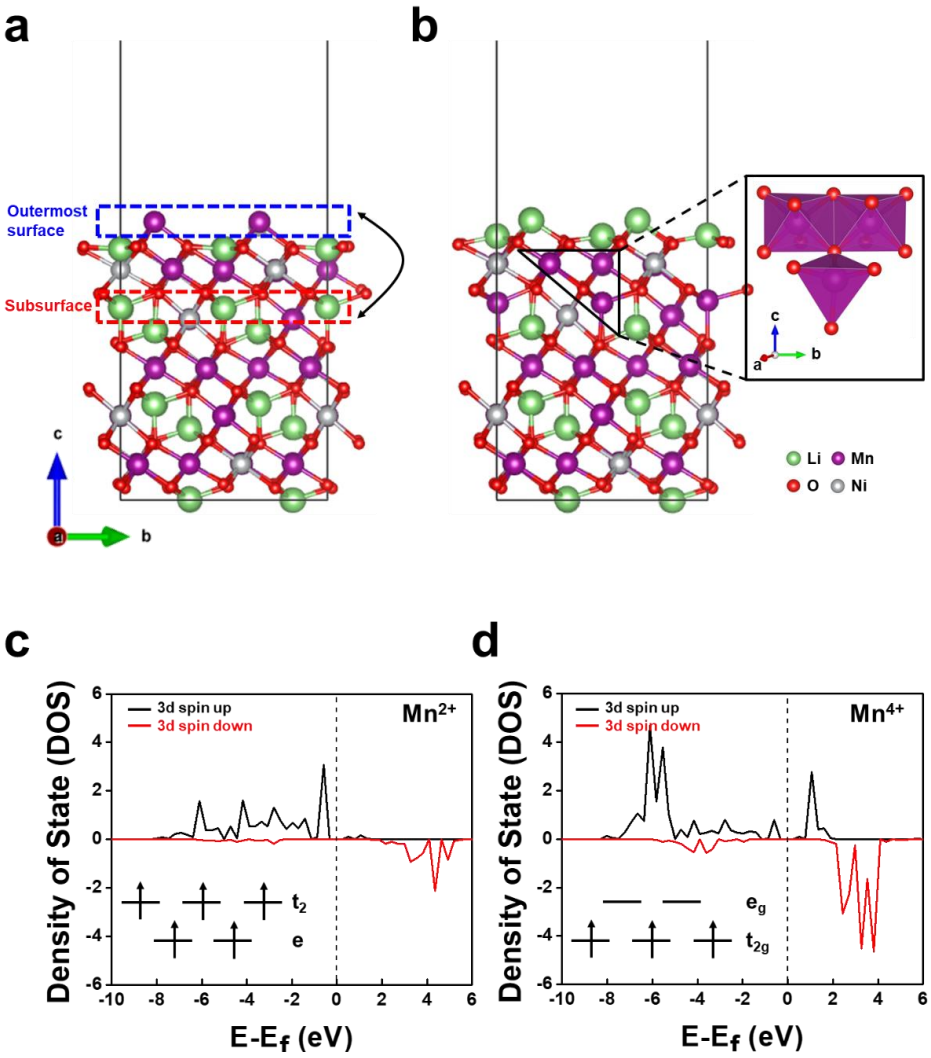

Figure 5.5 (a) The pristine LNMO (111) model where the surface Mn (or Ni) atoms (blue dots) and the subsurface Li atoms (red dots) are swapped to build the surface-reconstructed LNMO (111) models. (b) The surface-reconstructed LNMO (111) model with the lowest surface energy among possible models. The inset to the right shows the Mn_3O_4-like structure. (c) DOS of Mn tetrahedral site in the Mn_3O_4-like structure. (d) DOS of Mn octahedral site in the Mn_3O_4-like structure

The reconstruction models are developed by swapping the outermost surface Mn (or Ni) ions with the subsurface tetrahedral Li ions in the pristine LNMO (111) model (Fig. 5.5(a)). The swapping method was used previously by Kim et al. to study the surface reconstruction of LMO (111).

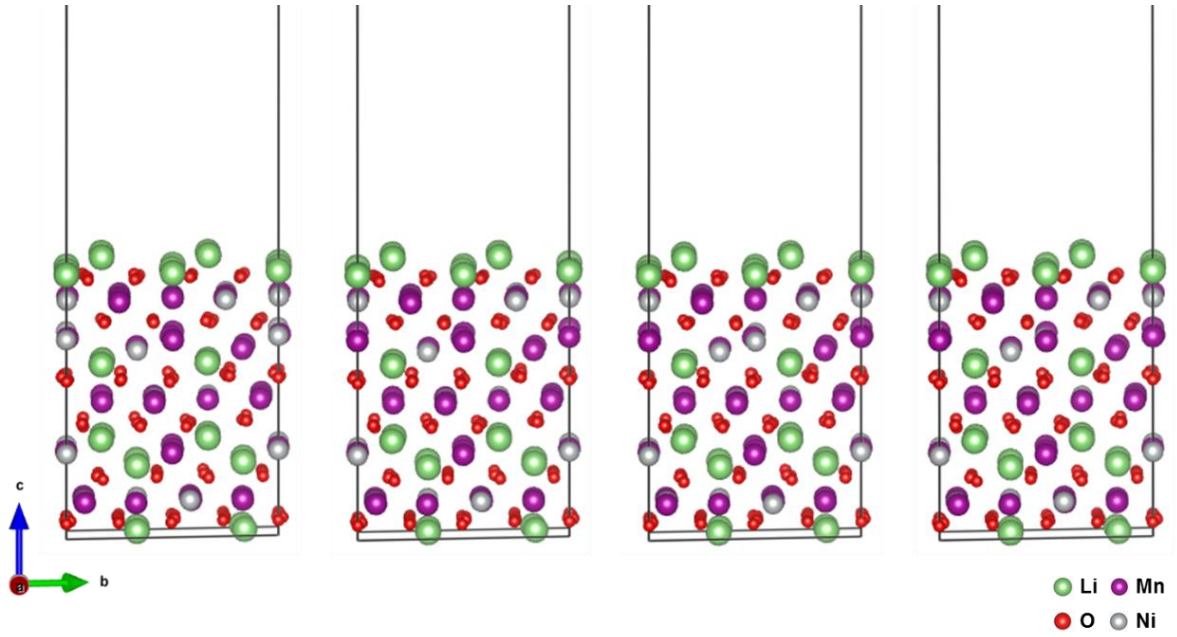

Figure 5.6 Possible LNMO (111) migration models

Among possible reconstruction models in Fig. 5.6, the model shown in Fig. 5.5(b) has the lowest total energy, which indicates the reconstruction model (Fig. 5.5(b)) has lower surface energy than the pristine LNMO (111) by 12 meV/Å^2. This represents the reconstruction stabilizes LNMO surface. It is reported that a lower charged cation, Li^+ on LMO surface leads to a lower surface energy.[159, 163-164] We believe that the surface reconstruction in the pristine LNMO is inevitable because migrated Li^+ on the outermost surface reduces the surface energy.

In addition, the reconstruction model has Mn_3O_4-like structure on the subsurface where the corner-sharing Mn tetrahedron is connected to the edge-sharing Mn octahedron (Fig. 5.5(b)). The density of state (DOS) calculation confirms the oxidation state for those sites: (1) Mn^{2+} in the tetrahedral site, and (2) Mn^{4+} in the octahedral site (Fig. 5.5(c-d)). The spin-up states of 3d orbitals in the tetrahedral Mn are fully occupied (Mn^{2+}); however, the octahedral Mn shows that the lower energy level in spin-up states is solely filled (Mn^{4+}). Thus, we believe Mn^{2+} in Mn_3O_4-like structure dissolves to an electrolyte and leads to capacity fading as LMO degradation does.[160-161] It is

expected that the surface reconstruction is mitigated in *P*-LNMO compared to *SG*-LNMO during cycles due to its extraordinary structure stability observed in synchrotron XAS and HAADF images results.

5.3.3 Oxygen evolution reaction mechanism in $YaBaCo_4O_7$

In alkaline condition, the overall OER reaction is expressed in terms of OH^-. The detailed OER steps are shown in the following equations:

$$4OH^-(aq) \leftrightarrow OH^* + 3OH^- + e^- \quad (1)$$

$$OH^* + 3OH^- + e^- \leftrightarrow O^* + 2OH^- + H_2O(l) + 2e^- \quad (2)$$

$$O^* + 2OH^- + H_2O(l) + 2e^- \leftrightarrow OOH^* + OH^- + H_2O(l) + 3e^- \quad (3)$$

$$OOH^* + OH^- + H_2O(l) + 3e^- \leftrightarrow O_2(g) + 2H_2O(l) + 4e^- \quad (4)$$

where * indicates the adsorption of OER intermediate on a support material. In order to understand the OER mechanism on $YBaCo_4O_7$ (110) by DFT calculations, stoichiometric slab models along [110] direction are built as shown in Figure 5.7. The surface energy (σ) is calculated based on the equation:

$$\sigma = \frac{1}{A}[E_{slab} - nE_{bulk}] \quad (5)$$

where A is the total area of surface in surface model; E_{slab} is the Gibbs energy for surface model; E_{bulk} is the Gibbs energy for bulk model per formula unit (f.u.); and n is the number of f.u. in a surface model.

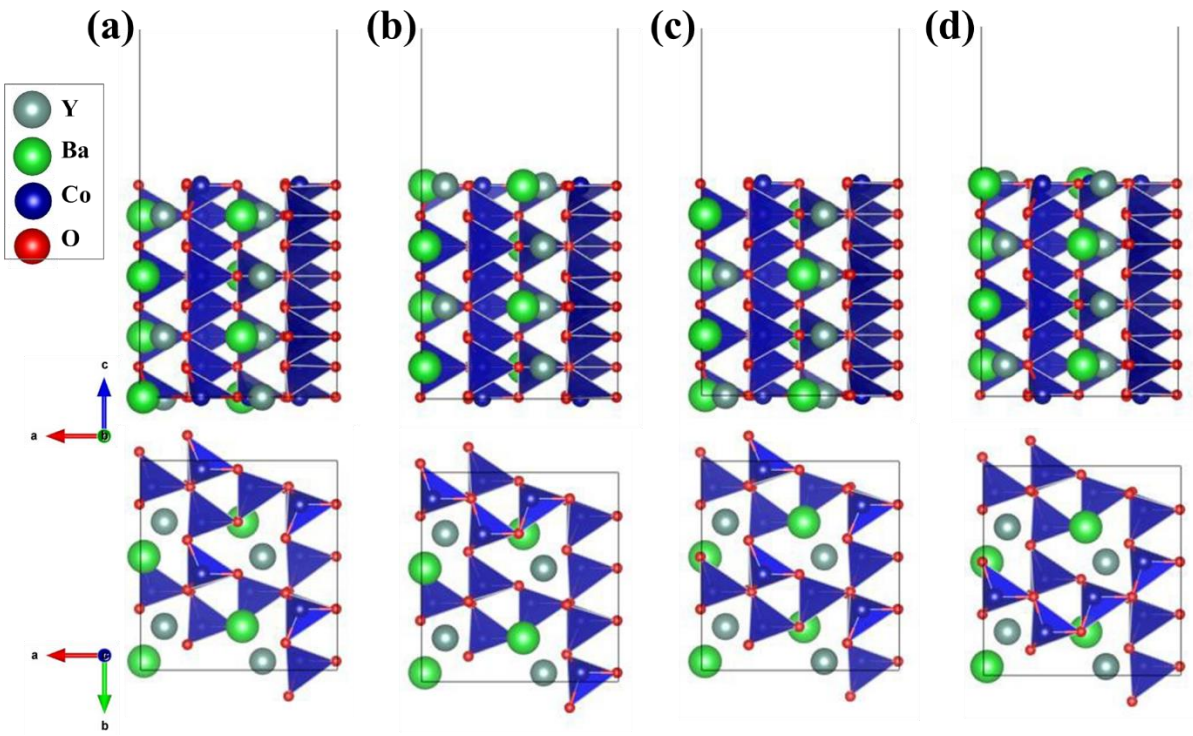

Figure 5.7 Possible terminations of $YBaCo_4O_7$ (110)

The most stable model has the surface energy of 67 meV $Å^{-2}$ (Figure 5.7 (d)), which is chosen to investigate OER mechanism. Since OER starts with a hydroxide adsorption as presented in equation (1), we establish possible OH adsorption sites for Co atom on the surface of YBC4 (110) as shown in Figure 5.8.

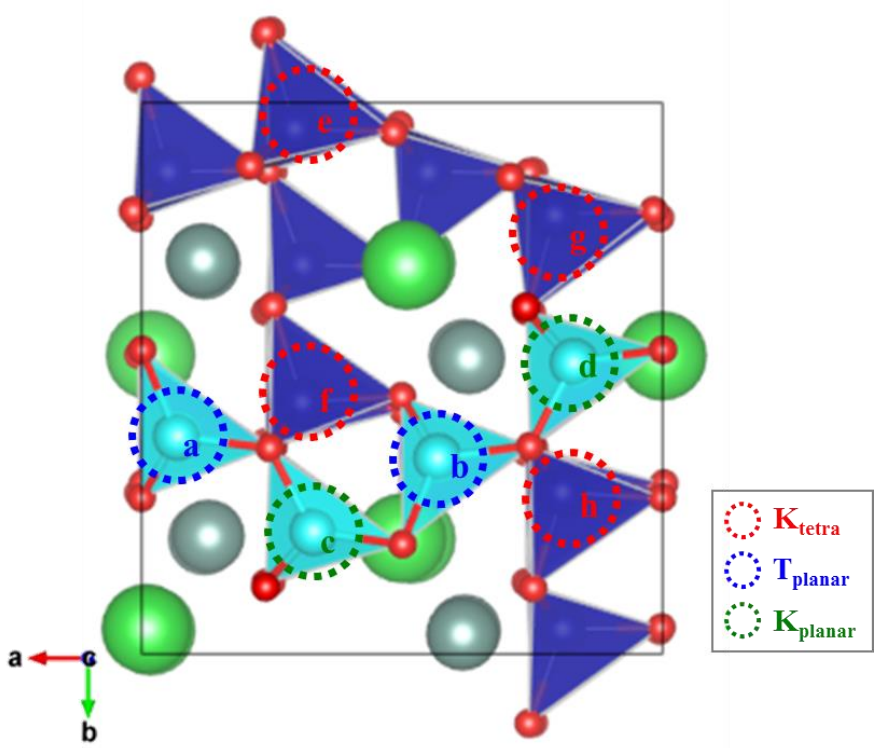

Figure 5.8 Possible OH adsorption sites on the surface of $YBaCo_4O_7$ (110)

There are three types of Co surface sites: (1) planar Co in Kagome layer, (2) planar Co in Triangular layer, and (3) tetrahedral Co in Kagome layer. We assess the most plausible OER active site with the lowest OH adsorption energy. The adsorption energy measured in this study is demonstrated as follows:

$$E_{ads} = E_{adsorbate-\mathrm{YBaCo4O7\,(110)}} - E_{\mathrm{YBaCo4O7\,(110)}} - E_{adsorbate} \quad (6)$$

where $E_{adsorbate-\mathrm{YBaCo4O7\,(110)}}$ is the Gibbs energy for an adsorbate adsorbed on $YBaCo_4O_7$ (110); $E_{\mathrm{YBaCo4O7\,(110)}}$ is the Gibbs energy for $YBaCo_4O_7$ (110); and $E_{adsorbate}$ is the Gibbs energy for OH. The site d shows the lowest adsorption energy among possible OH adsorptions as shown in Table 5.2.

Table 5.2 Calculated adsorption energy of OH on the $YBaCo_4O_7$ (110)

Site	Adsorption type	Absorption Energy (eV / f.u.)
a	T_{planar}	-0.499
b	T_{planar}	-0.511
c	K_{planar}	-0.523
d	K_{planar}	-0.537
e	K_{tetra}	-0.456
f	K_{tetra}	-0.505
g	K_{tetra}	-0.441
h	K_{tetra}	-0.509

It is noted that the structural model of site d shows that OH is located between a planar Co of Kagome layer and a planar Co of triangular layer as shown in Figure 5.9. The site d is 3-oxygen coordinated Co. At the initial stage of OER, OH adsorbed on this 3-oxygen coordinated Co, generating 4-oxygen coordinated Co.

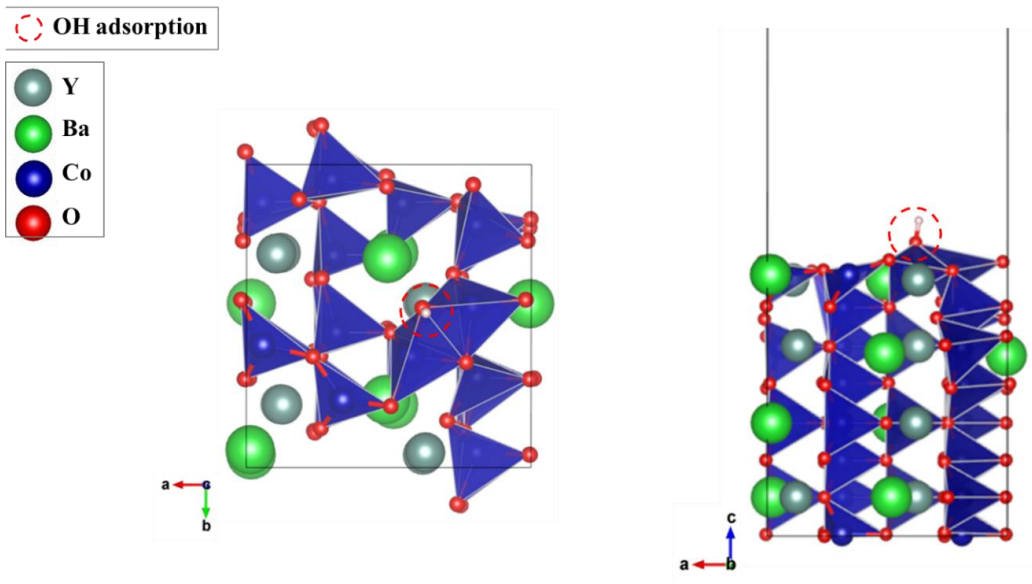

Figure 5.9 The structural model of OH adsorption on site d

The adsorbed hydroxide model (OH^*) undergoes one electron reaction and transforms to single O on the surface (O*). The following reaction is OOH intermediate adsorbed on the surface as demonstrated in equation. 3. The calculation models of OOH adsorbed support materials are developed as shown in Figure 5.10 and their adsorption energy is demonstrated in Table. 5.3.

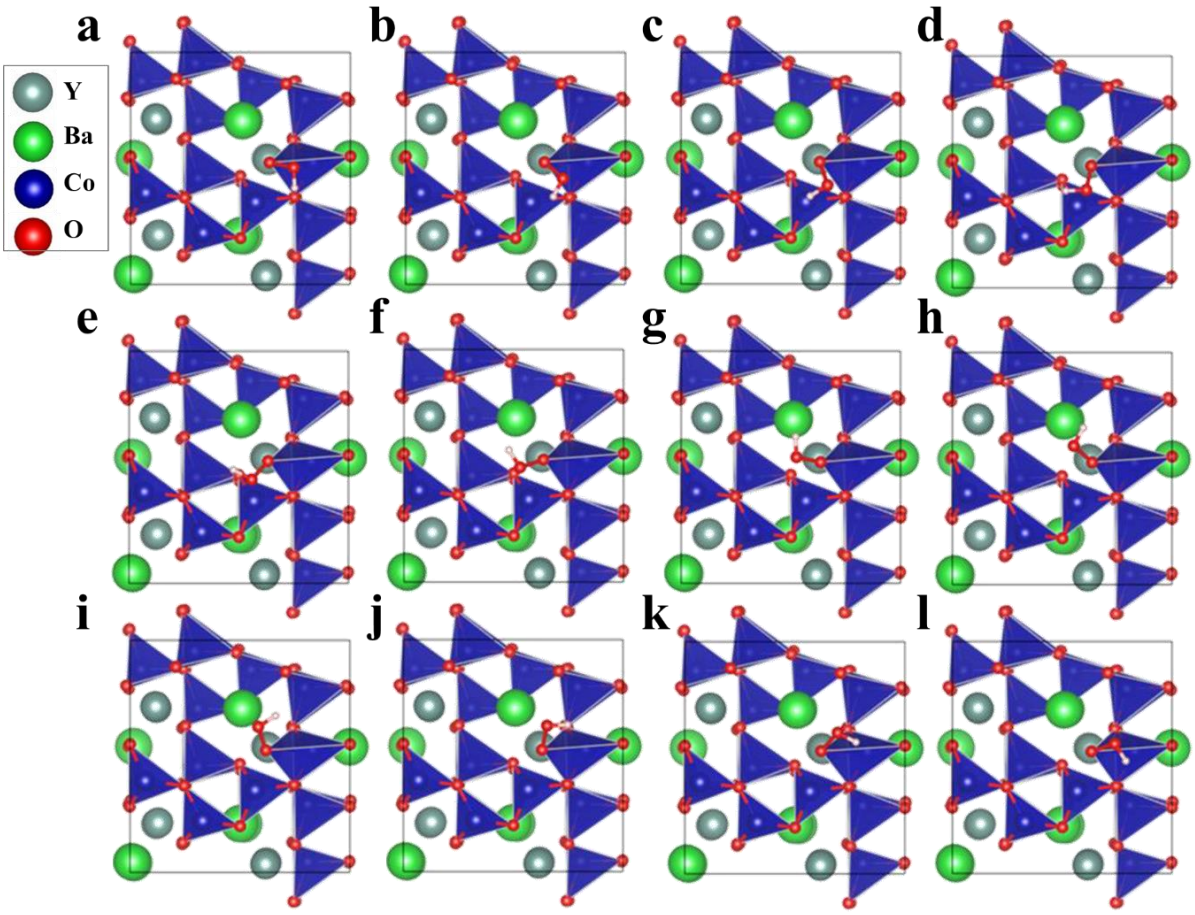

Figure 5.10 Possible OOH adsorption on $YBaCo_4O_7$ (110)

The structure with the lowest OOH adsorption energy is the model for site g where O-H bond heads opposite from the surface with the H-O-O angle of 100.02 deg.

Table 5.3 Calculated energy of OOH adsorbed $YBaCo_4O_7$ (110)

Site	Energy (eV / f.u.)	Site	Energy (eV / f.u.)
a	-86.327	g	-86.413
b	-86.372	h	-86.390
c	-86.364	i	-86.395
d	-86.370	j	-86.358
e	-86.369	k	-86.351
f	-86.378	l	-86.402

The free energy for each reaction (ΔG) demonstrated in equations 1-4 has been calculated using the following equation:

$$\Delta G = \Delta E + \Delta ZPE - T\Delta S \qquad (7)$$

where ΔE is the difference in the DFT calculated ground state energy; ΔZPE is a zero point energy; and TΔS is an entropy correction. We take ΔZPE of intermediates from the thermodynamic table presented by Norskov et al [142] as shown in Table 5.4. The value of ΔS corresponds to T = 298 K (refs.).

Table 5.4 Zero point energy corrections and entropic contributions

	TS	TΔS	ZPE	ΔZPE	ΔZPE-TΔS
H_2O	0.67	0	0.56	0	0
$OH^*+1/2H_2$	0.20	-0.47	0.44	-0.12	0.35
O^*+H_2	0.41	-0.27	0.34	-0.22	0.05
$1/2O_2+H_2$	0.73	0.05	0.32	-0.24	-0.29
H_2	0.41		0.27		
$1/2O_2$	0.32		0.05		
O^*	0		0.07		
OH^*	0		0.30		
H^*	0		0.17		

The free energy of reaction for each OER step (equation 1-4) can be written as a function of applied potential:

$$\Delta G_{eq.1} = \Delta G_{OH^*} - \Delta G_{H2O,l} + 1/2\ \Delta G_{H2} + kT\ln a_{H^+} - eU_1 \quad (8)$$

$$\Delta G_{eq.2} = \Delta G_{O^*} - \Delta G_{OH^*} + 1/2\ \Delta G_{H2} + kT\ln a_{H^+} - eU_2 \quad (9)$$

$$\Delta G_{eq.3} = \Delta G_{OOH^*} - \Delta G_{O^*} - \Delta G_{H2O,l} + 1/2\ \Delta G_{H2} + kT\ln a_{H^+} - eU_3 \quad (10)$$

$$\Delta G_{eq.4} = \Delta G_{O2,g} - \Delta G_{OOH^*} + 1/2\ \Delta G_{H2} + kT\ln a_{H^+} - eU_4 \quad (11)$$

where ΔG is DFT calculated free energy for equation 1-4. Applied potential is shown with respect to the reversible hydrogen electrode (RHE).

The calculated free energy change in each OER step on YBC4(110) surface is shown in Figure 5.11(a) as a function of applied potential. The Figure 5.11(b) shows the optimized structures.

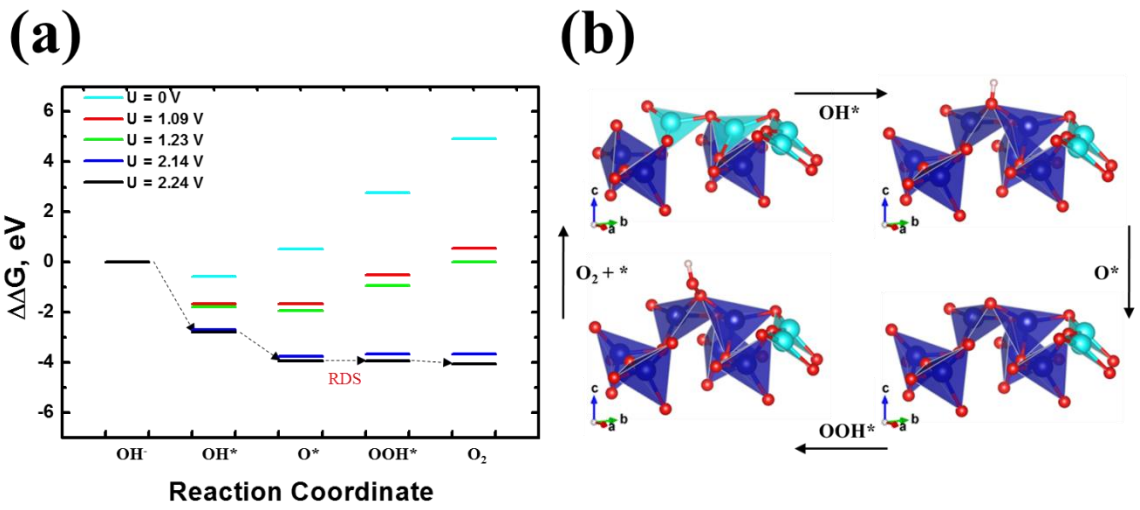

Figure 5.11 (a) Free energy diagram of $YBaCo_4O_7$ (110) depending on potential and (b) Proposed OER steps

At the equilibrium potential (U = 1.23 V), OH* and O* formations are energetically favorable (exothermic) whereas OOH* and O_2 formation steps are not (endothermic). When the applied potential (U) is 2.24 V, all free energy steps become exothermic completing all OER procedure. The oxidation step from O* to OOH* is the rate determining step.

5.4 Conclusions

In this chapter, the effect of Gd doping into the crystal lattice of $Li_4Ti_5O_{12}$ is investigated. Li sites and Ti sites in $Li_4Ti_5O_{12}$ are considered as Gd doping sites. The most stable Gd doped $Li_4Ti_5O_{12}$ structures, $Li_4Ti_{4.5}Gd_{0.5}O_{12}$ and $Li_{3.5}Ti_5Gd_{0.5}O_{12}$ demonstrate the electrical conducting property, which is opposed to the poor conductivity of $Li_4Ti_5O_{12}$.

We also perform DFT calculations to fully describe the reaction mechanism of $Li_4Ti_5O_{12}$ upon lithiation. The results show that intermediate phases of $Li_{4+3x}Ti_5O_{12}$ ($0 < x < 1$) is unfavorable. There is no intermediate phase more energetically stable than the mixture of $Li_4Ti_5O_{12}$ and $Li_7Ti_5O_{12}$. The electronic structure of $Li_4Ti_5O_{12}$ within the hybrid functional framework exhibits

the band gap of 3.87 eV. Upon lithiation, Li ions as well as electrons are incorporated into $Li_4Ti_5O_{12}$, which leads to the electronically conductive property of $Li_7Ti_5O_{12}$ with no band gap.

In addition, the Mn dissolution in LNMO was studied by reconstructing the surface area of LNMO (111). The DFT calculations show LNMO undergoes the surface reconstruction and produces a Mn_3O_4-like structure. DOS of the Mn_3O_4-like structure displays Mn^{2+} in a tetrahedral site, which is dissoluble specie into an electrolyte. As the cycle of LNMO battery goes, Mn^{2+} dissolution is accelerated and the capacity degrades.

Lastly, OER mechanism of YBC4 is investigated on the (110) surface. It is found that the 3-oxygen coordinated (planar) Co is OER active site. During the OER, OH is adsorbs on the planar Co, forming 4-oxygen coordinated (tetrahedral) Co. In addition, the free energy change in OER steps on YBC4 (110) surface is demonstrated by DFT calculations. OH* and O* formations are energetically favorable (exothermic) whereas OOH* and O_2 formation steps are not (endothermic) at the equilibrium potential (U = 1.23 V). Once the applied potential (U) increases to 2.24 V, all free energy steps become exothermic, completing all OER procedures. The rate determining step is the oxidation step from O* to OOH*.

Chapter 5, in part, is a reprint of the material “Elucidating the Phase Transformation of $Li_4Ti_5O_{12}$ Lithiation at the Nanoscale” as it appears in the ACS Nano, Michael G. Verde, Loïc Baggetto, Nina Balke, Gabriel M. Veith, Joon Kyo Seo, Ziying Wang, Ying Shirley Meng, 2016, 10, 4312. The dissertation author was the co-author of this paper. Secondly, chapter 5, in part, is a reprint of the material “Structural and electrochemical properties of Gd-doped $Li_4Ti_5O_{12}$ as anode material with improved rate capability for lithium-ion batteries” as it appears in the Journal of Power Sources, Qianyu Zhang, Michael G. Verde, Joon Kyo Seo, Xi Li, Y. Shirley Meng, 2015, 280, 355. The dissertation author was the co-author of this paper. Thirdly, chapter 5, in part, is

currently being prepared for submission for publication of the material. Hyojung Yoon, Hyeseung Chung, Joon Kyo Seo, Hyung-Man Cho, Danna Qian, Mahsa Sina, Chengyu Song, Jim Ciston, Y. Shirley Meng. The dissertation author was the co-author of this material. Lastly, chapter 5, in part, is currently being prepared for submission for publication of the material. Yubo Chen, Joon Kyo Seo, Jingxian Wang, Shibo Xi, Yonghua Du, Kaidi Yuan, Wei Chen, Adrian C. Fisher, Zhenxing Feng, Y. Shirley Meng, Zhichuan J. Xu. The dissertation author was the co-author of this material.

Chapter 6: Summary

6.1 Transition-metal-fluoride cathode materials for Li-ion conversion reaction

It is commonly found that an experimental conversion voltage is lower than theoretical thermodynamic voltage of a bulk-phase reaction. In this thesis, the factor that affects this phenomenon is demonstrated by combining first principles calculations, electrochemical experiments, and characterization techniques. We confirm that the voltage of conversion reaction heavily relies on the size of the metal nanoparticles generated. ADF-STEM images for the lithiated CuF_2 and NiF_2 cathodes and corresponding electron diffraction patterns show the formation of Cu and Ni nanoparticles at the end of the first discharge. The average particle sizes are ~2.5 and ~1.5 nm, respectively. In addition, PITT is conducted for CuF_2 and NiF_2 batteries to evaluate the near-equilibrium voltage for conversion reactions. The long voltage plateaus are found at ~3.02 V and ~1.77 V during the first discharge, which are lower than the theoretical thermodynamic voltage of CuF_2 (3.55 V) and NiF_2 (2.96 V) for the bulk-phase conversion reaction. We ascribe this voltage deviation to the surface energy of metal nanoparticles. DFT calculations indicate that the surface energy increases as the particle size decreases. The surface energy of metal nanoparticles plays a role as an energy penalty to the reaction energy, which leads to lower voltage compared to the thermodynamic voltage of the bulk-phase reaction. Furthermore, we enable CuF_2 battery to be rechargeable by NiO coating. NiO coated CuF_2 electrode exhibits a reversible specific capacity of 152 mAh g^{-1} at the end of first charge, however, CuF_2 electrode displays a charge failure. During the first charge, the voltage drops at around the redox potential of Cu^{2+}/Cu. EELS elemental maps indicate that the lithiation process mostly proceeds in the region of high NiO concentration. We propose that NiO is a suitable artificial solid electrolyte interphase that hampers Cu nanoparticles to be exposed to the electrolyte. Therefore Cu dissolution into the electrolyte is alleviated,

enhancing the rechargeability of CuF_2.

6.2 Rechargeable Zn/MnO_2 alkaline battery

In this thesis, rechargeable Zn/β-MnO_2 alkaline batteries are studied as a promising stationary energy storage. Unlike commercial Zn/MnO_2 alkaline batteries with poor cyclic performance, synthesized β-MnO_2 nanomaterials in the 3M LiOH and 1M KOH electrolyte promote rechargeable reactions with high capacity. The electrochemical test shows that the average discharge capacity is 280 mAh g^{-1} throughout 100 cycles, which is higher than the average capacity of commercial β-MnO_2 at 116 mAh g^{-1} during 100 cycles. The *ex situ* X-ray diffraction patterns and theoretical thermodynamic voltage show that the proton intercalation reaction is followed by two-phase conversion reactions. Upon the initiation of the first discharge, protons from H_2O molecules intercalate 1 x 1 tunnels in nanosized β-MnO_2 and form γ-MnOOH at the end of the first-electron reaction. γ-MnOOH undergoes a conversion reaction and produces $Mn(OH)_2$ during the second-electron reaction. Mn_3O_4 is formed by a sluggish chemical reaction between γ-MnOOH and $Mn(OH)_2$ in parallel. During the first charge, λ-MnO_2 is generated by conversion reactions. *Ex situ* synchrotron X-ray diffractions are conducted to verify the reaction mechanism during the hundredth cycle. The results demonstate Li and H co-intercalation in the host structure of λ-MnO_2 spinel. The presence of Li is measured by Li 1s region of XPS, which supports the formation and deformation of Li contained phases. We also find electrochemically irreversible phase of $ZnMn_2O_4$ from both the hundredth discharge/charge states, which is formed by chemical reaction between $Zn(OH)_4^{2-}$ and MnOOH. Adding Bi_2O_3 in the nanosized β-MnO_2 cathode exhibits an outstanding discharge capacity. It shows ~316 mAh g^{-1}, which is higher than the commercial β-MnO_2 (112 mAh g^{-1}) and synthesized β-MnO_2 nanomaterial (225 mAh g^{-1}) at the hundredth cycle.

6.3 First principles computational studies on electrode materials

First principles calculations are used in this thesis to understand the thermodynamic properties of $Li_4Ti_5O_{12}$ spinel as an anode material, $LiNi_{0.5}Mn_{1.5}O_4$ spinel as a cathode material in Li-ion batteries, and oxygen evolution reaction mechanism in $YaBaCo_4O_7$.

First of all, we study the influence of Gd doping if it enhances the electronic property of $Li_4Ti_5O_{12}$. Our DOS calculation shows that the band gap of $Li_4Ti_5O_{12}$ is about 2 eV, which is mainly determined by the O 2p and Ti 3d bands and demonstrates that $Li_4Ti_5O_{12}$ is an insulator. Upon substituting Gd with Li site ($Li_{3.5}Ti_5Gd_{0.5}O_{12}$) or Ti site ($Li_4Ti_{4.5}Gd_{0.5}O_{12}$) in $Li_4Ti_5O_{12}$,the electronic property changes to an electrical conductor. The total DOS of $Li_{3.5}Ti_5Gd_{0.5}O_{12}$ moves downwards with respect to the normalized energy ($E-E_f$) and the tail of conduction bands becomes partly filled. On the other hand, the total DOS of $Li_4Ti_{4.5}Gd_{0.5}O_{12}$ shifts upwards with respect to $E-E_f$ and the Fermi level resides in the middle of valence bands, which demonstrates the conducting property.

Secondly, we investigate the formation energy of possible intermediate phases upon Li intercalation, $Li_{4+3x}Ti_5O_{12}$ ($0 < x < 1$). The formation energy of the possible intermediate phases shows higher value than the common tangent line between $Li_4Ti_5O_{12}$ and $Li_7Ti_5O_{12}$. This means there is no intermediate phase more energetically stable than the mixture of end phases of $Li_4Ti_5O_{12}$ and $Li_7Ti_5O_{12}$. The lithiation/delithiation of $Li_{4+3x}Ti_5O_{12}$ ($0 < x < 1$) proceeds through a two-phase reaction.

Thirdly, the surface reconstruction of LNMO and its effect on Mn dissolution are investigated by calculating surface energy of reconstructed LNMO and conducting DOS calculations. The calculated results indicate that LNMO proceeds the surface reconstruction by

swapping the outermost Li and the subsurface Mn, which forms a Mn_3O_4-like structure. DOS of Mn in a tetrahedral site of the Mn_3O_4-like structure exhibits the oxidation state is 2+, which is dissoluble species into an electrolyte. It is expected that Mn^{2+} dissolution is accelerated as the cycle of LNMO battery goes, which degrades the battery's capacity.

Lastly, the study of OER mechanism on YBC4 (110) is conducted by DFT calculations. The 3-oxygen coordinated Co on the YBC4 (110) is an OER active site. Once OER begins, OH is adsorbed into the 3-oxygen coordinated Co and generates 4-oxygen coordinated Co. In addition, the free energy change in OER steps on YBC4 (110) surface is investigated. OH* and O* formations are exothermic processes, which are energetically favorable, however OOH* and O_2 formation steps are endothermic processes at the equilibrium potential (U = 1.23 V). When the applied potential is 2.24 V, all free energy steps become energetically favorable, completing all OER procedure. The rate determining step is the oxidation step from O* to OOH*.

Chapter 7: Conclusions and future directions

Massive research has been conducted to enhance the performance of Li-ion battery since it was commercialized in early 1990s. Li-ion batteries have become a major energy storage in mobile electronics market, yet it is not popular in the vehicle market since the technology is still behind the widespread commercialization for electric vehicles. In order to make Li-ion batteries competitive as an energy source in the vehicle market, their energy and power density needs to match the internal combustion engine.

Considering the energy density, intercalation materials have limits because of intrinsically low concentration of Li-ion. It is important to develop alternative materials that undergo non-intercalation reactions with better energy density. In this regard, conversion-reaction materials have drawn great attention as a promising solution for current Li-ion battery technologies. Conversion materials exhibit at least twofold specific capacity than that of intercalation materials. Multiple oxidation states in a transition metal can be utilized, allowing multiple Li-ion per transition metal to participate in conversion reactions, which results in high specific capacity. The intrinsic property such as large voltage hysteresis during the cycle leads to poor rechargeability, which needs extensive work for commercialization.

In addition, the power density is another issue in developing Li-ion batteries for electric vehicles. Among intercalation materials, Li spinel structures display fast Li-ion diffusion and high power because of their 3D channels. $LiNi_{0.5}Mn_{1.5}O_4$ and $Li_4Ti_5O_{12}$ are representative materials for cathode and anode, respectively. The $LiNi_{0.5}Mn_{1.5}O_4$ cathode has higher operating voltage (~4.7 V vs. Li) and improves structural stability compared to the parent material, $LiMn_2O_4$. In addition, the $Li_4Ti_5O_{12}$ anode is intrinsically safe and stable because of relatively higher operating voltage

compared to graphite and silicon anode, which alleviates the degradation of an electrolyte. Several intrinsic properties of $LiNi_{0.5}Mn_{1.5}O_4$ and $Li_4Ti_5O_{12}$, however, still remain to be solved for their widespread commercialization. The $LiNi_{0.5}Mn_{1.5}O_4$ cathode goes through capacity fade because of the structural degradation on the surface during cycles. It is reported that cation migration proceeds to minimize the surface energy during cycles, which leads to surface degradation at the end. To prevent this, a proper material modification needs to be applied on the surface to minimize the surface energy such as metal-oxide coatings. Considering the $Li_4Ti_5O_{12}$ anode, it has limited electronic conductivity with the band gap of 2 - 4 eV. This property is significantly improved by doping with transition metal in Li and Ti sites. Dopants provide sufficient electrons to enable $Li_4Ti_5O_{12}$ conductive, which enhances electrochemical performance eventually.

Rechargeable Zn/MnO_2 aqueous batteries have been recently developed significantly for stationary energy storage since they are safe, non-flammable, and inexpensive. The pH of aqueous solution is the key to the cyclability of Zn/MnO_2 aqueous batteries. In acidic solutions, Zn anode undergoes Zn^{2+}/Zn redox. Zn^{2+} in aqueous solutions promotes the reversibility by participating in the reversible precipitation of Zn hydroxide sulfate while MnO_2 proceeds proton intercalations. In addition, salt in the electrolyte alleviates the capacity degradation during cycles. For example, $MnSO_4$ salt suppresses electrochemical dissolution of Mn^{2+} upon MnO_2/MnOOH redox in acidic solutions. On the other hand, Zn anode proceeds $Zn(OH)_4^{2-}/Zn$ redox in base solutions. Once $Zn(OH)_4^{2-}$ is generated from Zn anode, it migrates to the cathode and produces $ZnMn_2O_4$ as a result of the chemical reaction between MnOOH and $Zn(OH)_4^{2-}$. $ZnMn_2O_4$ is an electrochemically inactive phase in base solution, which needs to be prevented from forming for rechargeable Zn/MnO_2 in base solution. Bi_2O_3 is one of the effective additives, which alleviates the $ZnMn_2O_4$ formation.

Oxygen evolution reaction (OER) is an important step exists in various electrochemical cells, such as water electrolyzer, metal-air batteries, and fuel cells. In general, OER has a certain level of overpotential as it involves multi electron steps. If one of the steps is sluggish, it increases the overall required energy consumption of OER. Tremendous effort has been applied in the past several decades to find catalysts to promote the rate of OER. As one of effective tools, DFT calculations demonstrate underlying OER mechanisms and propose ideal catalysts that reduce the overpotential. For developing decent OER catalysts, this technique should be adopted for peroxide-type, perovskite-type, and spinel-type oxides, which have captured significant interests recently. For example, the earth-abundant first-row transition metals such as Fe, Co, and Ni in perovskite-type or spinel-type oxide show predominant catalytic performance and promising stability. DFT calculation can provide further development by designing and analyzing materials on an atomic scale.

References

1. Singh, N.; Galande, C.; Miranda, A.; Mathkar, A.; Gao, W.; Reddy, A. L. M.; Vlad, A.; Ajayan, P. M. Paintable Battery **2012,** *2*, 481.

2. Cabana, J.; Monconduit, L.; Larcher, D.; Palacín, M. R. Beyond Intercalation-Based Li-Ion Batteries: The State of the Art and Challenges of Electrode Materials Reacting Through Conversion Reactions. *Adv. Mater.* **2010,** *22* (35), E170-E192.

3. Li, H.; Balaya, P.; Maier, J. Li-storage via Heterogeneous Reaction in Selected Binary Metal Fluorides and Oxides. *J. Electrochem. Soc.* **2004,** *151* (11), A1878-A1885.

4. Lee, D. H.; Carroll, K. J.; Calvin, S.; Jin, S.; Meng, Y. S. Conversion Mechanism of Nickel Fluoride and NiO-doped Nickel Fluoride in Li Ion Batteries. *Electrochim. Acta* **2012,** *59*, 213-221.

5. Lee, D. H.; Carroll, K. J.; Chapman, K. W.; Borkiewicz, O. J.; Calvin, S.; Fullerton, E. E.; Meng, Y. S. Understanding Improved Electrochemical Properties of NiO-doped NiF_2-C Composite Conversion Materials by X-ray Absorption Spectroscopy and Pair Distribution Function Analysis. *Phys. Chem. Chem. Phys.* **2014,** *16* (7), 3095-3102.

6. Armand, M.; Tarascon, J.-M. Building better batteries. *Nature* **2008,** *451* (7179), 652-657.

7. Kim, J. H.; Myung, S. T.; Yoon, C. S.; Kang, S. G.; Sun, Y. K. Comparative Study of LiNi0.5Mn1.5O4-δ and LiNi0.5Mn1.5O4 Cathodes Having Two Crystallographic Structures: Fd3̄m and P4332. *Chemistry of Materials* **2004,** *16* (5), 906-914.

8. Amatucci, G. G.; Pereira, N. Fluoride based electrode materials for advanced energy storage devices. *Journal of Fluorine Chemistry* **2007,** *128* (4), 243-262.

9. Badway, F.; Cosandey, F.; Pereira, N.; Amatucci, G. G. Carbon Metal Fluoride Nanocomposites High-Capacity Reversible Metal Fluoride Conversion Materials as Rechargeable Positive Electrodes for Li Batteries. *J. Electrochem. Soc.* **2003,** *150* (10), A1318-A1327.

10. Badway, F.; Pereira, N.; Cosandey, F.; Amatucci, G. G. Carbon-Metal Fluoride Nanocomposites Structure and Electrochemistry of FeF_3: C. *J. Electrochem. Soc.* **2003,** *150* (9), A1209-A1218.

11. Nitta, N.; Wu, F.; Lee, J. T.; Yushin, G. Li-ion battery materials: present and future.

Materials Today **2015,** *18* (5), 252-264.

12. Yadav, G. G.; Gallaway, J. W.; Turney, D. E.; Nyce, M.; Huang, J.; Wei, X.; Banerjee, S. Regenerable Cu-intercalated MnO2 layered cathode for highly cyclable energy dense batteries. *Nature Communications* **2017,** *8*, 14424.

13. Ingale, N. D.; Gallaway, J. W.; Nyce, M.; Couzis, A.; Banerjee, S. Rechargeability and economic aspects of alkaline zinc–manganese dioxide cells for electrical storage and load leveling. *J. Power Sources* **2015,** *276* (0), 7-18.

14. Gallaway, J. W.; Menard, M.; Hertzberg, B.; Zhong, Z.; Croft, M.; Sviridov, L. A.; Turney, D. E.; Banerjee, S.; Steingart, D. A.; Erdonmez, C. K. Hetaerolite Profiles in Alkaline Batteries Measured by High Energy EDXRD. *J. Electrochem. Soc.* **2015,** *162* (1), A162-A168.

15. Ohzuku, T.; Ueda, A.; Yamamoto, N. Zero-Strain Insertion Material of Li [Li1 / 3Ti5 / 3] O 4 for Rechargeable Lithium Cells. *Journal of The Electrochemical Society* **1995,** *142* (5), 1431-1435.

16. Ferg, E.; Gummow, R. J.; de Kock, A.; Thackeray, M. M. Spinel Anodes for Lithium-Ion Batteries. *Journal of The Electrochemical Society* **1994,** *141* (11), L147-L150.

17. Colbow, K. M.; Dahn, J. R.; Haering, R. R. Structure and electrochemistry of the spinel oxides LiTi2O4 and Li43Ti53O4. *Journal of Power Sources* **1989,** *26* (3), 397-402.

18. Deschanvres, A.; Raveau, B.; Sekkal, Z. Mise en evidence et etude cristallographique d'une nouvelle solution solide de type spinelle Li1+xTi2−xO4 $0 \leqslant x \leqslant 0$, 333. *Materials Research Bulletin* **1971,** *6* (8), 699-704.

19. Yang, Z.; Choi, D.; Kerisit, S.; Rosso, K. M.; Wang, D.; Zhang, J.; Graff, G.; Liu, J. Nanostructures and lithium electrochemical reactivity of lithium titanites and titanium oxides: A review. *Journal of Power Sources* **2009,** *192* (2), 588-598.

20. Xiao, J.; Chen, X.; Sushko, P. V.; Sushko, M. L.; Kovarik, L.; Feng, J.; Deng, Z.; Zheng, J.; Graff, G. L.; Nie, Z.; Choi, D.; Liu, J.; Zhang, J.-G.; Whittingham, M. S. High-Performance LiNi0.5Mn1.5O4 Spinel Controlled by Mn3+ Concentration and Site Disorder. *Advanced Materials* **2012,** *24* (16), 2109-2116.

21. Ma, L.-W.; Chen, B.-Z.; Shi, X.-C.; Zhang, W.; Zhang, K. Stability and Li+ extraction/adsorption properties of LiMxMn2−xO4 (M=Ni, Al, Ti; $0 \leq x \leq 1$) in aqueous solution.

Colloids and Surfaces A: Physicochemical and Engineering Aspects **2010,** *369* (1), 88-94.

22. Arunkumar, T. A.; Manthiram, A. Influence of Lattice Parameter Differences on the Electrochemical Performance of the 5 V Spinel LiMn1.5 − y Ni0.5 − z M y + z O4 (M = Li , Mg, Fe, Co, and Zn). *Electrochemical and Solid-State Letters* **2005,** *8* (8), A403-A405.

23. von Cresce, A.; Xu, K. Electrolyte Additive in Support of 5 V Li Ion Chemistry. *Journal of The Electrochemical Society* **2011,** *158* (3), A337-A342.

24. Burke, M. S.; Enman, L. J.; Batchellor, A. S.; Zou, S.; Boettcher, S. W. Oxygen Evolution Reaction Electrocatalysis on Transition Metal Oxides and (Oxy)hydroxides: Activity Trends and Design Principles. *Chemistry of Materials* **2015,** *27* (22), 7549-7558.

25. Man, I. C.; Su, H.-Y.; Calle-Vallejo, F.; Hansen, H. A.; Martínez, J. I.; Inoglu, N. G.; Kitchin, J.; Jaramillo, T. F.; Nørskov, J. K.; Rossmeisl, J. Universality in Oxygen Evolution Electrocatalysis on Oxide Surfaces. *ChemCatChem* **2011,** *3* (7), 1159-1165.

26. Seo, M. H.; Park, H. W.; Lee, D. U.; Park, M. G.; Chen, Z. Design of Highly Active Perovskite Oxides for Oxygen Evolution Reaction by Combining Experimental and ab Initio Studies. *ACS Catalysis* **2015,** *5* (7), 4337-4344.

27. Serov, A.; Andersen, N. I.; Roy, A. J.; Matanovic, I.; Artyushkova, K.; Atanassov, P. CuCo2O4 ORR/OER Bi-Functional Catalyst: Influence of Synthetic Approach on Performance. *Journal of The Electrochemical Society* **2015,** *162* (4), F449-F454.

28. Armstrong, M. J.; O'Dwyer, C.; Macklin, W. J.; Holmes, J. D. Evaluating the performance of nanostructured materials as lithium-ion battery electrodes. *Nano Res.* **2014,** *7* (1), 1-62.

29. Badway, F.; Mansour, A. N.; Pereira, N.; Al-Sharab, J. F.; Cosandey, F.; Plitz, I.; Amatucci, G. G. Structure and Electrochemistry of Copper Fluoride Nanocomposites Utilizing Mixed Conducting Matrices. *Chem. Mater.* **2007,** *19* (17), 4129-4141.

30. Gocheva, I. D.; Tanaka, I.; Doi, T.; Okada, S.; Yamaki, J.-i. A New Iron Oxyfluoride Cathode Active Material for Li-ion Battery, Fe_2OF_4. *Electrochem. Commun.* **2009,** *11* (8), 1583-1585.

31. Pereira, N.; Badway, F.; Wartelsky, M.; Gunn, S.; Amatucci, G. G. Iron Oxyfluorides as High Capacity Cathode Materials for Lithium Batteries. *J. Electrochem. Soc.* **2009,** *156* (6), A407-A416.

32. Wiaderek, K. M.; Borkiewicz, O. J.; Castillo-Martínez, E.; Robert, R.; Pereira, N.; Amatucci, G. G.; Grey, C. P.; Chupas, P. J.; Chapman, K. W. Comprehensive Insights into the Structural and Chemical Changes in Mixed-Anion FeOF Electrodes by Using Operando PDF and NMR Spectroscopy. *J. Am. Chem. Soc.* **2013,** *135* (10), 4070-4078.

33. Cosandey, F.; Su, D.; Sina, M.; Pereira, N.; Amatucci, G. G. Fe Valence Determination and Li Elemental Distribution in Lithiated $FeO_{0.7}F_{1.3}$/C Nanocomposite Battery Materials by Electron Energy Loss Spectroscopy (EELS). *Micron* **2012,** *43* (1), 22-29.

34. Wang, F.; Kim, S.-W.; Seo, D.-H.; Kang, K.; Wang, L.; Su, D.; Vajo, J. J.; Wang, J.; Graetz, J. Ternary Metal Fluorides as High-energy Cathodes with Low Cycling Hysteresis. *Nat. Commun.* **2015,** *6*, 6668.

35. Ko, J. K.; Wiaderek, K. M.; Pereira, N.; Kinnibrugh, T. L.; Kim, J. R.; Chupas, P. J.; Chapman, K. W.; Amatucci, G. G. Transport, Phase Reactions, and Hysteresis of Iron Fluoride and Oxyfluoride Conversion Electrode Materials for Lithium Batteries. *ACS Appl. Mater. Interfaces* **2014,** *6* (14), 10858–10869.

36. Wang, F.; Robert, R.; Chernova, N. A.; Pereira, N.; Omenya, F.; Badway, F.; Hua, X.; Ruotolo, M.; Zhang, R.; Wu, L. Conversion Reaction Mechanisms in Lithium Ion Batteries: Study of the Binary Metal Fluoride Electrodes. *J. Am. Chem. Soc.* **2011,** *133* (46), 18828-18836.

37. Yamakawa, N.; Jiang, M.; Grey, C. P. Investigation of the Conversion Reaction Mechanisms for Binary Copper (II) Compounds by Solid-State NMR Spectroscopy and X-ray Diffraction. *Chem. Mater.* **2009,** *21* (14), 3162-3176.

38. Hua, X.; Robert, R.; Du, L.-S.; Wiaderek, K. M.; Leskes, M.; Chapman, K. W.; Chupas, P. J.; Grey, C. P. Comprehensive Study of the CuF2 Conversion Reaction Mechanism in a Lithium-ion Battery. *J. Phys. Chem. C* **2014**.

39. Towns, J.; Cockerill, T.; Dahan, M.; Foster, I.; Gaither, K.; Grimshaw, A.; Hazlewood, V.; Lathrop, S.; Lifka, D.; Peterson, G. D.; Roskies, R.; Scott, J. R.; Wilkens-Diehr, N. XSEDE: Accelerating Scientific Discovery. *Comput. Sci. Eng.* **2014,** *16* (5), 62-74.

40. Kresse, G.; Furthmüller, J. Efficient Iterative Schemes for Ab Initio Total-energy Calculations using a Plane-wave Basis Set. *Phys. Rev. B* **1996,** *54* (16), 11169-11186.

41. Dudarev, S. L.; Botton, G. A.; Savrasov, S. Y.; Humphreys, C. J.; Sutton, A. P. Electron-energy-loss Spectra and the Structural Stability of Nickel Oxide:An LSDA+U Study. *Phys. Rev. B* **1998,** *57* (3), 1505-1509.

42. Perdew, J. P.; Burke, K.; Ernzerhof, M. Generalized Gradient Approximation Made Simple. *Phys. Rev. Lett.* **1996,** *77* (18), 3865-3868.

43. Blöchl, P. E. Projector Augmented-wave Method. *Phys. Rev. B* **1994,** *50* (24), 17953-17979.

44. Kresse, G.; Joubert, D. From Ultrasoft Pseudopotentials to the Projector Augmented-wave Method. *Phys. Rev. B* **1999,** *59* (3), 1758-1775.

45. Kresse, G.; Furthmüller, J. Efficiency of Ab-initio Total Energy Calculations for Metals and Semiconductors using a Plane-wave Basis Set. *Comput. Mater. Sci.* **1996,** *6* (1), 15-50.

46. Jain, A.; Hautier, G.; Ong, S. P.; Moore, C. J.; Fischer, C. C.; Persson, K. A.; Ceder, G. Formation Enthalpies by Mixing GGA and GGA + U Calculations. *Phys. Rev. B* **2011,** *84* (4), 045115.

47. Cho, H.-M.; Chen, M. V.; MacRae, A. C.; Meng, Y. S. Effect of Surface Modification on Nano-Structured LiNi0.5Mn1.5O4 Spinel Materials. *ACS Appl. Mater. Interfaces* **2015,** *7* (30), 16231-16239.

48. Seo, J. K.; Khetan, A.; Seo, M. H.; Kim, H.; Han, B. First-principles Thermodynamic Study of the Electrochemical Stability of Pt Nanoparticles in Fuel Cell Applications. *J. Power Sources* **2013,** *238*, 137-143.

49. Noh, S. H.; Han, B.; Ohsaka, T. First-principles computational study of highly stable and active ternary PtCuNi nanocatalyst for oxygen reduction reaction. *Nano Res.* **2015,** *8* (10), 3394-3403.

50. Vitos, L.; Ruban, A. V.; Skriver, H. L.; Kollár, J. The Surface Energy of Metals. *Surf. Sci.* **1998,** *411* (1–2), 186-202.

51. Baletto, F.; Ferrando, R. Structural Properties of Nanoclusters: Energetic, Thermodynamic, and Kinetic Effects. *Rev. Mod. Phys.* **2005,** *77* (1), 371-423.

52. Yacamán, M. J.; Ascencio, J. A.; Liu, H. B.; Gardea-Torresdey, J. Structure Shape and Stability of Nanometric Sized Particles. *J. Vac. Sci. Technol. B* **2001,** *19* (4), 1091-1103.

53. Noh, S. H.; Seo, M. H.; Seo, J. K.; Fischer, P.; Han, B. First Principles Computational Study on the Electrochemical Stability of Pt-Co Nanocatalysts. *Nanoscale* **2013,** *5* (18), 8625-8633.

54. Escaño, M. C. S. First-principles calculations of the dissolution and coalescence properties of Pt nanoparticle ORR catalysts: The effect of nanoparticle shape. *Nano Res.* **2015,** *8* (5), 1689-1697.

55. Klabunde, K. J.; Richards, R. M. *Nanoscale Materials in Chemistry*. John Wiley & Sons, Inc.: Hoboken, 2009.

56. Wang, Z. L. Transmission Electron Microscopy of Shape-Controlled Nanocrystals and Their Assemblies. *J. Phys. Chem. B* **2000,** *104* (6), 1153-1175.

57. Li, Z. Y.; Young, N. P.; Di Vece, M.; Palomba, S.; Palmer, R. E.; Bleloch, A. L.; Curley, B. C.; Johnston, R. L.; Jiang, J.; Yuan, J. Three-Dimensional Atomic-Scale Structure of Size-Selected Gold Nanoclusters. *Nature* **2007,** *451* (7174), 46-48.

58. Yamakawa, N.; Jiang, M.; Key, B.; Grey, C. P. Identifying the Local Structures Formed during Lithiation of the Conversion Material, Iron Fluoride, in a Li Ion Battery: A Solid-State NMR, X-ray Diffraction, and Pair Distribution Function Analysis Study. *J. Am. Chem. Soc.* **2009,** *131* (30), 10525-10536.

59. Mansour, A. N.; Badway, F.; Yoon, W.-S.; Chung, K. Y.; Amatucci, G. G. In Situ X-ray Absorption Spectroscopic Investigation of the Electrochemical Conversion Reactions of CuF_2–MoO_3 nanocomposite. *J. Solid State Chem.* **2010,** *183* (12), 3029-3038.

60. Curtarolo, S.; Morgan, D.; Persson, K.; Rodgers, J.; Ceder, G. Predicting Crystal Structures with Data Mining of Quantum Calculations. *Phys. Rev. Lett.* **2003,** *91* (13), 135503.

61. Barin, I.; Sauert, F.; Schultze-Rhonhof, E.; Sheng, W. S. *Thermochemical Data of Pure Substances*. VCH: Weinheim, 1993.

62. Liu, P.; Vajo, J. J.; Wang, J. S.; Li, W.; Liu, J. Thermodynamics and Kinetics of the Li/FeF_3 Reaction by Electrochemical Analysis. *J. Phys. Chem. C* **2012,** *116* (10), 6467-6473.

63. Poizot, P.; Laruelle, S.; Grugeon, S.; Dupont, L.; Tarascon, J. M. Nano-sized Transition-metal Oxides as Negative-electrode Materials for Lithium-ion Batteries. *Nature* **2000,** *407* (6803), 496-499.

64. Lin, C.-F.; Noked, M.; Kozen, A. C.; Liu, C.; Zhao, O.; Gregorczyk, K.; Hu, L.; Lee, S. B.; Rubloff, G. W. Solid Electrolyte Lithium Phosphous Oxynitride as a Protective Nanocladding Layer for 3D High-Capacity Conversion Electrodes. *ACS Nano* **2016,** *10*, 2693-2701.

65. Medasani, B.; Park, Y. H.; Vasiliev, I. Theoretical Study of the Surface Energy, Stress, and Lattice Contraction of Silver Nanoparticles. *Phys. Rev. B* **2007,** *75* (23), 235436.

66. Delmer, O.; Balaya, P.; Kienle, L.; Maier, J. Enhanced Potential of Amorphous Electrode Materials: Case Study of RuO_2. *Adv. Mater.* **2008,** *20* (3), 501-505.

67. Peng, L.; Dunlap, R. A.; Dahn, J. R. A Mössbauer Effect Study of Combinatorially Prepared Al_2O_3/Fe and LiF/Fe Multilayers. *J. Phys.: Condens. Matter* **2008,** *20* (5), 055203.

68. Dalverny, A. L.; Filhol, J. S.; Doublet, M. L. Interface electrochemistry in conversion materials for Li-ion batteries. *J. Mater. Chem.* **2011,** *21* (27), 10134-10142.

69. Sina, M.; Thorpe, R.; Rangan, S.; Pereira, N.; Bartynski, R. A.; Amatucci, G. G.; Cosandey, F. Investigation of SEI Layer Formation in Conversion Iron Fluoride Cathodes by Combined STEM/EELS and XPS. *J. Phys. Chem. C* **2015,** *119* (18), 9762-9773.

70. Rangan, S.; Thorpe, R.; Bartynski, R. A.; Sina, M.; Cosandey, F.; Celik, O.; Mastrogiovanni, D. D. T. Conversion Reaction of FeF_2 Thin Films upon Exposure to Atomic Lithium. *J. Phys. Chem. C* **2012,** *116* (19), 10498-10503.

71. Cho, J.; Kim, T.-J.; Park, B. The Effect of a Metal-Oxide Coating on the Cycling Behavior at 55°C in Orthorhombic $LiMnO_2$ Cathode Materials. *J. Electrochem. Soc.* **2002,** *149* (3), A288-A292.

72. Kim, B.; Lee, J.-G.; Choi, M.; Cho, J.; Park, B. Correlation between Local Strain and Cycle-life Performance of $AlPO_4$-coated $LiCoO_2$ Cathodes. *J. Power Sources* **2004,** *126* (1–2), 190-192.

73. Shin, J.; You, J.-M.; Lee, J. Z.; Kumar, R.; Yin, L.; Wang, J.; Meng, Y. S. Deposition of ZnO on Bismuth Species Towards Rechargeable Zn-Based Aqueous Battery. *Phys. Chem. Chem. Phys.* **2016,** *18*, 26376.

74. Gallaway, J. W.; Erdonmez, C. K.; Zhong, Z.; Croft, M.; Sviridov, L. A.; Sholklapper, T. Z.; Turney, D. E.; Banerjee, S.; Steingart, D. A. Real-time materials evolution visualized within intact cycling alkaline batteries. *J. Mater. Chem. A* **2014,** *2* (8), 2757-2764.

75. Turney, D. E.; Gallaway, J. W.; Yadav, G. G.; Ramirez, R.; Nyce, M.; Banerjee, S.; Chen-Wiegart, Y.-c. K.; Wang, J.; D'Ambrose, M. J.; Kolhekar, S.; Huang, J.; Wei, X. Rechargeable Zinc Alkaline Anodes for Long-Cycle Energy Storage. *Chem. Mater.* **2017,** *29* (11), 4819-4832.

76. Julien, C. M.; Massot, M.; Poinsignon, C. Lattice vibrations of manganese oxides: Part I. Periodic structures. *Spectrochimica Acta Part A: Molecular and Biomolecular Spectroscopy* **2004,** *60* (3), 689-700.

77. Zhang, K.; Han, X.; Hu, Z.; Zhang, X.; Tao, Z.; Chen, J. Nanostructured Mn-based oxides for electrochemical energy storage and conversion. *Chem. Soc. Rev.* **2015,** *44* (3), 699-728.

78. Patrice, R.; Gérand, B.; Leriche, J. B.; Seguin, L.; Wang, E.; Moses, R.; Brandt, K.; Tarascon, J. M. Understanding the Second Electron Discharge Plateau in MnO2-Based Alkaline Cells. *J. Electrochem. Soc.* **2001,** *148* (5), A448-A455.

79. McBreen, J. The electrochemistry of β-MnO2 and γ-MnO2 in alkaline electrolyte. *Electrochim. Acta* **1975,** *20* (3), 221-225.

80. Boden, D.; Venuto, C. J.; Wisler, D.; Wylie, R. B. The Alkaline Manganese Dioxide Electrode: I . The Discharge Process. *J. Electrochem. Soc.* **1967,** *114* (5), 415-417.

81. Holton, D. M.; Maskell, W. C.; Tye, F. L. The Behaviour of γ-MnO2 and Reduced Forms in Concentrated KOH Solution. *In Proc. 14th International Power Sources*

Symposium **1985,** *10*, p. 247.

82. Lee, B.; Seo, H. R.; Lee, H. R.; Yoon, C. S.; Kim, J. H.; Chung, K. Y.; Cho, B. W.; Oh, S. H. Critical Role of pH Evolution of Electrolyte in the Reaction Mechanism for Rechargeable Zinc Batteries. *ChemSusChem* **2016,** *9* (20), 2948-2956.

83. Lee, B.; Yoon, C. S.; Lee, H. R.; Chung, K. Y.; Cho, B. W.; Oh, S. H. Electrochemically-induced reversible transition from the tunneled to layered polymorphs of manganese dioxide. *Sci. Rep.* **2014,** *4*, 6066.

84. Pan, H.; Shao, Y.; Yan, P.; Cheng, Y.; Han, K. S.; Nie, Z.; Wang, C.; Yang, J.; Li, X.; Bhattacharya, P.; Mueller, K. T.; Liu, J. Reversible aqueous zinc/manganese oxide energy storage from conversion reactions. *Nat. Energy* **2016,** *1*, 16039.

85. Hertzberg, B. J.; Huang, A.; Hsieh, A.; Chamoun, M.; Davies, G.; Seo, J. K.; Zhong, Z.; Croft, M.; Erdonmez, C.; Meng, Y. S.; Steingart, D. Effect of Multiple Cation Electrolyte Mixtures on Rechargeable Zn–MnO2 Alkaline Battery. *Chem. Mater.* **2016,** *28* (13), 4536-4545.

86. Chamoun, M.; Hertzberg, B. J.; Gupta, T.; Davies, D.; Bhadra, S.; Van Tassell, B.;

Erdonmez, C.; Steingart, D. A. Hyper-dendritic nanoporous zinc foam anodes. *NPG Asia Mater.* **2015,** *7*, e178.

87. Chen, J.; Cheng, F. Combination of Lightweight Elements and Nanostructured Materials for Batteries. *Acc. Chem. Res.* **2009,** *42* (6), 713-723.

88. Cheng, F.; Zhao, J.; Song, W.; Li, C.; Ma, H.; Chen, J.; Shen, P. Facile Controlled Synthesis of MnO2 Nanostructures of Novel Shapes and Their Application in Batteries. *Inorg. Chem.* **2006,** *45* (5), 2038-2044.

89. Persson, K. A.; Waldwick, B.; Lazic, P.; Ceder, G. Prediction of solid-aqueous equilibria: Scheme to combine first-principles calculations of solids with experimental aqueous states. *Phys. Rev. B* **2012,** *85* (23), 235438.

90. Stranick, M. A. MnO2 by XPS. *Surf. Sci. Spectra* **1999,** *6* (1), 31-38.

91. Han, B. C.; Miranda, C. R.; Ceder, G. Effect of particle size and surface structure on adsorption of O and OH on platinum nanoparticles: A first-principles study. *Phys. Rev. B* **2008,** *77* (7), 075410.

92. Jacob, K.; Kumar, A.; Rajitha, G.; Waseda, Y. Thermodynamic Data for Mn3O4, Mn2O3 and MnO2. *High Temperature Materials and Processes* **2011,** *30* (4), 459-472.

93. Hem, J. D.; Lind, C. J. Nonequilibrium models for predicting forms of precipitated manganese oxides. *Geochimica et Cosmochimica Acta* **1983,** *47* (11), 2037-2046.

94. Wagman, D. D.; Evans, W. H.; Parker, V. B.; Schumm, R. H.; Halow, I. *The NBS tables of chemical thermodynamic properties. Selected values for inorganic and C1 and C2 organic substances in SI units*; DTIC Document: 1982.

95. Dirkse, T. P. The Behavior of the Zinc Electrode in Alkaline Solutions: III . The Equilibrium Potential. *J. Electrochem. Soc.* **1979,** *126* (9), 1456-1459.

96. Bratsch, S. G. Standard Electrode Potentials and Temperature Coefficients in Water at 298.15 K. *J. Phys. Chem. Ref. Data* **1989,** *18* (1), 1-21.

97. Kordesch, K.; Gsellmann, J.; Tomantschger, K. The alkaline manganese dioxide-zinc cell. *J. Electroanal. Chem. Interfacial Electrochem.* **1981,** *118* (0), 187-201.

98. Donne, S. W.; Lawrance, G. A.; Swinkels, D. A. J. Redox Processes at the Manganese Dioxide Electrode: II. Slow-Scan Cyclic Voltammetry. *J. Electrochem. Soc.* **1997,** *144* (9), 2954-2961.

99. Binder, L.; Kordesch, K.; Urdl, P. Improvements of the Rechargeable Alkaline MnO2 - Zn Cell. *J. Electrochem. Soc.* **1996,** *143* (1), 13-17.

100. Kozawa, A.; Kalnoki-Kis, T.; Yeager, J. F. Solubilities of Mn(II) and Mn(III) Ions in Concentrated Alkaline Solutions. *J. Electrochem. Soc.* **1966,** *113* (5), 405-409.

101. Wang, J.-G.; Jin, D.; Zhou, R.; Li, X.; Liu, X.-r.; Shen, C.; Xie, K.; Li, B.; Kang, F.; Wei, B. Highly Flexible Graphene/Mn3O4 Nanocomposite Membrane as Advanced Anodes for Li-Ion Batteries. *ACS Nano* **2016,** *10* (6), 6227-6234.

102. Gao, J.; Lowe, M. A.; Abruña, H. D. Spongelike Nanosized Mn3O4 as a High-Capacity Anode Material for Rechargeable Lithium Batteries. *Chem. Mater.* **2011,** *23* (13), 3223-3227.

103. Wang, H.; Cui, L.-F.; Yang, Y.; Sanchez Casalongue, H.; Robinson, J. T.; Liang, Y.; Cui, Y.; Dai, H. Mn3O4−Graphene Hybrid as a High-Capacity Anode Material for Lithium Ion Batteries. *J. Am. Chem. Soc.* **2010,** *132* (40), 13978-13980.

104. Sharma, Y.; Haynes, A.; Binder, L.; Kordesch, K. The effect of the amount of electrolyte in the anode gel on the rechargeability of alkaline manganese dioxide · zinc cells. *J. Power Sources* **1989,** *27* (2), 145-153.

105. Yao, Y. F.; Gupta, N.; Wroblowa, H. S. Rechargeable manganese oxide electrodes. *J. Electroanal. Chem. Interfacial Electrochem.* **1987,** *223* (1), 107-117.

106. Wroblowa, H. S.; Gupta, N. Rechargeable manganese oxide electrodes. *J. Electroanal. Chem. Interfacial Electrochem.* **1987,** *238* (1), 93-102.

107. Dzieciuch, M. A.; Gupta, N.; Wroblowa, H. S. Rechargeable Cells with Modified MnO2 Cathodes. *J. Electrochem. Soc.* **1988,** *135* (10), 2415-2418.

108. Zhu, G.-N.; Wang, Y.-G.; Xia, Y.-Y. Ti-based compounds as anode materials for Li-ion batteries. *Energy & Environmental Science* **2012,** *5* (5), 6652-6667.

109. Goodenough, J. B.; Kim, Y. Challenges for Rechargeable Li Batteries. *Chemistry of*

Materials **2010,** *22* (3), 587-603.

110. Oumellal, Y.; Delpuech, N.; Mazouzi, D.; Dupre, N.; Gaubicher, J.; Moreau, P.; Soudan, P.; Lestriez, B.; Guyomard, D. The failure mechanism of nano-sized Si-based negative electrodes for lithium ion batteries. *Journal of Materials Chemistry* **2011,** *21* (17), 6201-6208.

111. Aravindan, V.; Lee, Y.-S.; Madhavi, S. Research Progress on Negative Electrodes for Practical Li-Ion Batteries: Beyond Carbonaceous Anodes. *Advanced Energy Materials* **2015,** *5* (13), 1402225-n/a.

112. Takami, N.; Hoshina, K.; Inagaki, H. Lithium Diffusion in Li4/3Ti5/3O4 Particles during Insertion and Extraction. *Journal of The Electrochemical Society* **2011,** *158* (6), A725-A730.

113. Chen, C. H.; Vaughey, J. T.; Jansen, A. N.; Dees, D. W.; Kahaian, A. J.; Goacher, T.; Thackeray, M. M. Studies of Mg-Substituted Li4−xMg x Ti5O12 Spinel Electrodes (0≤x≤1) for Lithium Batteries. *Journal of The Electrochemical Society* **2001,** *148* (1), A102-A104.

114. Nitta, N.; Yushin, G. High-Capacity Anode Materials for Lithium-Ion Batteries: Choice of Elements and Structures for Active Particles. *Particle & Particle Systems Characterization* **2014,** *31* (3), 317-336.

115. Rho, Y. H.; Kanamura, K. Li+ ion diffusion in Li4Ti5O12 thin film electrode prepared by PVP sol–gel method. *Journal of Solid State Chemistry* **2004,** *177* (6), 2094-2100.

116. Edwards, P. P.; Egdell, R. G.; Fragala, I.; Goodenough, J. B.; Harrison, M. R.; Orchard, A. F.; Scott, E. G. A study of the spinel materials LiTi2O4 and Li43Ti53O4 by photoelectron spectroscopy. *Journal of Solid State Chemistry* **1984,** *54* (2), 127-135.

117. Kostlánová, T.; Dědeček, J.; Krtil, P. The effect of the inner particle structure on the electronic structure of the nano-crystalline Li–Ti–O spinels. *Electrochimica Acta* **2007,** *52* (5), 1847-1856.

118. Pang, L.; Zhao, M.; Zhao, X.; Chai, Y. Preparation and electrochemical performance of Gd-doped LiFePO4/C composites. *Journal of Power Sources* **2012,** *201*, 253-258.

119. Scharner, S.; Weppner, W.; Schmid-Beurmann, P. Evidence of Two-Phase Formation upon Lithium Insertion into the Li1.33Ti1.67 O 4 Spinel. *Journal of The Electrochemical Society* **1999,** *146* (3), 857-861.

120. Kanamura, K.; Umegaki, T.; Naito, H.; Takehara, Z.; Yao, T. Structural and electrochemical characteristics of Li4/3Ti5/3O4 as an anode material for rechargeable lithium batteries. *J Appl Electrochem* **2001,** *31* (1), 73-78.

121. Sathiya, M.; Abakumov, A. M.; Foix, D.; Rousse, G.; Ramesha, K.; Saubanere, M.; Doublet, M. L.; Vezin, H.; Laisa, C. P.; Prakash, A. S.; Gonbeau, D.; VanTendeloo, G.; Tarascon, J. M. Origin of voltage decay in high-capacity layered oxide electrodes. *Nat Mater* **2015,** *14* (2), 230-238.

122. Kim, M. C.; Nam, K. W.; Hu, E. Y.; Yang, X. Q.; Kim, H.; Kang, K.; Aravindan, V.; Kim, W. S.; Lee, Y. S. Sol- Gel Synthesis of Aliovalent Vanadium- Doped LiNi0.Mn-5(1).O-5(4) Cathodes with Excellent Performance at High Temperatures. *Chemsuschem* **2014,** *7* (3), 829-834.

123. Huang, R.; Ikuhara, Y. H.; Mizoguchi, T.; Findlay, S. D.; Kuwabara, A.; Fisher, C. A. J.; Moriwake, H.; Oki, H.; Hirayama, T.; Ikuhara, Y. Oxygen-Vacancy Ordering at Surfaces of Lithium Manganese(III,IV) Oxide Spinel Nanoparticles. *Angew Chem Int Edit* **2011,** *50* (13), 3053-3057.

124. Kim, J. H.; Yoon, C. S.; Myung, S. T.; Prakash, J.; Sun, Y. K. Phase transitions in Li1-delta Ni0.5Mn1.5O4 during cycling at 5 v. *Electrochem Solid St* **2004,** *7* (7), A216-A220.

125. Manthiram, A.; Chemelewski, K.; Lee, E.-S. A perspective on the high-voltage LiMn1.5Ni0.5O4 spinel cathode for lithium-ion batteries. *Energy & Environmental Science* **2014**.

126. Liu, D.; Zhu, W.; Trottier, J.; Gagnon, C.; Barray, F.; Guerfi, A.; Mauger, A.; Groult, H.; Julien, C. M.; Goodenough, J. B.; Zaghib, K. Spinel materials for high-voltage cathodes in Li-ion batteries. *RSC Advances* **2014,** *4* (1), 154-167.

127. Santhanam, R.; Rambabu, B. Research progress in high voltage spinel LiNi0.5Mn1.5O4 material. *Journal of Power Sources* **2010,** *195* (17), 5442-5451.

128. Cho, H.-M.; Meng, Y. S. Effect of Ni/Mn Ordering on Elementary Polarizations of LiNi0.5Mn1.5O4 Spinel and Its Nanostructured Electrode. *J. Electrochem. Soc.* **2013,** *160* (9), A1482-A1488.

129. Ulvestad, A.; Singer, A.; Cho, H.-M.; Clark, J. N.; Harder, R.; Maser, J.; Meng, Y. S.; Shpyrko, O. G. Single Particle Nanomechanics in Operando Batteries via Lensless Strain Mapping. *Nano Lett.* **2014,** *14* (9), 5123-5127.

130. Singer, A.; Ulvestad, A.; Cho, H.-M.; Kim, J. W.; Maser, J.; Harder, R.; Meng, Y. S.; Shpyrko, O. G. Nonequilibrium Structural Dynamics of Nanoparticles in LiNi1/2Mn3/2O4 Cathode under Operando Conditions. *Nano Lett.* **2014,** *14* (9), 5295-5300.

131. Xia, Y. Y.; Zhou, Y. H.; Yoshio, M. Capacity fading on cycling of 4 V Li/LiMn2O4 cells. *J Electrochem Soc* **1997,** *144* (8), 2593-2600.

132. Zhan, C.; Lu, J.; Jeremy Kropf, A.; Wu, T.; Jansen, A. N.; Sun, Y.-K.; Qiu, X.; Amine, K. Mn(II) deposition on anodes and its effects on capacity fade in spinel lithium manganate–carbon systems. *Nat Commun* **2013,** *4*.

133. Lin, M. X.; Ben, L. B.; Sun, Y.; Wang, H.; Yang, Z. Z.; Gu, L.; Yu, X. Q.; Yang, X. Q.; Zhao, H. F.; Yu, R.; Armand, M.; Huang, X. J. Insight into the Atomic Structure of High-Voltage Spinel LiNiO3Mn1.5O4 Cathode Material in the First Cycle. *Chemistry of Materials* **2015,** *27* (1), 292-303.

134. Pistoia, G.; Antonini, A.; Rosati, R.; Zane, D. Storage characteristics of cathodes for Li-ion batteries. *Electrochim Acta* **1996,** *41* (17), 2683-2689.

135. Pieczonka, N. P. W.; Liu, Z. Y.; Lu, P.; Olson, K. L.; Moote, J.; Powell, B. R.; Kim, J. H. Understanding Transition-Metal Dissolution Behavior in LiNi0.5Mn1.5O4 High-Voltage Spinel for Lithium Ion Batteries. *J Phys Chem C* **2013,** *117* (31), 15947-15957.

136. Aurbach, D.; Levi, M. D.; Gamulski, K.; Markovsky, B.; Salitra, G.; Levi, E.; Heider, U.; Heider, L.; Oesten, R. Capacity fading of LixMn2O4 spinel electrodes studied by XRD and electroanalytical techniques. *Journal of Power Sources* **1999,** *81–82*, 472-479.

137. Huang, H. T.; Vincent, C. A.; Bruce, P. G. Capacity loss of lithium manganese oxide spinel in LiPF6/ethylene carbonate-dimethyl carbonate electrolytes. *J Electrochem Soc* **1999,** *146* (2), 481-485.

138. Jang, D. H.; Shin, Y. J.; Oh, S. M. Dissolution of spinel oxides and capacity losses in 4V Li/LixMn2O4 coils. *J Electrochem Soc* **1996,** *143* (7), 2204-2211.

139. Kim, M. C.; Kim, S. H.; Aravindan, V.; Kim, W. S.; Lee, S. Y.; Lee, Y. S. Ultrathin Polyimide Coating for a Spinel LiNi0.5Mn1.5O4 Cathode and Its Superior Lithium Storage Properties under Elevated Temperature Conditions. *J Electrochem Soc* **2013,** *160* (8), A1003-A1008.

140. Lee, Y.; Suntivich, J.; May, K. J.; Perry, E. E.; Shao-Horn, Y. Synthesis and Activities of Rutile IrO2 and RuO2 Nanoparticles for Oxygen Evolution in Acid and Alkaline Solutions. *The Journal of Physical Chemistry Letters* **2012,** *3* (3), 399-404.

141. Inoue, M.; Hirasawa, I. The relationship between crystal morphology and XRD peak intensity on CaSO4·2H2O. *Journal of Crystal Growth* **2013,** *380* (Supplement C), 169-175.

142. Fadley, C. S.; Shirley, D. A. Multiplet Splitting of Metal-Atom Electron Binding Energies. *Physical Review A* **1970,** *2* (4), 1109-1120.

143. Nelson, A. J.; Reynolds, J. G.; Christou, G. Spin-state effects on the outer core-level multiplet structures for high-spin Mn molecular clusters. *Journal of Applied Physics* **2003,** *93* (5), 2536-2539.

144. Bagus, P. S.; Freeman, A. J.; Sasaki, F. Prediction of New Multiplet Structure in Photoemission Experiments. *Physical Review Letters* **1973,** *30* (18), 850-853.

145. Laumann, A.; Boysen, H.; Bremholm, M.; Fehr, K. T.; Hoelzel, M.; Holzapfel, M. Lithium Migration at High Temperatures in Li4Ti5O12 Studied by Neutron Diffraction. *Chemistry of Materials* **2011,** *23* (11), 2753-2759.

146. Blöchl, P. E.; Jepsen, O.; Andersen, O. K. Improved tetrahedron method for Brillouin-zone integrations. *Physical Review B* **1994,** *49* (23), 16223-16233.

147. Heyd, J.; Scuseria, G. E.; Ernzerhof, M. Hybrid functionals based on a screened Coulomb potential. *The Journal of Chemical Physics* **2003,** *118* (18), 8207-8215.

148. Wang, L.; Maxisch, T.; Ceder, G. Oxidation energies of transition metal oxides within the GGA + U framework. *Physical Review B* **2006,** *73* (19), 195107.

149. Lu, X.; Zhao, L.; He, X.; Xiao, R.; Gu, L.; Hu, Y. S.; Li, H.; Wang, Z.; Duan, X.; Chen, L. Lithium storage in Li4Ti5O12 spinel: The full static picture from electron microscopy. *Advanced Materials* **2012,** *24* (24), 3233-3238.

150. Sun, Y.; Zhao, L.; Pan, H.; Lu, X.; Gu, L.; Hu, Y.-S.; Li, H.; Armand, M.; Ikuhara, Y.; Chen, L.; Huang, X. Direct atomic-scale confirmation of three-phase storage mechanism in Li4Ti5O12 anodes for room-temperature sodium-ion batteries**2013,** *4*, 1870.

151. Jhan, Y.-R.; Duh, J.-G. Electrochemical performance and low discharge cut-off voltage behavior of ruthenium doped Li4Ti5O12 with improved energy density. *Electrochimica Acta* **2012,** *63* (0), 9-15.

152. Kim, C.; Norberg, N. S.; Alexander, C. T.; Kostecki, R.; Cabana, J. Mechanism of Phase Propagation During Lithiation in Carbon-Free Li4Ti5O12 Battery Electrodes. *Advanced Functional Materials* **2013,** *23* (9), 1214-1222.

153. Raja, M. W.; Mahanty, S.; Kundu, M.; Basu, R. N. Synthesis of nanocrystalline Li4Ti5O12 by a novel aqueous combustion technique. *Journal of Alloys and Compounds* **2009,** *468* (1–2), 258-262.

154. Ouyang, C. Y.; Zhong, Z. Y.; Lei, M. S. Ab initio studies of structural and electronic properties of Li4Ti5O12 spinel. *Electrochemistry Communications* **2007,** *9* (5), 1107-1112.

155. Ding, Z.; Zhao, L.; Suo, L.; Jiao, Y.; Meng, S.; Hu, Y.-S.; Wang, Z.; Chen, L. Towards understanding the effects of carbon and nitrogen-doped carbon coating on the electrochemical performance of Li4Ti5O12 in lithium ion batteries: a combined experimental and theoretical study. *Physical Chemistry Chemical Physics* **2011,** *13* (33), 15127-15133.

156. Tsai, P.-c.; Hsu, W.-D.; Lin, S.-k. Atomistic Structure and Ab Initio Electrochemical Properties of Li4Ti5O12 Defect Spinel for Li Ion Batteries. *Journal of The Electrochemical Society* **2014,** *161* (3), A439-A444.

157. Jones, R. O.; Gunnarsson, O. The density functional formalism, its applications and prospects. *Reviews of Modern Physics* **1989,** *61* (3), 689-746.

158. Benedek, R.; Thackeray, M. M. Simulation of the surface structure of lithium manganese oxide spinel. *Physical Review B* **2011,** *83* (19), 195439.

159. Kim, S.; Aykol, M.; Wolverton, C. Surface phase diagram and stability of (001) and (111) LiMn2O4 spinel oxides. *Physical Review B* **2015,** *92* (11), 115411.

160. Tang, D.; Sun, Y.; Yang, Z.; Ben, L.; Gu, L.; Huang, X. Surface Structure Evolution of LiMn2O4 Cathode Material upon Charge/Discharge. *Chemistry of Materials* **2014,** *26* (11), 3535-3543.

161. Tang, D.; Ben, L.; Sun, Y.; Chen, B.; Yang, Z.; Gu, L.; Huang, X. Electrochemical behavior and surface structural change of LiMn2O4 charged to 5.1 V. *Journal of Materials Chemistry A*

2014, *2* (35), 14519-14527.

162. Amos, C. D.; Roldan, M. A.; Varela, M.; Goodenough, J. B.; Ferreira, P. J. Revealing the Reconstructed Surface of Li[Mn2]O4. *Nano Letters* **2016,** *16* (5), 2899-2906.

163. Parker, S. C.; Oliver, P. M.; De Leeuw, N. H.; Titiloye, J. O.; Watson, G. W. Atomistic simulation of mineral surfaces: Studies of surface stability and growth. *Phase Transitions* **1997,** *61* (1-4), 83-107.

164. Bhattacharya, J.; Wolverton, C. Relative stability of normal vs. inverse spinel for 3d transition metal oxides as lithium intercalation cathodes. *Physical Chemistry Chemical Physics* **2013,** *15* (17), 6486-6498.